Diels-Alder thermoreversible polymer networks and their nanocomposites

Doctoral Dissertation
Doctoral Program in Science and technology of materials (35th Cycle)

# Diels-Alder thermoreversible polymer networks and their nanocomposites


By

**Francesco Cantamessa**

* * * * * *

**Supervisor**
Prof. Alberto Fina


## Doctoral Examination Committee:

Prof. Enrico Dalcanale, Referee, Università di Parma
Prof. Jean-Marie Raquez, Referee, University of Mons
Prof. Giada Lo Re, Chalmers University of Technology
Prof. Maurizio Galimberti, Politecnico di Milano
Prof. Alberto Frache, Politecnico di Torino


Politecnico di Torino
2023

# Declaration

I hereby declare that, the contents and organization of this dissertation constitute my own original work and does not compromise in any way the rights of third parties, including those relating to the security of personal data.

Francesco Cantamessa

2023

* This dissertation is presented in partial fulfillment of the requirements for **Ph.D. degree** in the Graduate School of Politecnico di Torino (ScuDo).

*To the people who stand by me*

# Acknowledgments

I want to thank all the people who shared this journey, starting from the ones who collaborated with me during these years in the experimental work: Rossella Arrigo for the help in rheology data interpretations, Orietta Monticelli and her group for the work done together, Fabio Carniato for his work on silica functionalization, Emiliano Bilotti and Giovanni Santagiuliana for inviting me in Queen Mary University of London and teaching me their Press&Fold method. Then I want to thank all my colleagues in Alessandria and Torino: Chiara, Francesco, Valentina, Lorenza, Tian, Marta, Massimo, Samuele, Rossella, Chiara, Giulia, Fulvia, Federico, Daniele, Diego, Giusi. A special thanks goes to Sergio Salviati and Giuseppe Ferraro, former colleagues who introduced me for the first time in the laboratory. Another special thanks goes to Samuele Matta and Jiang Tianhui, who shared this "interesting" writing period with me. And a last special thanks goes to Carpeneto, town of incredible stories that animated our coffee breaks, home of our wonderful and irreplaceable colleague Chiara Paravidino. Finally, I want to thank my supervisor, Alberto Fina, with whom I really shared this long journey and also some passion for cycling.

I want also to thank all the people who supported me during these years: my close friends, especially Giovanni, Francesca, Davide, Stefano, Massimo, Caterina, Luca, Marta, Francesco and all the others, who are able to be always there when it comes the time despite my inner solitary nature, I'm so grateful for that. Thanks also to my mother, to my father and to Paolo, my brother. Then, I want also to thank my bike, which kept me from going insane during the writing process of this thesis. Finally, a special thanks goes to Silvia, who without doubts is the first person I think about looking at these years.

# Abstract

This doctoral dissertation addresses the industrially viable and environmentally sustainable preparation of thermoreversibly crosslinked polymers and nanocomposites. First, the state of the art on Covalent Adaptable Networks (CANs) and composites is presented, in order to give to the reader a clear background into which this work lies. The two main classes of CANs, associative and dissociative, according to the network rearrangement process, are presented and discussed with a variety of examples, in the case of both polymers and composites. After showing the differences between the two approaches, the choice of a dissociative system is justified and the experimental work is presented. Three different groups of dissociative CANs based on the thermoreversible crosslinking via Diels-Alder (DA) reaction of three different polymers (a Styrene Maleic Anhydride (SMA) copolymer, a Polyethylene grafted with Maleic Anhydride (PEgMA) and an Ethylene-Propylene Rubber grafted with Maleic Anhydride (EPRgMA)) were prepared via melt blending as an environmental-friendly alternative to traditional synthesis in organic solvents. Functionalization of the polymers with furan groups was previously validated in solvent for SMA, then performed in a melt blender for the three polymers. The achievement of the functionalization was assessed by FT-IR spectroscopy. The obtained grafted polymers (SMAgF, PEgF and EPRgF) were subsequently mixed with different amounts of bismaleimide (BM or BM1) in a micro-extruder. Crosslinking was assessed by FT-IR spectroscopy and confirmed for EPRgF-BM CANs, which were further characterized for physical properties. Crosslinking degree was assessed by solubility at room temperature, while the thermoreversible character of the network was confirmed by a solubility test at 110 °C and by re-molding via hot-pressing. Mechanical and thermomechanical properties of the obtained rubbers showed potential to compete with conventionally crosslinked elastomers, with stiffness in the range 1-1.7 MPa and strain at break in the range 200-500%, while allowing recycling via a simple melt processing step.

Reduced Graphene Oxide (rGO) and Silica (Sil) nanoparticles were selected as suitable nanofillers for EPR, due to the central role of carbon and silica fillers in rubber industry and the reinforcement provided by nanoparticles at low loadings. Possible DA reaction on carbon nanoparticles, described in the state of the art, was explored via a model reaction between Graphite NanoPlates (GNP) and MA, both following a solvent method already used in literature (GNP-MA_sol) and using a new developed vapor method which does not involves the use of solvents (GNP-MA_vap). Then the prepared GNP-MA adducts were characterized via TGA, DSC, XPS, FT-IR and Raman spectroscopy, evidencing the presence of interacting MA on GNP in GNP-MA_vap with indications of covalent DA grafting. Nanocomposites based on the thermoreversible rubber were prepared with rGO, showing significantly increasing stiffness up to ca. 8 MPa, ~2-fold increased strength, and thermal conductivity up to ~0.5 W/(m·K). To overcome the problem of high viscosity in the melt during processing, an alternative processing technique called Press&Fold (P&F) method was used with the aim of rising the content of rGO in the nanocomposite, unfortunately with unsatisfying results due to matrix degradation. Regarding Sil nanocomposites, a maleimide-functionalized silica (Sil-M) was prepared and then mixed with EPRgF. Mechanical properties of EPRgF/Sil-M were compared to unfunctionalized EPRgF/Sil to demonstrate the role of DA crosslinking on mechanical properties. Furthermore, the combination between Sil-M and BM as a conventional DA crosslinker was investigated, to optimize crosslinking degree and materials performances.

Overall, results reported in this work demonstrate the possibility to develop a new class of recyclable nanocomposite rubbers for the substitution of conventional rubbers, which are currently causing major problems in the management of rubber products at their end-of life, using an industrially viable e sustainable process.

# Contents

# List of Figures

# List of Tables

# Chapter 1

# State of the art

## 1.1. Covalent adaptable networks

Covalent Adaptable Networks (CANs) are polymeric materials whose aim is to merge the benefits of thermoplastic and thermoset polymers. In general, thermoplastics are easily processable and reprocessable, and so recyclable, but usually they have lower mechanical strength and stiffness due to the weak interactions between chains. Thermoplastic polymers are also more sensible to chemical attacks, since they are soluble in a proper solvent. On the other hand, crosslinked polymers usually present higher stiffness and tensile strength, they are more resistant to high temperatures and they are insoluble, but they are less easily processable than their thermoplastic homologues and they are not reprocessable. Indeed, in a classic thermoset material the network is formed by strong covalent bonds (crosslinks) between the polymer chains, instead of weak interactions and entanglements as in the case of thermoplastic polymers. In a crosslinked network these covalent bonds impede the flow of the chains with the temperature increase and the solubilization of the polymer as well. Moreover, these strong covalent crosslinks, contribute to the higher stiffness and tensile strength of several thermosets, compared to thermoplastics. It is clear how attractive can be the option to reach some of the benefits of both these polymer categories: insolubility and superior mechanical properties, coupled with easier processability and the possibility to recycle. This is the basic idea behind the developing of CANs, developing networks that are not fixed but rearrangeable.

It is convenient to divide CANs in two main categories, based on the type of reaction exploited to achieve the network rearrangement: they can be based on exchange reactions (in this case they are usually called *associative* polymer networks) or they can exploit addition reactions (in this case they are typically called *dissociative* polymer networks) [1, 2]. Representative schemes of both categories are shown in Figure 1.

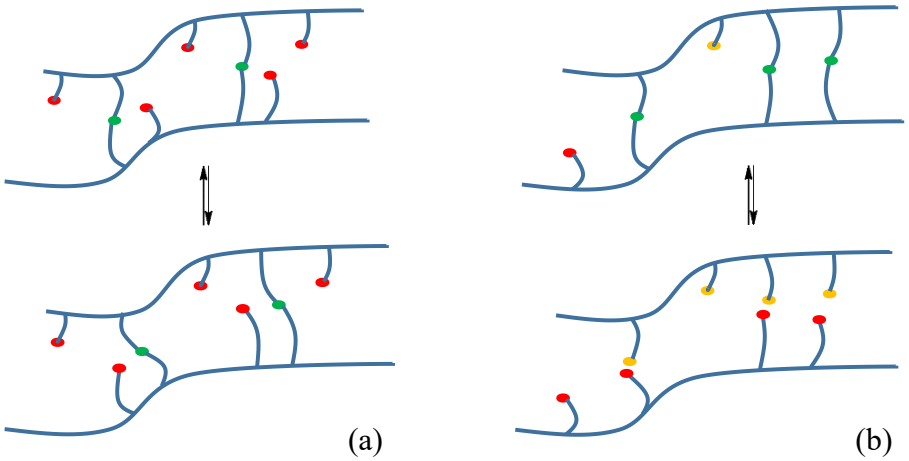


Figure 1. Schemes of CANs based on exchange reactions (a) and addition reactions (b).

In the case of exchange reaction-based CANs (Figure 1 (a)), these associative networks are able to reorganize when the activation conditions for the involved reaction are reached (typically with the rise of temperature), changing their conformation without reducing the total number of crosslinks. Indeed, the crosslink density of these network is constant during their rearrangement. These associative CANs are often referred to as *vitrimers,* after the pioneering work of Leibler's research group [3], with the parallelism of this kind of viscous behaviour with that of vitreous silica. On the other hand, addition reaction-based CANs (Figure 1 (b)) involve the formation of reversible adducts between the chains, generating the crosslinks. These crosslinks break when the condition for the reverse reaction are met, cleaving the network. In this case, the crosslinking density does not remain constant during the rearrangement process, but it drops then rises again when the condition to reform the adducts are met again, regenerating the network.

In the next sections an extensive presentation of several examples of CANs, both exchange and addition reaction-based, is presented, in order to give to the reader an overview of the current state of the art and the frame in which this work lays.

### 1.1.1. Associative Covalent Adaptable Networks

Associative CANs reprocessability is based on the rearrangement of their networks, thanks to exchange reactions between the crosslink sites. Fundamentally, these exchange reactions at room temperature are usually not active, or with a very low reaction rate, so the network results to be fixed. Then, increasing temperature the reaction rate increase allowing the network rearrangement and flow. There are many examples of exchange reactions used to prepare associative CANs, including transesterification [3-8], transamination [9-11], disulfide or dioxaborolane metathesis [12-14] and disulfide-thiol exchange [15] among others [16].

The first pioneering work about associative CANs was carried out in 2011 by Montarnal *et al.* [3], exploiting transesterification as the crosslinking dynamic reaction. Transesterification reaction involves an ester and an alcohol: a new ester is formed with the interchange of the alkoxy moiety [17]. Here the authors generated an associative CAN from an epoxy resin thanks to the presence of hydroxyl groups and ester links and adding a proper catalyst, as outlined in Figure 2.

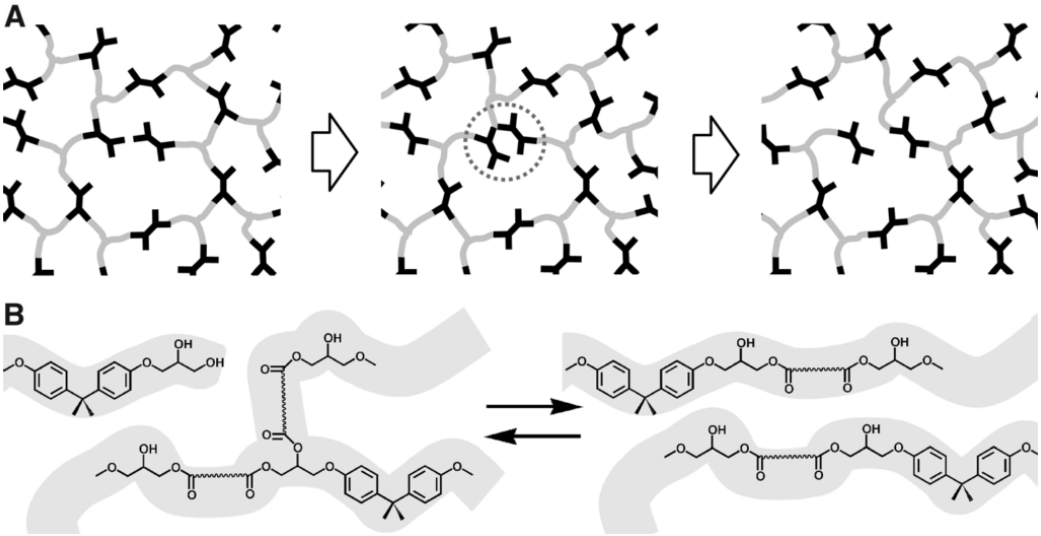


Figure 2. Scheme of the associative CAN rearrangement process with constant crosslinking density (a). Exchange transesterification reaction in the network (b). From *"D. Montarnal, M. Capelot, F. Tournilhac, L. Leibler, Silica-like malleable materials from permanent organic networks, Science 334(6058) (2011) 965-968"*. Reprinted with permission from AAAS.

The authors assessed the polymer crosslinking via FT-IR spectroscopy and solubilization tests, then demonstrated the ability of the network to flow, increasing

temperature, via stress relaxation tests (Figure 3 (a)) and reprocessing (Figure 3 (b)).

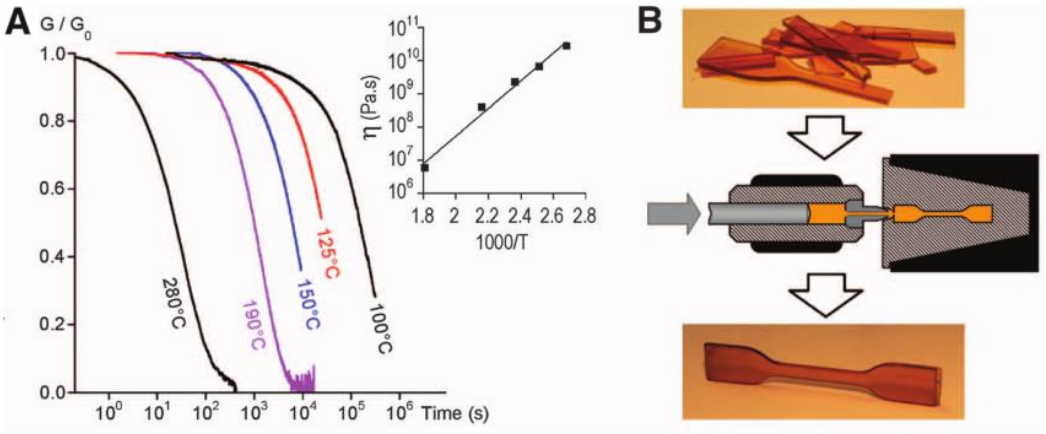


Figure 3. Stress relaxation curves, with normalized complex modulus G trend over time (a), and reprocessing via injection molding (b) of the epoxy vitrimer. From "*D. Montarnal, M. Capelot, F. Tournilhac, L. Leibler, Silica-like malleable materials from permanent organic networks, Science 334(6058) (2011) 965-968*". Reprinted with permission from AAAS.

Stress relaxation tests (Figure 3 (a)) clearly show that these polymer networks, subjected to a constant deformation, relaxes over variable timescales, depending on temperature; this is a sign that increasing temperature the network is able to rearrange and flow faster. Besides, the authors evidenced the trend of viscosity (inset in Figure 3 (a)), following the Arrhenius law, with an activation energy of 80 kJ/mol. The network reprocessability is confirmed by re-molding tests (Figure 3 (b)), where it was evidenced the possibility to process again this crosslinked epoxy resin. Moreover, the authors reported also the polymer insolubility at high temperature.

Among the several works on associative CANs based on transesterification reaction [3-8], Kaiser *et al.* [6] prepared a covalently crosslinked Hydrogenated Carboxylated Nitrile Butadiene Rubber (HXNBR), as outlined in Figure 4.

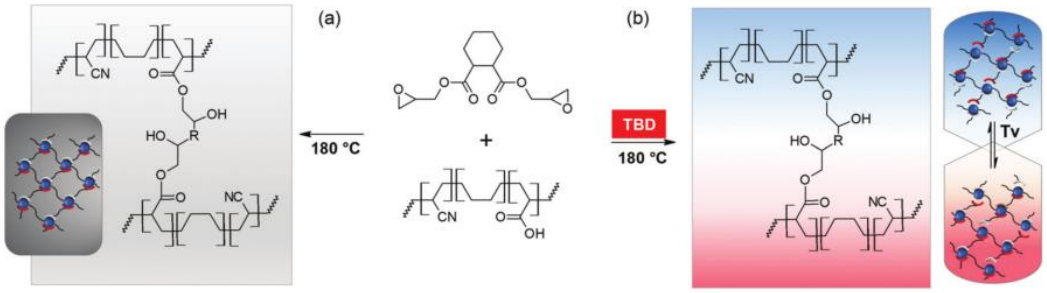


Figure 4. Crosslinking process of HXNBR without (a) and with (b) a transesterification catalyst (triazabicyclodecene, TBD), generating a fixed and a dynamic network, respectively. Used with permission of Royal Society of Chemistry, from "*S. Kaiser, S. Wurzer, G. Pilz, W. Kern, S. Schlögl, Stress relaxation and thermally adaptable properties in vitrimer-like elastomers from HXNBR rubber with covalent bonds, Soft Matter 15(30) (2019) 6062-6072"*; permission conveyed through Copyright Clearance Center, Inc.

The authors performed stress relaxation tests (Figure 5) on the crosslinked HXNBR with and without catalyst (TBD) at different temperatures. In Figure 5 (a) and (b), it can be seen that HXNBR without TBD (green curve), with 10 mol% of TBD (orange curve) and with 20 mol% of TBD (red curve), have different behaviour at different temperatures: at 30°C (Figure 5 (a)), all the rubbers does not present stress relaxation (the curves are constant), while at 180°C (Figure 5 (b)) the presence of the catalyst allows stress relaxation. The authors reported also the trends of stress relaxation for the crosslinked rubber containing 10 mol% of TBD (Figure 5 (c)) and 20 mol% of TBD (Figure 5 (d)) at different temperature steps from 30°C to 180°C, showing that a lower content of catalyst allows the rearrangement of the network only at higher temperatures, while an higher catalyst availability allows stress relaxation and flow starting from lower temperatures. This behaviour highlights how much the exchange reaction kinetic (here controlled by the catalyst) is central in the associative CANs reorganization, in order to obtain a material that is mechanically stable at room temperature, but reworkable at high temperature.

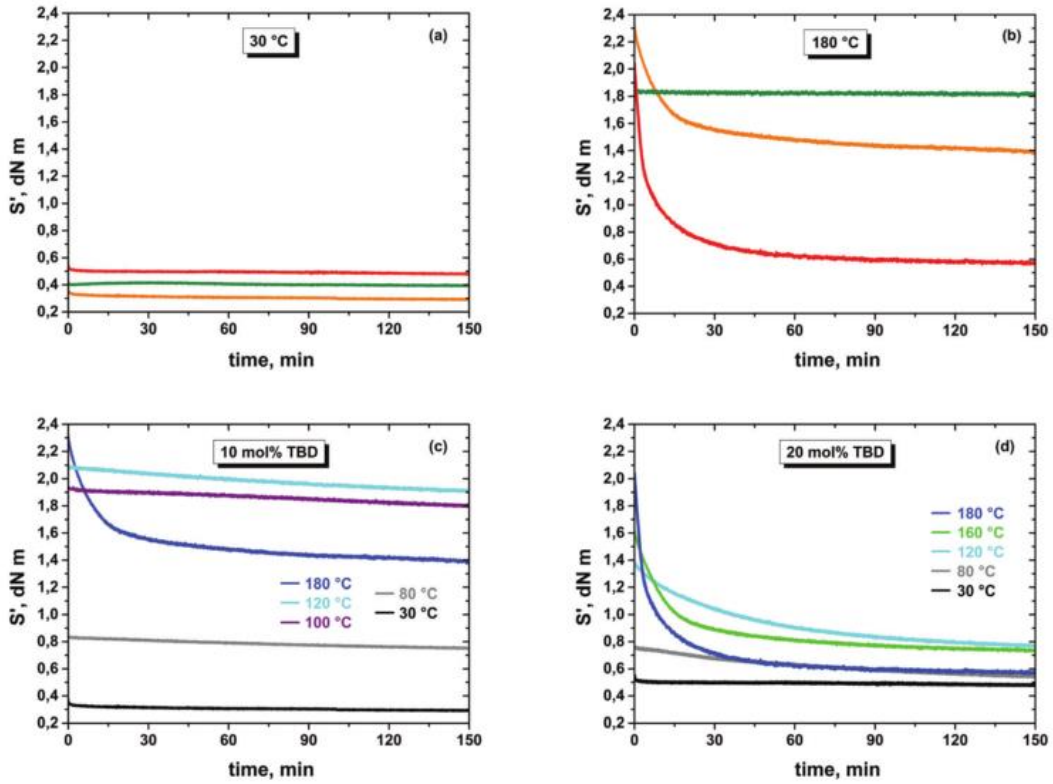


Figure 5. Stress relaxation curves (torque over time) for: HXNBR without TBD (green curve), with 10 mol% of TBD (orange curve) and with 20 mol% of TBD (red curve) at 30°C (a) and 180°C (b); HXNBR with 10 mol% (c) and 20 mol% (d) of TBD at different temperature steps. Used with permission of Royal Society of Chemistry, from "*S. Kaiser, S. Wurzer, G. Pilz, W. Kern, S. Schlögl, Stress relaxation and thermally adaptable properties in vitrimer-like elastomers from HXNBR rubber with covalent bonds, Soft Matter 15(30) (2019) 6062-6072"*; permission conveyed through Copyright Clearance Center, Inc.

An alternative to transesterification in order to prepare associative CANs has been proposed with transamination [9-11]. In 2015 Denissen *et al.* reported the preparation of a catalyst-free poly(vinylogous urethane) dynamic network [9]. In Figure 6, the different exchange reaction scheme, compared to transesterification, is shown.

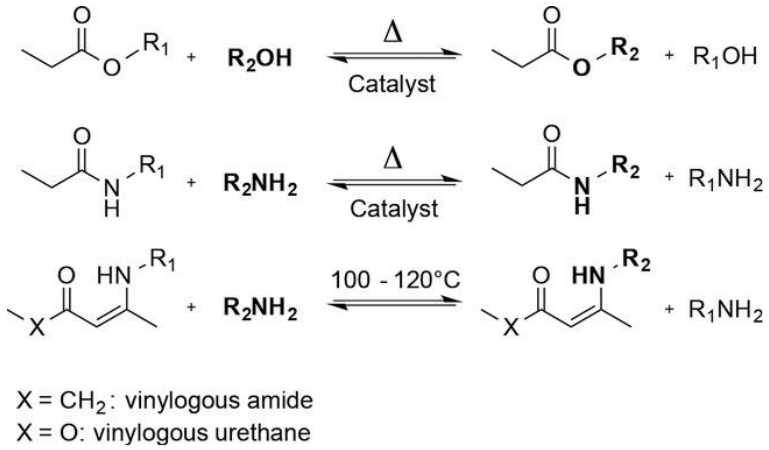


Figure 6. Scheme of transesterification, transamidation and transamination reactions of vinylogous amides and urethanes. Reprinted with permission from "*W. Denissen, G. Rivero, R. Nicolaÿ, L. Leibler, J.M. Winne, F.E. Du Prez, Vinylogous urethane vitrimers, Advanced Functional Materials 25(16) (2015) 2451-2457*". Copyright 2015 WILEY-VCH Verlag GmbH & Co. KGaA, Weinheim.

The authors reported the formation of a rearrangeable covalent network, insoluble at both room temperature and high temperature. The network flow, thanks to the transamination reactions, is clearly evidenced by stress relaxation tests (Figure 7 (a)): again, increasing temperature (here from 130°C to 170°C) brings to shorter relaxation time, thanks to the enhanced exchange reaction kinetic. The activation energy of the process, calculated by the trend of stress relaxation times on temperature, is assessed at 59 kJ/mol. The authors reported also that it was possible to grind and hot-press the samples again, preserving stiffness, tensile strength and elongation at break in tensile testing (Figure 7 (b)).

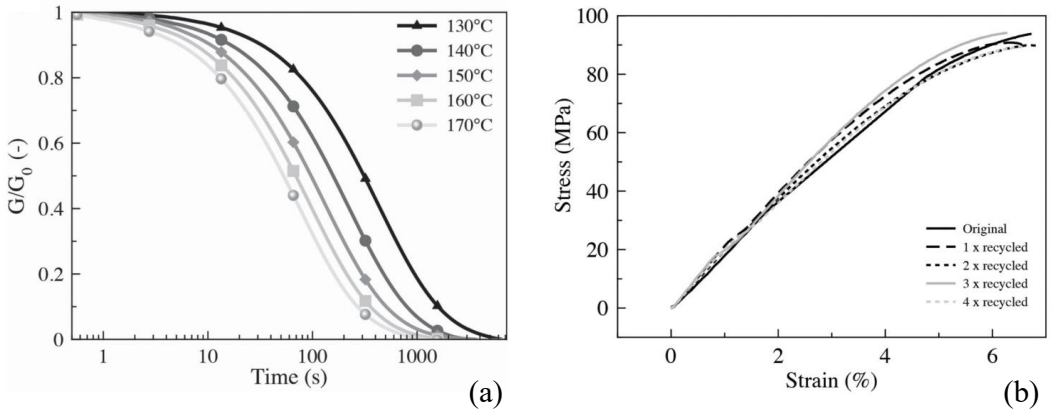


Figure 7. Normalized stress relaxation curves at different temperatures (a) and stress–strain curves of the recycled samples (b). Reprinted with permission from "*W. Denissen, G. Rivero, R. Nicolaÿ, L. Leibler, J.M. Winne, F.E. Du Prez, Vinylogous urethane vitrimers,*

*Advanced Functional Materials 25(16) (2015) 2451-2457*". Copyright 2015 WILEY-VCH Verlag GmbH & Co. KGaA, Weinheim.

Another example of vitrimer comes again from Leibler's group, this time exploiting a catalyst-free dioxaborolane metathesis exchange reaction [13]: Rottger *et al.* reported this work where they prepared vitrimers both via copolymerization of the required macromolecule and via group-grafting on commercial polymers (PMMA, PS and HDPE) via reactive melt processing, adding an interesting industrially viable contribute to their work. These two approaches are outlined in Figure 8.

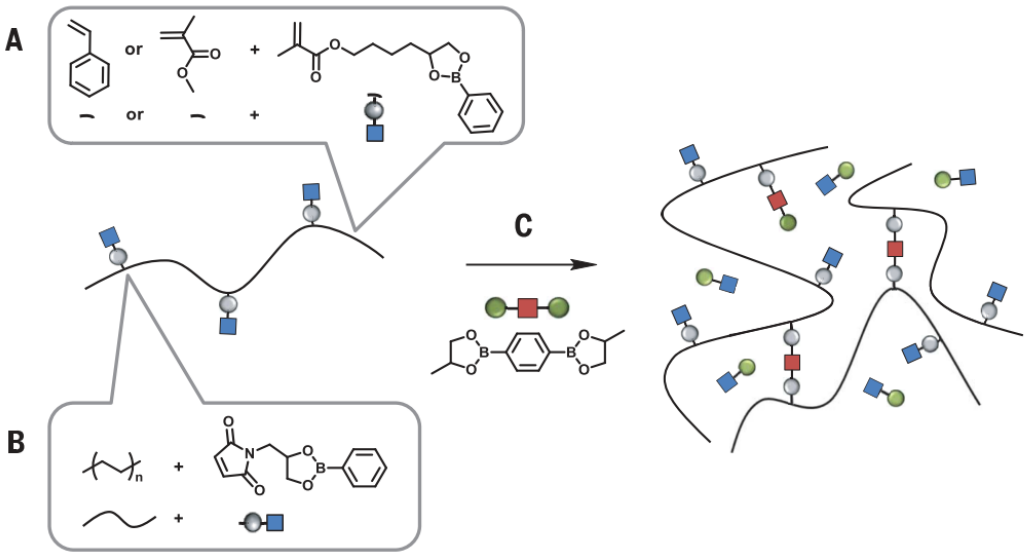


Figure 8. Synthesis of copolymers containing pendant dioxaborolanes from functional monomers (a). Grafting of dioxaborolanes onto thermoplastic polymers by means of reactive processing (b). Crosslinking of functional polymers containing pendant dioxaborolane units by means of metathesis with a bis-dioxaborolane (c). From "*M. Rottger, T. Domenech, R. van der Weegen, A. Breuillac, R. Nicolaÿ, L. Leibler, High-performance vitrimers from commodity thermoplastics through dioxaborolane metathesis, Science 356(6333) (2017) 62-65*". Reprinted with permission from AAAS.

In Figure 9 (a) the stress-relaxation curves for the PMMA vitrimer, at different temperature from 120°C to 160°C, are reported. Here the complex modulus is not normalized, nevertheless it is clear that the relaxation process become faster increasing temperature (higher slope at lower test time), as observed in the previous vitrimer examples. The activation energy for the relaxation of this vitrimer was assessed at 77 kJ/mol. In Figure 9 (b), a picture of injection and compression molded PMMA, PS and HDPE vitrimer samples is shown, reporting the authors capability to melt process these associative CANs. Finally, in Figure 9 (c) tensile strength and elongation at break of HDPE, HDPE vitrimer and recycled HDPE

vitrimer are reported. Tensile strength is not significantly increased by crosslinking, while its elongation at break decreases generating the vitrimer. However, reprocessing the vitrimers is possible and does not affect these mechanical properties, evidencing the rearrangement and flow properties of the vitrimers, generating a new network with mechanical properties similar to the pristine one.

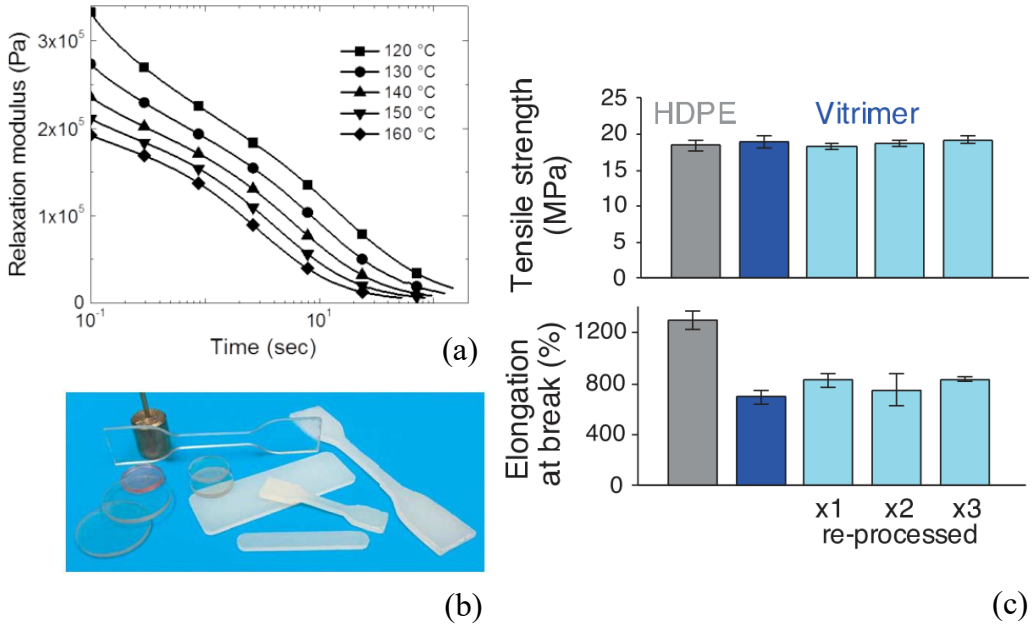


Figure 9. Relaxation tests of PMMA vitrimer at different temperatures, complex modulus over time (a). Injection and compression molded vitrimers: (left) injection-molded PMMA discs and dog-bone samples, (middle) injection molded PS discs, (right) compression molded HDPE bars and dog-bone sample (b). Tensile strength and elongation at break of HDPE, HDPE vitrimer and recycled HDPE vitrimer (c). From "*M. Rottger, T. Domenech, R. van der Weegen, A. Breuillac, R. Nicolaÿ, L. Leibler, High-performance vitrimers from commodity thermoplastics through dioxaborolane metathesis, Science 356(6333) (2017) 62-65*". Reprinted with permission from AAAS.

## 1.1.2. Dissociative Covalent Adaptable Networks

Regarding dissociative CANs based on reversible addition reactions, the network is cleavable thanks to the reversibility character of the reactions involved. In fact, over a certain temperature, since usually these CANs are *thermo*reversible, the crosslinking density drops and the polymer behaves as a thermoplastic or close to. By a rheological point of view, a critical difference in dissociative CANs from their associative homologues is the decrease of the storage modulus G' *plateau* ($G_0$ in Figure 10) related to crosslinking density, as a function of temperature [2, 18]. In fact, classical permanent networks (black solid line in Figure 10) present this

*plateau* until low frequencies, while associative CANs with thermally activated exchange reactions (red dashed line in Figure 10) present a temperature-dependant liquid-like stress relaxation at low frequencies, but their $G_0$ *plateau* is not affected by temperature, because of their network rearrangement process at constant crosslinking density. Instead, dissociative CANs based on thermoreversible addition reactions (blue dashed line in Figure 10) present a similar temperature-dependant liquid-like stress relaxation but shifted at higher frequencies, thanks to the decrease in $G_0$ *plateau*, related to the decrease in crosslinking density with temperature.

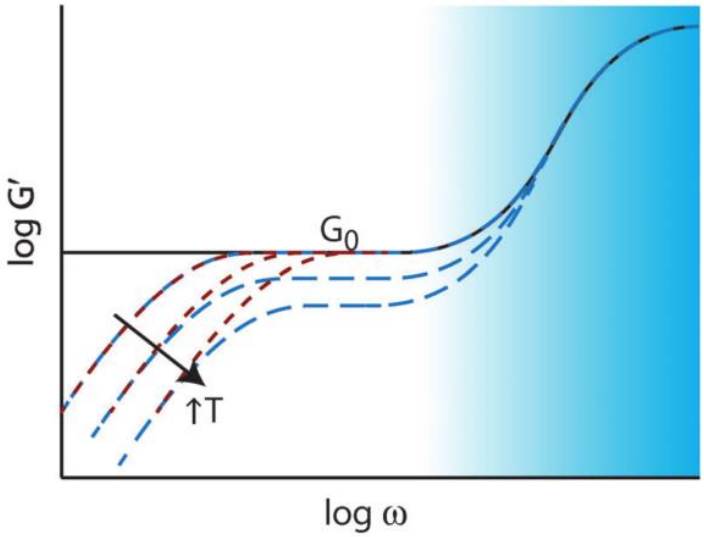


Figure 10. Frequency sweep rheological test curves, with storage modulus versus frequency for a classic thermoset (black solid line), a dissociative CAN based on thermoreversible addition reactions (blue, dashed line) and an associative CAN based on thermally activated exchange reactions (red, dashed line), as a function of temperature. Reprinted from "*C.J. Kloxin, C.N. Bowman, Covalent adaptable networks: smart, reconfigurable and responsive network systems, Chemical Society Reviews 42(17) (2013) 7161-7173*".

There is a wide choice of addition reactions already used in dissociative CANs: nucleophilic addition, dimerization, reversible radical coupling and Diels-Alder (DA) cycloaddition (as outlined in Figure 11). However, some of these present problems of stability, *e.g.* isocyanates (Figure 11 (1)) show sensibility to moisture, while carbenes (Figure 11 (2)) show sensibility to oxidation, or problems of reversibility, *e.g.* the reactivity of active radicals (as the styryl radical in Figure 11 (3)) in undesired side reactions [18].

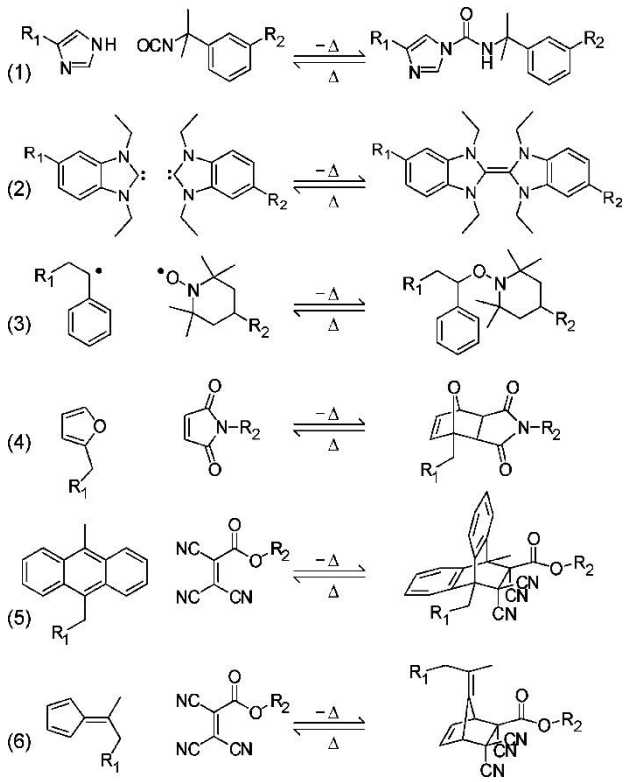

Figure 11. Examples of addition reactions used for thermoreversible crosslinking in dissociative CANs: nucleophilic addition between isocyanate and imidazole (1), carbene dimerization (2), reversible radical coupling between 2,2,6,6-tetramethylpiperidinyl-1-oxy and a styryl radical (3) and the DA cycloadditions between furan and maleimide (4), anthracene and tricyanoacrylate (5) and fulvene and tricyanoacrylate (6). Reprinted with permission from "*C.J. Kloxin, T.F. Scott, B.J. Adzima, C.N. Bowman, Covalent Adaptable Networks (CANs): A unique paradigm in crosslinked polymers, Macromolecules 43(6) (2010) 2643-2653*". Copyright 2010 American Chemical Society.

In this scenario, the best performances in terms of stability to environmental species (as water and oxygen) and reversibility are given by DA cycloaddition reactions (Figure 11 (4, 5, 6)), which in fact has been the most used addition reaction in dissociative CANs preparation [18]. It was 1928 when German Professor Otto Diels and his student Kurt Alder figured out the cycloaddition reaction which since that moment took their names, bringing them the Nobel Prize for chemistry in 1950 [19]. DA reaction is a [4+2] cycloaddition reaction that involves 4+2 electrons, coming from two double bonds (in a molecule or a group called diene) and from one double bond (in a molecule or a group called dienophile), in order to form a cyclic compound (Figure 11 (4, 5, 6)). The diene is a molecule or a group with two conjugated double bonds, while a dienophile is a molecule or a group with one double bond, typically weakened by nearby electron withdrawing atoms, such as oxygen. The feature of this reaction that makes it a powerful choice for dissociative

CANs is its reversibility: while DA reaction is favoured around 50°C (it can take place also at room temperature, but at slower rate [20]) the retro-Diels-Alder (retro-DA) reaction is usually achieved rising temperature above 110°C [20]. This reaction brought a new powerful tool in organic chemistry, since its field of applicability is wide [21-23] and its potential in organic synthesis is even huge, especially in the case of complex molecules [24], thanks to its versatile properties (as the unnecessity of catalysts) which make this reaction really suitable for a clean click-chemistry approach [25].

Before receiving more attention recently, DA reaction was already used with the aim of preparing thermoreversible networks in the late 20$^{th}$ century [26]. As an example, in 1992 Canary and Stevens prepared a crosslinked gel composed of a polystyrene grafted with maleimide groups in the role of dienophiles (Figure 12 (a)) and a copolymer of styrene and maleic anhydride grafted with furan groups in the role of dienes (Figure 12 (b)) [27]. The authors performed the grafting and the crosslinking of the two polymers in solvent (Figure 12 (c)), evidencing the achievement of a reversible crosslinking: in a good solvent for both the polymers, the compound presented gelation and did not dissolved at room temperature, while increasing temperature to 150°C the network cleaved and the gel was dissolved. The authors reported problems of stability of the two polymers, especially for the furan grafted one, which presented irreversible gelation after time, even at room temperature. Indeed, furan ring is reported as a reactive compound, beside DA cycloaddition, including ring-opening via oxidation [28] and hydrolysis [29].

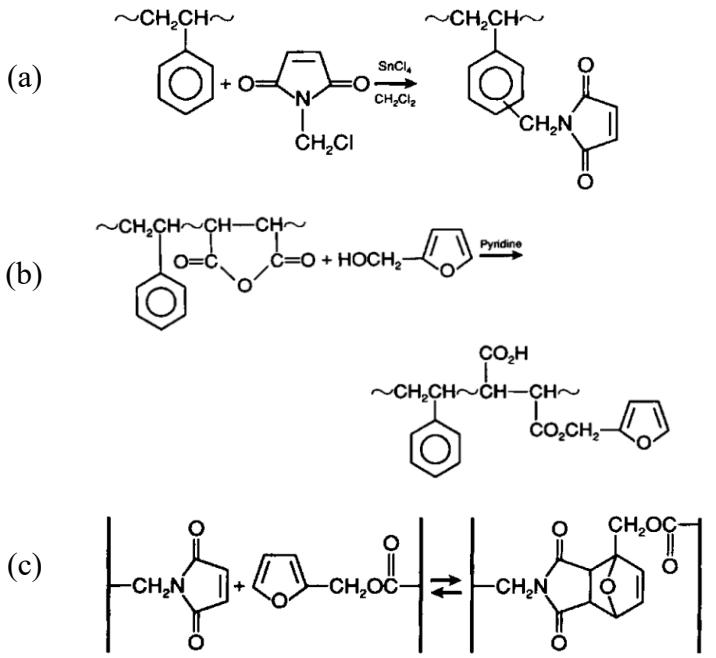


Figure 12. Polystyrene grafted with maleimide groups, in the role of dienophiles (a). Copolymer of styrene and maleic anhydride grafted with furan groups, in the role of dienes (b). DA reaction of crosslinking between maleimide and furan groups (c). Reprinted with permission from "*S.A. Canary, M.P. Stevens, Thermally reversible crosslinking of polystyrene via the furan–maleimide Diels–Alder reaction, Journal of Polymer Science, Part A: Polymer Chemistry 30(8) (1992) 1755-1760*". Copyright 1992 John Wiley & Sons, Inc.

Several other authors realized CANs exploiting DA reaction [30-36]. In 2002 Chen *et al.* realized an epoxy reversible network starting from multifunctional diene and dienophile grafted monomers [30], reporting mechanical properties competitive with commercial crosslinked epoxy resins (Young's modulus of 4.72 GPa and yield strength of 68 MPa). In 2011 Defize *et al.* prepared a thermoreversibly crosslinked polycaprolactone (PCL) starting from tetra-functional star-shaped unities, end-functionalized with furan and maleimide groups (Figure 13) [31].

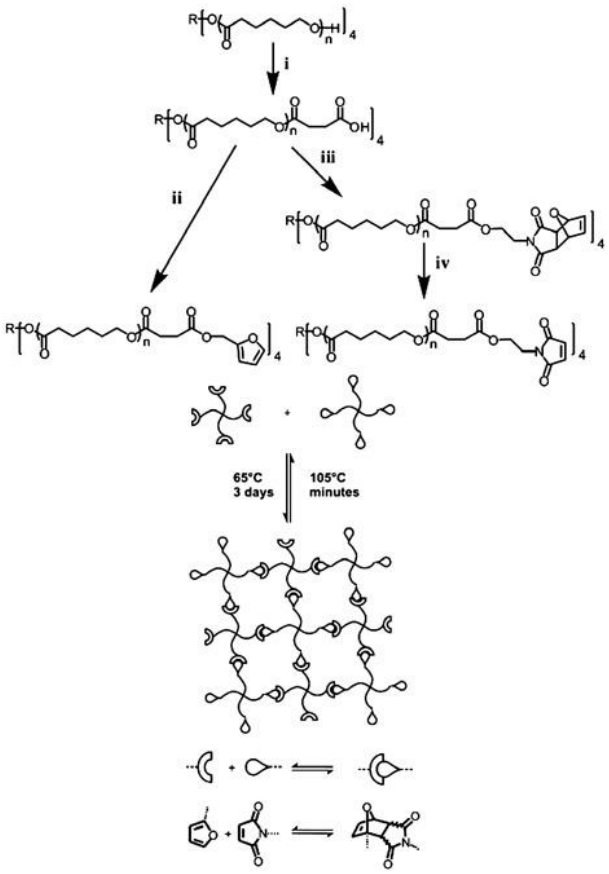


Figure 13. Scheme of PCL reversible network preparation. Reprinted with permission from *"T. Defize, R. Riva, J.M. Raquez, P. Dubois, C. Jerome, M. Alexandre, Thermoreversibly Crosslinked Poly(epsilon-caprolactone) as Recyclable Shape-Memory Polymer Network, Macromolecular Rapid Communications 32(16) (2011) 1264-1269"*. Copyright 2011 WILEY-VCH Verlag GmbH & Co. KGaA, Weinheim.

The authors performed the functionalization of the star-shaped unities with furan groups (Figure 13 (i→ii)) and maleimide groups (Figure 13 (i→iii→iv)) in solvent, then melt blended the two in a mini-extruder at 105°C, finally annealing the product in oven at 65°C for 3 days, in order to complete the DA reaction. The authors evidenced the achieved crosslinking by solubilization test, obtaining in the product a gel fraction of 91.6 wt%, and proved the thermoreversibility of the network chopping some samples and melt processing them again, this time by injection-molding, obtaining new recycled specimens.

In 2015 Polgar *et al.* prepared an ethylene-propylene rubber thermoreversible network, grafting furan groups on the polymer backbone and then generating the network using a bismaleimide (Figure 14), performing the reactions in solvent (THF) [34].

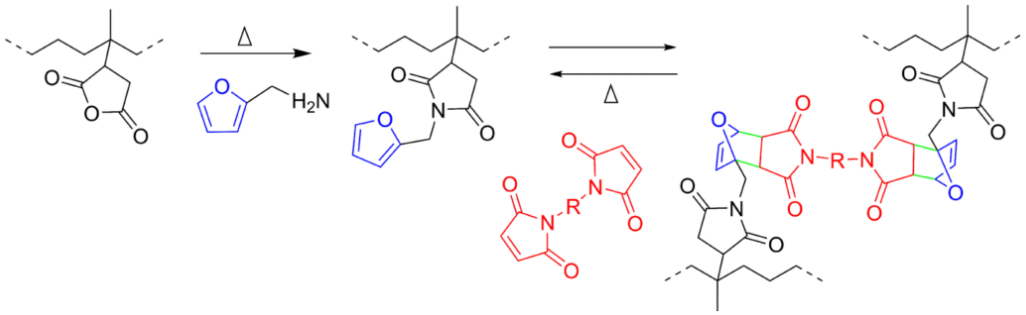

Figure 14. Scheme of furan grafting and DA crosslinking with bismaleimide. Reprinted with permission from *"L.M. Polgar, M. van Duin, A.A. Broekhuis, F. Picchioni, Use of Diels–Alder chemistry for thermoreversible cross-linking of rubbers: The next step toward recycling of rubber products?, Macromolecules 48(19) (2015) 7096-7105"*. Copyright 2015 American Chemical Society.

The authors used furfurylamine to graft the furan (used as diene for DA reaction), reacting with the maleic anhydride groups grafted on the commercial polymer and forming an imide, then reversibly crosslinked the rubber with a bismaleimide, as a bifunctional dienophile for DA reaction. In this way, bismaleimide can play as a crosslinker at room temperature and then opening, cleaving the network, when temperature rises meeting retro-DA conditions. Authors documented the achievement of crosslinking by solubilization test at room temperature and its reversibility increasing the solution temperature to 175°C for 1 h, dissolving the cleaved network (Figure 15 (a)). In Figure 15 (b) and (c) results for tensile tests are reported.

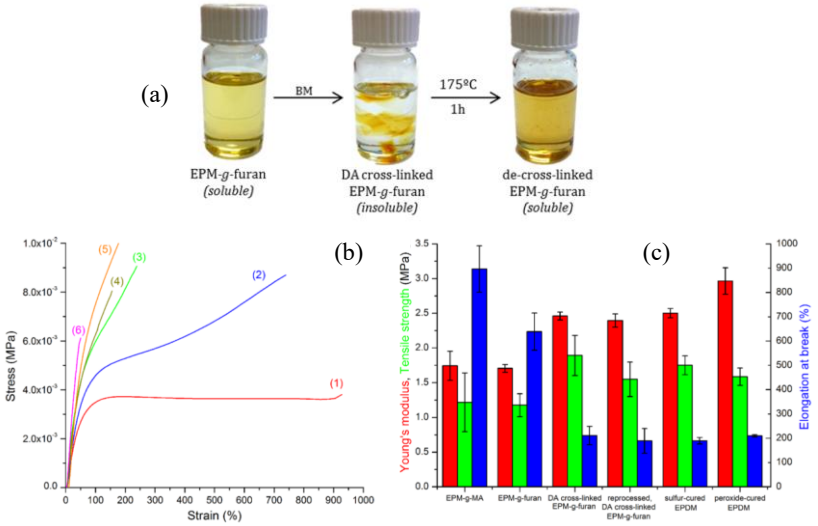


Figure 15. Solubility of non-crosslinked, DA crosslinked and de-crosslinked ethylene-propylene rubber grafted with furan (EPM-g-furan) in decalin (a). Tensile test results for the pristine rubber EPM-g-MA (1), EPM-g-furan (2), DA crosslinked EPM-g-furan (3),

and reprocessed, DA crosslinked EPM-g-furan (4) together with sulfur-cured (5) and peroxide-cured (6) EPDM: median stress−stain graphs (b) and the corresponding Young's modulus, tensile strength, and elongation at break (c). Adapted with permission from *"L.M. Polgar, M. van Duin, A.A. Broekhuis, F. Picchioni, Use of Diels–Alder chemistry for thermoreversible cross-linking of rubbers: The next step toward recycling of rubber products?, Macromolecules 48(19) (2015) 7096-7105"*. Copyright 2015 American Chemical Society.

Results show a clear increase in stiffness and tensile strength, together with the decrease of elongation at break, compared to the non-crosslinked polymers, reporting a typical behaviour for networks. Moreover, a recycled sample does not show substantial changes in terms of tensile strength, stiffness and elongation at break. The authors compared these results also with two permanently crosslinked samples of the same rubber (sulfur-cured and peroxide-cured), showing, despite a slightly higher stiffness especially for the peroxide-cured rubber, similar tensile strength and elongation at break compared to the thermoreversible networks.

Another example of a rubber dissociative CAN came from Bai *et al.*, who in 2015 prepared a thermoreversibly crosslinked polybutadiene [35]. The authors used a similar approach to Polgar *et al.,* this time using furfuryl mercaptan to graft furan groups on the polybutadiene double bonds via thiol-ene reaction, then crosslinking with bismaleimide. The authors evidenced the achievement of network forming via solubilization test at room temperature (Figure 16) and its thermoreversibility via re-molding and solubilization test at 160°C.

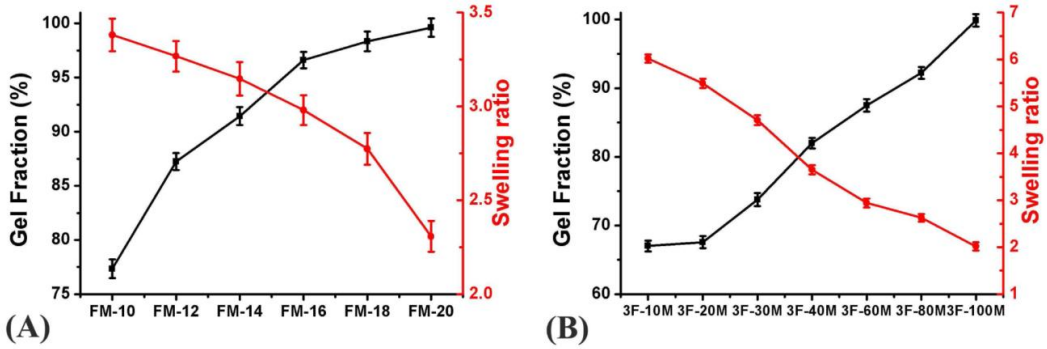


Figure 16. Gel fraction and swelling ratio for two reversibly crosslinked polybutadiene rubbers series: with a furan:maleimide molar ratio of 1:1 and increasing furan grafting on the polymer chain (from 10 to 20 mol%, compared to double bonds of polybutadiene) (a); with fixed furan grafting of 30 mol% and increasing maleimide content (furan:maleimide molar ratio from 1:0.1 to 1:1) (b). Reprinted with permission from *"J. Bai, H. Li, Z. Shi, J. Yin, An Eco-Friendly Scheme for the Cross-Linked Polybutadiene Elastomer via Thiol–Ene and Diels–Alder Click Chemistry, Macromolecules 48(11) (2015) 3539-3546"*. Copyright 2015 American Chemical Society.

It's worth to notice that the authors prepared several crosslinked network with different parameters: a set of rubbers with a furan:maleimide molar ratio of 1:1 and different levels of furan grafting on the polymer chain (from 10 to 20 mol%, compared to double bonds of polybutadiene) and another set with fixed furan grafting of 30 mol% and several furan:maleimide molar ratios (from 1:0.1 to 1:1). The corresponding measured gel fractions for these two sets of crosslinked rubbers are shown in Figure 16 (a) and (b), respectively. The authors observed a progressive increase in the gelled crosslinked portion, both with fixed furan:maleimide ratio and increasing furan grafting (gel fraction from about 77% to 99%, Figure 16 (a)) than with fixed furan grafting and increasing maleimide content (gel fraction from 67% to 99%, Figure 16 (b)), indicating than in both cases the crosslinking degree is related to the maximum amount of furan-maleimide couples available.

## 1.2. Composites and nanocomposites

After presenting examples of associative and dissociative CANs, in this section the possibility to add fillers to a rearrangeable network, preparing so composites or nanocomposites, are explored, using again the same classification for associative and dissociative matrices. Besides simply adding fillers to a CAN matrix, generating a CAN composite presents the opportunity, explored by several authors, to involve fillers in the process of crosslinking and rearrangement of the material.

### 1.2.1. Associative Covalent Adaptable Networks composites

In this subsection some examples of associative CANs composites, so polymeric composites that present a rearrangeable crosslinking via exchange reaction, are presented: *e.g.* the widest used reaction for vitrimers, transesterification, has been used to prepare nanocomposites with cellulose nanofibers [37], with previously functionalized silica nanoparticles [38] or carbon nanotubes [39]. Lossada *et al.* prepared an associative CAN nanocomposite sintering previously prepared poly(dimethylsiloxane) vitrimer nanoparticles mixed with Cellulose NanoFibers (CNF) in an aqueous solution, then removing the solvent via evaporation and curing the obtained films at 120°C (process outlined in Figure 17 [37]).

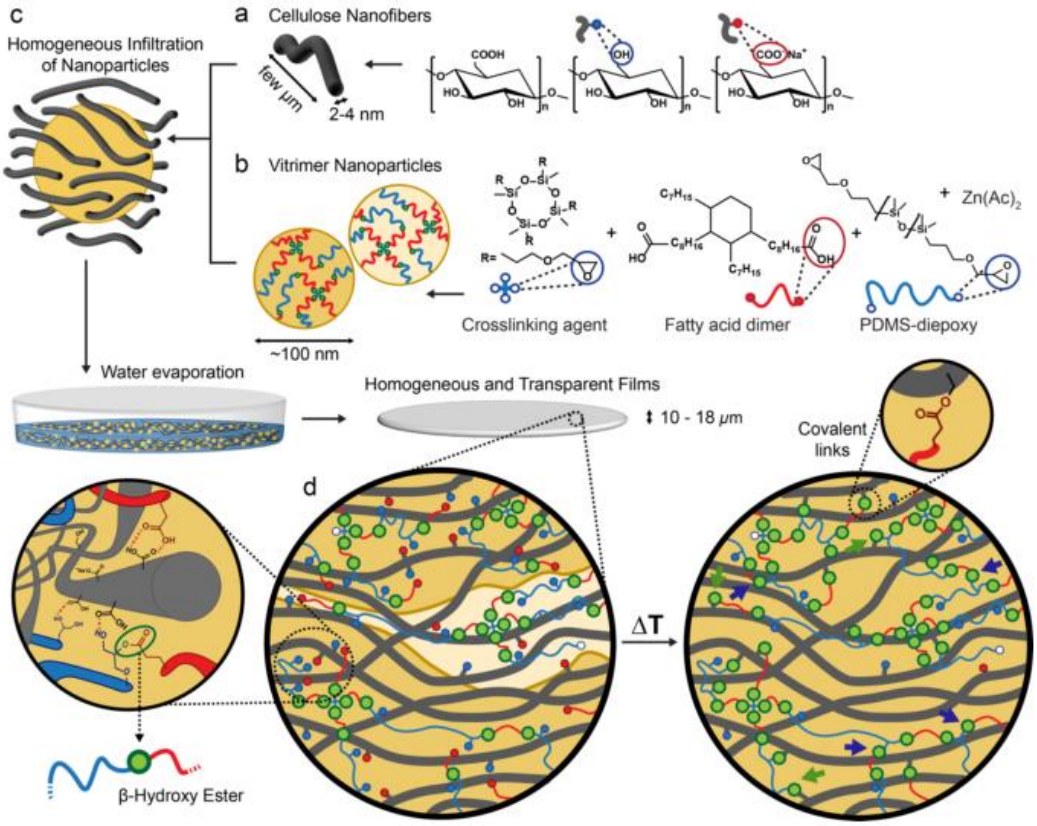


Figure 17. Schematic preparation route of cellulose nanofibers/poly(dimethylsiloxane) vitrimer nanocomposites, with transesterification exchange reaction between the filler and the matrix. Reprinted with permission from *"F. Lossada, J. Guo, D. Jiao, S. Groeer, E. Bourgeat-Lami, D. Montarnal, A. Walther, Vitrimer Chemistry Meets Cellulose Nanofibrils: Bioinspired Nanopapers with High Water Resistance and Strong Adhesion, Biomacromolecules 20(2) (2019) 1045-1055".* Copyright 2018 American Chemical Society.

In the prepared nanocomposites, the vitrimer matrix is also covalently grafted to the cellulose nanofibers, via the esterification of carboxylic acid in the fatty acid dimers, present in the vitrimer formulation (Figure 17 (b)), with the alcohol groups on cellulose (Figure 17 (a) and (c)). This results in a nanocomposite with exchangeable crosslinks both in the poly(dimethylsiloxane) vitrimer matrix and at the matrix/cellulose interface. The strong interfacial adhesion between matrix and filler was evidenced by the author by Scanning Electron Microscopy (SEM) micrographs (Figure 18): in the composite before thermal curing the pull-out of CNF is clearly visible (Figure 18 (b)), while in the cured composite (Figure 17 (d)) the cross-section of the composite appears free of pulled-out cellulose nanofibers, suggesting a strong interaction with the matrix via the ester bonds. The authors also

underlined the hydrophobic character of the obtained composite films, despite the presence of the hydrophilic CNFs thanks to the poly(dimethylsiloxane) matrix.

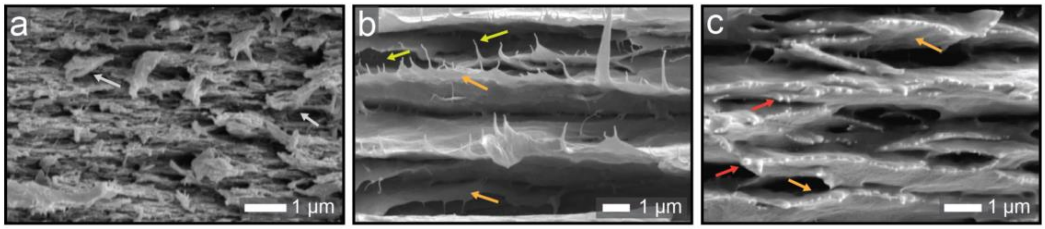


Figure 18. SEM micrographs of fractured samples of cellulose nanofibers (a), the not-sintered cellulose nanofibers/poly(dimethylsiloxane) vitrimer nanoparticles (b) and the sintered nanocomposite (c). Reprinted with permission from *"F. Lossada, J. Guo, D. Jiao, S. Groeer, E. Bourgeat-Lami, D. Montarnal, A. Walther, Vitrimer chemistry meets cellulose nanofibrils: bioinspired nanopapers with high water resistance and strong adhesion, Biomacromolecules 20(2) (2019) 1045-1055".* Copyright 2018 American Chemical Society.

Legrand *et al.* prepared a vitrimer nanocomposite incorporating epoxy-functionalized silica nanoparticles (Figure 19 (1)) in a vitrimer matrix (composed by fatty acids and DGEBA, Figure 19 (2)).

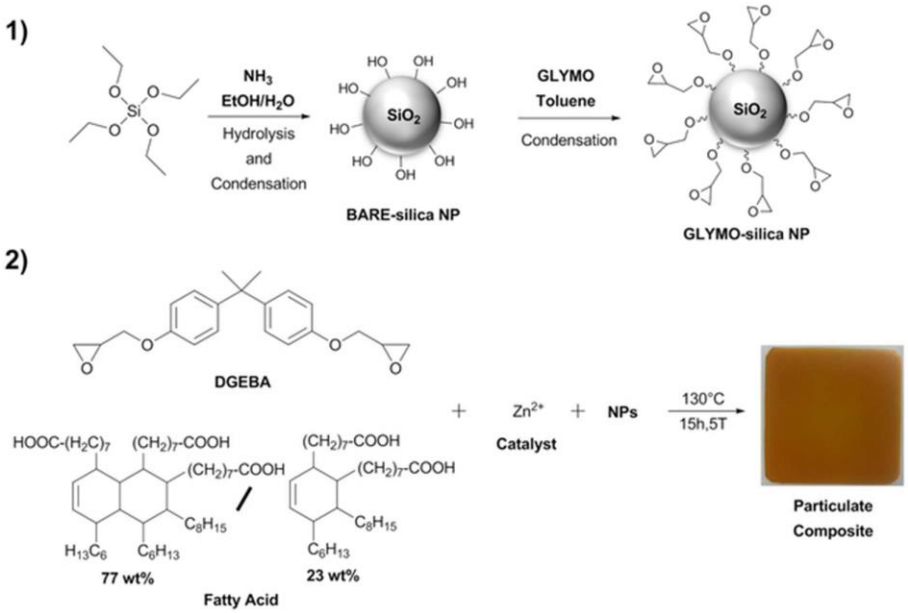


Figure 19. Scheme of synthesis and functionalization of silica nanoparticles (1) and of composite formulation (2). Reprinted with permission from *"A. Legrand, C. Soulié-Ziakovic, Silica–epoxy vitrimer nanocomposites, Macromolecules 49(16) (2016) 5893-5902".* Copyright 2016 American Chemical Society.

The authors obtained a nanocomposite with enhanced stiffness but reduced tensile strength and elongation at break compared to the reference vitrimer matrix

(black and red curves with 25 wt%, solid, and 40 wt%, dashed, of silica nanoparticles, compared to blue curve, Figure 20 (a)). Nevertheless, the crosslinking contribute brought by the epoxy-functionalized silica nanoparticles is evidenced by their reinforcing effect, with a slight tensile strength increasing for both 25 wt% and 40 wt% formulations (red curves) compared to the reference non-functionalized silica nanocomposites (black curves). Besides, the authors reported the ability of the network to rearrange and flow by relaxation tests at 190°C (Figure 20 (b)), where the presence of nanoparticles slows down the relaxation process.

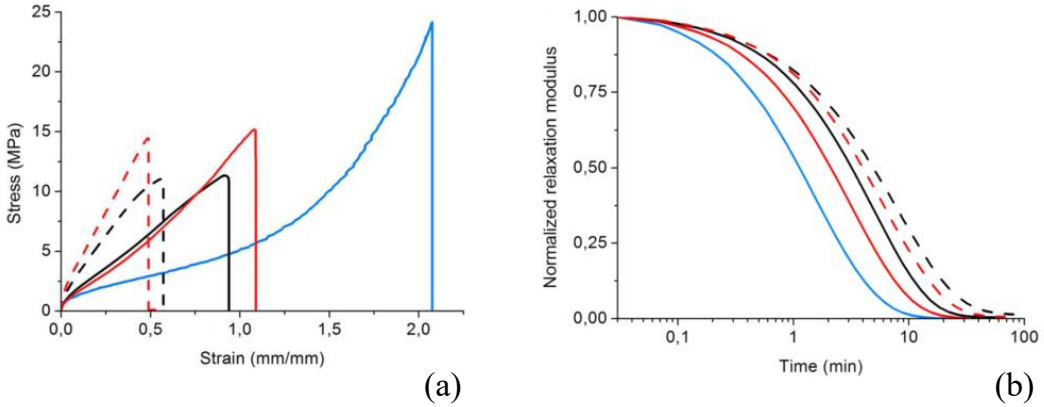


Figure 20. Stress-strain (a) and relaxation test (b) curves obtained for the vitrimer matrix (blue), the reference nanocomposite with not-functionalized silica (black) and the nanocomposite with epoxy-functionalized silica (red) (25 wt% solid line; 40 wt% dashed line). Adapted with permission from *"A. Legrand, C. Soulié-Ziakovic, Silica–epoxy vitrimer nanocomposites, Macromolecules 49(16) (2016) 5893-5902"*. Copyright 2016 American Chemical Society.

Beside CANs, networks based on ionic bonds were also explored: Odent *et al.* prepared a dynamic network system based on ionic reactions [40]; the system is based on mixing oligomers of polylactide (PLA, blue in Figure 21 scheme) and poly[ε-caprolactone-co-D,L-lactide] (P[CL-co-LA], red in Figure 21 scheme) together with commercial PLA and a sulfonate-functionalized silica.

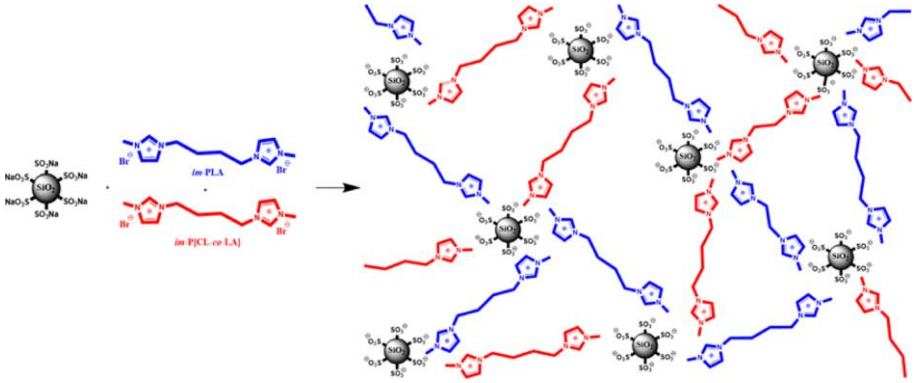

Figure 21. Scheme of ionic rearrangeable nanocomposites made of PLA and imidazolium-terminated PLA (blue) and P[CL-co-LA] (red) oligomers with sulfonated silica nanoparticles. Reprinted with permission from *"J. Odent, J.-M. Raquez, C. Samuel, S. Barrau, A. Enotiadis, P. Dubois, E.P. Giannelis, Shape-Memory Behavior of Polylactide/Silica Ionic Hybrids, Macromolecules 50(7) (2017) 2896-2905".* Copyright 2017 American Chemical Society.

The authors reported the achievement of an ionic network by rheological measures (Figure 22), where the lower slope at low frequencies in the composites with 5 wt% of sulfonated silica nanoparticles and different contents of imidazolium-terminated PLA (10 wt%, green curve, 30 wt%, blue curve, 50 wt%, red curve), compared to a reference nanocomposite with 5 wt% of sulfonated silica nanoparticles but without ionic oligomers, is related to a typical network behaviour. Moreover, this ionic system guarantees an optimal distribution of the filler in the matrix, compared to the reference PLA nanocomposite (TEM micrographs in Figure 22).

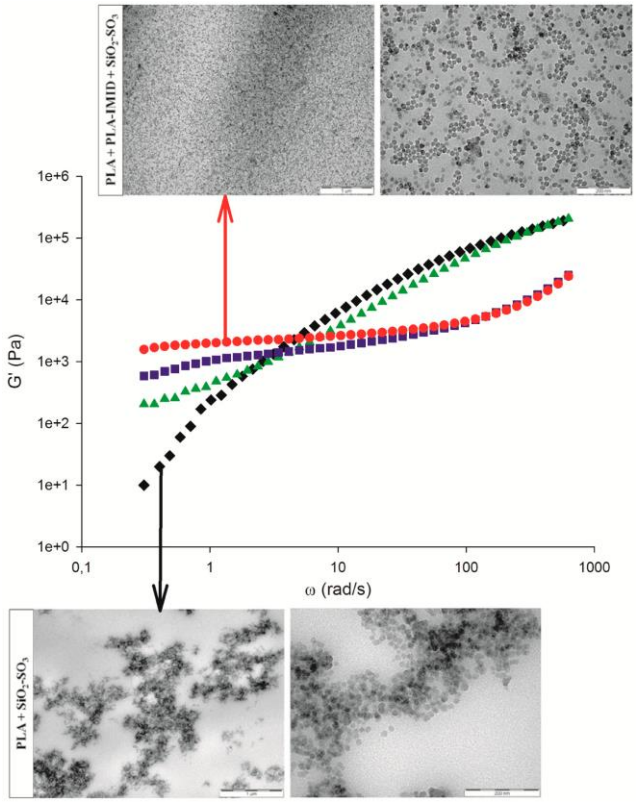


Figure 22. Frequency sweep test: storage modulus G′ at 180 °C for the reference PLA based nanocomposite with 5 wt% of silica nanoparticles (black) and for the nanocomposites containing 10 wt% (green), 30 wt% (blue) and 50 wt% (red) of imidazolium-terminated PLA oligomers. Cross-sectional TEM micrographs (with scales of 1 µm (left) and 200 nm (right)) for the reference nanocomposite based on PLA (bottom) and 50 wt% of imidazolium-terminated PLA oligomers (top) are also included. Reprinted with permission from *"J. Odent, J.-M. Raquez, C. Samuel, S. Barrau, A. Enotiadis, P. Dubois, E.P. Giannelis, Shape-Memory Behavior of Polylactide/Silica Ionic Hybrids, Macromolecules 50(7) (2017) 2896-2905"*. Copyright 2017 American Chemical Society.

The authors proposed also this interesting ionic system using the sulfonated silica nanoparticles but grafting the imidazolium groups on a polyurethane chain, with the aim of extending this design to a wider class of polymer systems [41].

## 1.2.2. Dissociative Covalent Adaptable Networks composites

DA reaction is the most widely used addition reaction in dissociative CANs, thanks to its outstanding properties in terms of stability and reversibility [18]. Regarding DA reaction, authors' interest has been attracted by the possibility to perform this cycloaddition not only between molecules and groups, as seen so far, but also between molecules or groups and the sites of $sp^2$ hybridized carbon particles. This topic started in 2002 with the theoretical work of Lu *et al.* [42], which

explored the dienophile nature of single-wall carbon nanotubes and the possibility of grafting diene molecules via DA reaction (Figure 23).

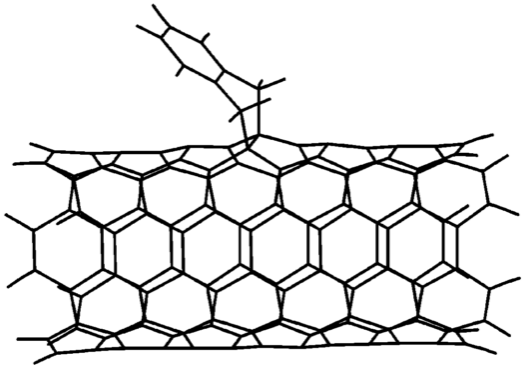

Figure 23. Scheme of DA grafting of a diene (quinodimethane) on a single-wall carbon nanotube. Reprinted with permission from *"X. Lu, F. Tian, N. Wang, Q. Zhang, Organic functionalization of the sidewalls of carbon nanotubes by diels-alder reactions: a theoretical prediction, Organic letters 4(24) (2002) 4313-4315".* Copyright 2002 American Chemical Society.

The authors underlined that the reaction is favoured by the curvature of the carbon surface, thanks to the increased reactivity of the sites. In 2010 Munirasu *et al.* performed a large experimental work, reporting the achievement of grafting on single- and multi-wall carbon nanotubes of several diene and dienophile species, evidencing the double nature of the sites on these nanofiller as both dienophile and diene, respectively [43]. Moreover, the point of the higher reactivity of curved carbon surfaces (as carbon nanotubes) compared to planar carbon surfaces (as graphene and Graphene Related Materials (GRMs)) was then confirmed in the theoretical work of Willocq *et al.* [44] in 2016, who reported lower reaction activation energies for DA reaction increasing the surface curvature. This principle can explain why the evolution of DA functionalization of carbon fillers started with single-wall carbon nanotubes [45-47], then multi-wall carbon nanotubes [43, 48, 49] and Herringbone carbon nanofibers [43], and finally more recently on graphene and GRMs [50].

GRMs are indeed of interest for the preparation of polymer nanocomposites, coupling the benefits typical of lamellar nanoparticles (e.g. gas barrier and mechanical properties) with the intrinsic thermal and electrical conductivity of sp2 carbon nanostructures [51-54]. In this thesis, GRM are therefore addressed as nanofillers for the reinforcement of dissociative CANs. To exploit GRM within the formation of the dissociative networks, both DA functionalization with diene and dienophile species may be exploited in principle, either with small molecules or

with functional polymers. The state of the art on DA functionalization of graphite and GRM is discussed hereunder.

**Diels-Alder reaction on Graphene Related Materials and graphites**

Houk *et al.* [55] and Denis [56] focused on the theoretical study of DA reaction on graphene, calculating the activation energies for both dienophile and diene model species to react on the plane or on defects, as edges. Houk *et al.* [55] concluded that the reaction should not be possible on basal planes and could be rarely possible on edges, so weak interactions between these species and graphene are dominants without a real covalent DA grafting. Nevertheless, Denis [56] concluded the achievement of the reaction both on basal plane and defects of graphene is possible, despite its endergonicity.

By an experimental point of view, covalent functionalization of GRMs through DA cycloaddition reaction was reported for the first time in 2011 with the pioneering work by Sarkar *et al.* [50]. The authors performed the grafting of different species, both dienes and dienophiles, on different carbon substrates (exfoliated graphene (XG), epitaxial graphene (EG), highly oriented pyrolytic graphite (HOPG)) evidencing the double nature of sites on these GRMs as, respectively, dienophile and diene, as outlined in Figure 24.

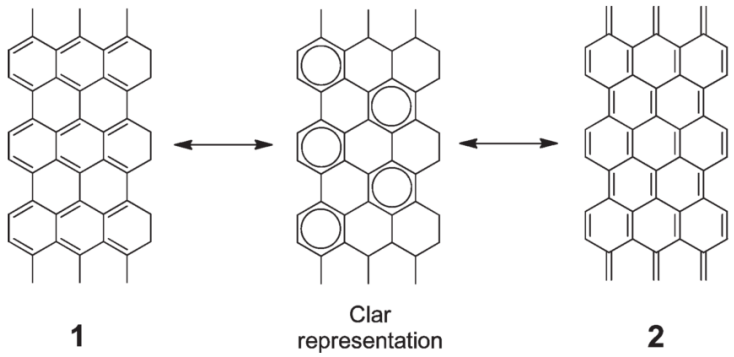


Figure 24. Resonance forms of graphene: as diene (1) and dienophile (2). Reprinted with permission from "*S. Sarkar, E. Bekyarova, S. Niyogi, R.C. Haddon, Diels-Alder chemistry of graphite and graphene: graphene as diene and dienophile, Journal of the American Chemical Society 133(10) (2011) 3324-3327*". Copyright 2011 American Chemical Society.

The authors characterized the products via Raman and IR spectroscopies, focusing on a qualitative characterization of the reaction. Regarding the diene nature of the substrates, the authors used tetracyanoethylene (TCNE) and maleic anhydride (MA) as dienophile molecules. Focusing on MA functionalization, the

process was performed in solvent and with heat supply. The scheme of graphene functionalization with maleic anhydride is reported in Figure 25.

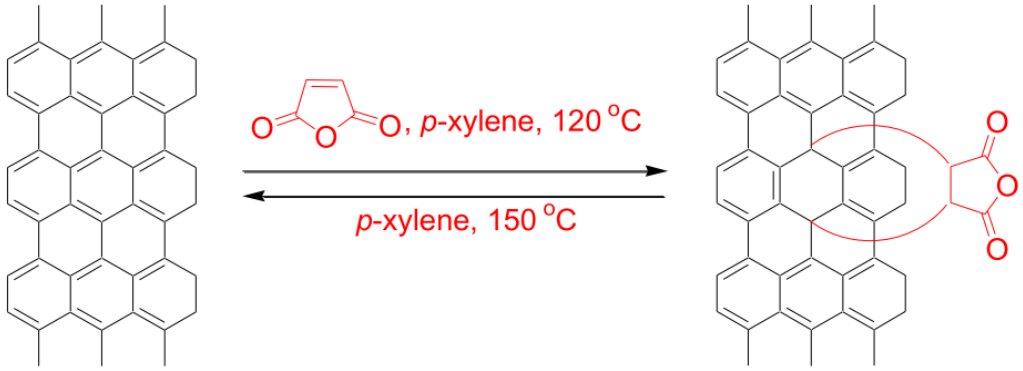


Figure 25. Scheme of DA and retro-DA reactions of MA on HOPG (and in general for GRMs) diene sites. Reprinted with permission from "*S. Sarkar, E. Bekyarova, S. Niyogi, R.C. Haddon, Diels-Alder chemistry of graphite and graphene: graphene as diene and dienophile, Journal of the American Chemical Society 133(10) (2011) 3324-3327*". Copyright 2011 American Chemical Society.

Regarding Raman spectroscopy characterization, success of the reaction is supported by the authors through the rise of the $I_D/I_G$ ratio with the functionalization, related to the increase of defects on graphene (like edges or vacancies) and also to the presence of hybridized $sp^3$ carbons on the basal plane [57]. In Figure 26 the relative spectra for MA functionalization of HOPG at different temperatures are reported.

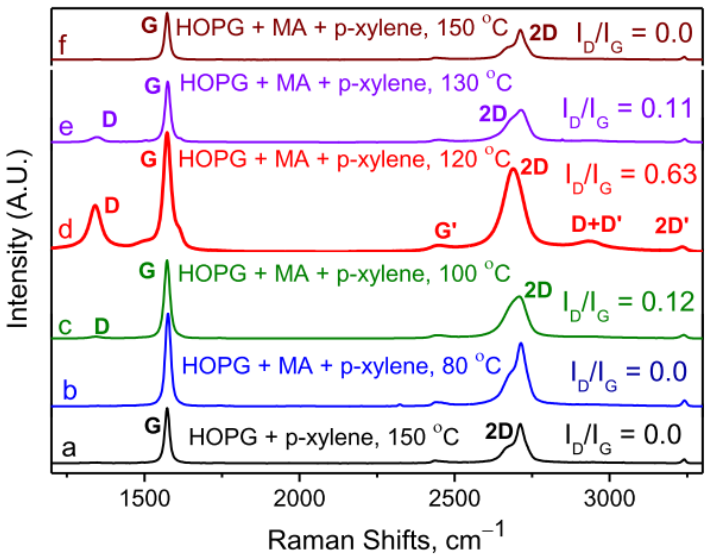


Figure 26. Raman spectra for the reacted MA on HOPG, at different temperatures. Reprinted with permission from "*S. Sarkar, E. Bekyarova, S. Niyogi, R.C. Haddon, Diels-*

*Alder chemistry of graphite and graphene: graphene as diene and dienophile, Journal of the American Chemical Society 133(10) (2011) 3324-3327*". Copyright 2011 American Chemical Society.

In the Raman spectra the ratio $I_D/I_G$ passed from 0.00 at 80°C to 0.63 at 120°C, then to 0.00 again at 150°C; this is consistent with the proceeding of DA grafting of MA on HOPG surface increasing temperature, until retro-DA conditions are reached. In Figure 27 the FT-IR spectra for XG, MA and MA-XG product, are reported.

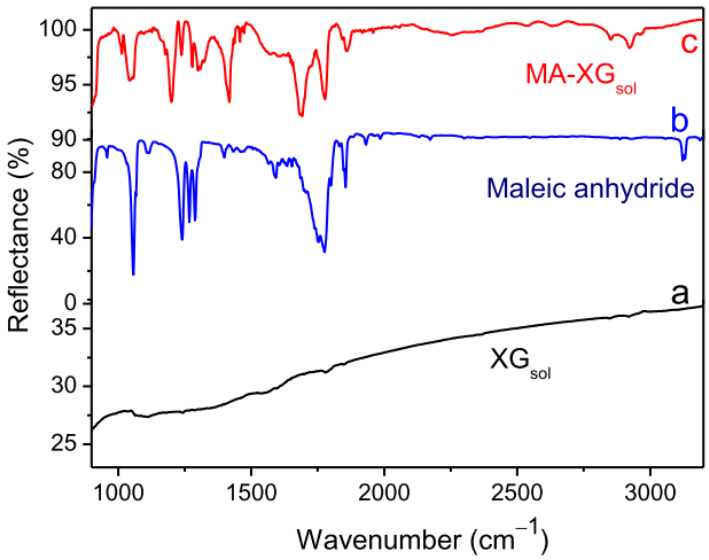


Figure 27. ATR FT-IR spectra of XG (a), MA (b) and MA-XG (c). Reprinted with permission from "*S. Sarkar, E. Bekyarova, S. Niyogi, R.C. Haddon, Diels-Alder chemistry of graphite and graphene: graphene as diene and dienophile, Journal of the American Chemical Society 133(10) (2011) 3324-3327*". Copyright 2011 American Chemical Society.

The most direct evidence of DA reaction achievement on this graphene substrate is the presence of two signals near 2900 $cm^{-1}$ in the FT-IR spectrum of MA-XG. The authors reported that these signals, assigned to C($sp^3$)-H stretching, evidenced the presence of MA carbons bonded to the substrate after functionalization, as a consequence of $sp^2$ to $sp^3$ hybridization conversion (see Figure 25). With the aim of studying the dienophile nature of the substrates, the authors used 9-methylanthra-cene (9-MeA) and 2,3-dimethoxy-1,3-butadiene (DMBD) as dienes. The achievement of the functionalization is supported again with the rise of $I_D/I_G$ ratio in Raman spectroscopy and with FT-IR spectroscopy, in a similar way to the diene part. Focusing on DMDB functionalization, the process was performed in solvent and, for all the substrates, in p-xylene at 120°C. In Figure 28 the scheme of DA and retro-DA reaction of XG with DMDB is reported.

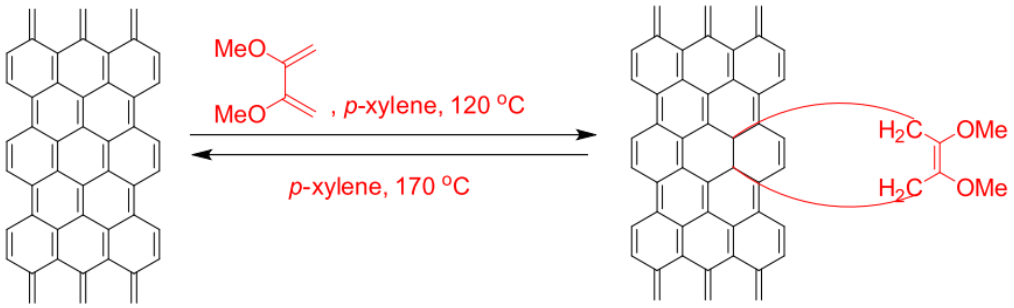


Figure 28. Scheme of DA and retro-DA reactions of DMDB on XG (and in general for GRMs) dienophile sites. Reprinted with permission from "*S. Sarkar, E. Bekyarova, S. Niyogi, R.C. Haddon, Diels-Alder chemistry of graphite and graphene: graphene as diene and dienophile, Journal of the American Chemical Society 133(10) (2011) 3324-3327*". Copyright 2011 American Chemical Society.

Raman spectra evolution of the product DMDB-XG has been followed during the thermal treatment. Spectra of pristine exfoliated graphene (black curve) at room temperature, of the product at 120°C (red curve) and at 170°C (blue curve) are reported in Figure 29.

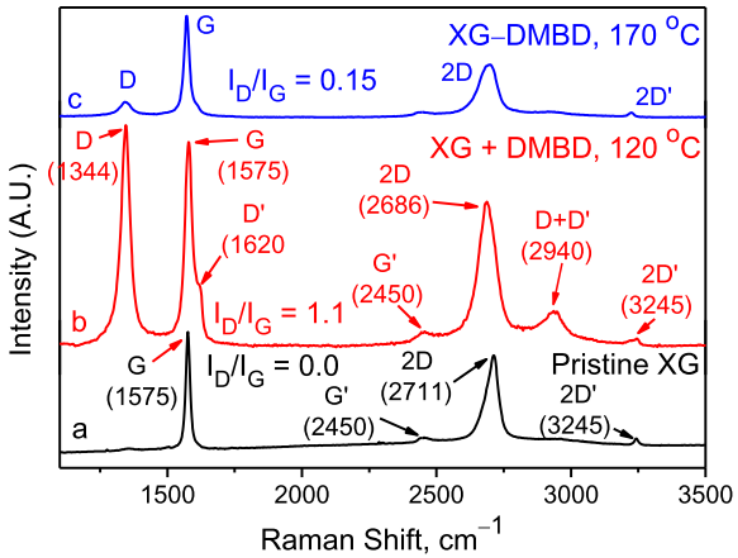


Figure 29. Raman spectra for the reacted DMDB on XG, at different temperatures. Reprinted with permission from "*S. Sarkar, E. Bekyarova, S. Niyogi, R.C. Haddon, Diels-Alder chemistry of graphite and graphene: graphene as diene and dienophile, Journal of the American Chemical Society 133(10) (2011) 3324-3327*". Copyright 2011 American Chemical Society.

It is clear that the D band of Raman spectrum of the product rises dramatically at 120°C (compared to pristine graphene), before dropping at 170°C. Again, the authors used this result to support the achievement of DA functionalization within

120°C and of retro-DA within 170°C. The FT-IR spectrum of exfoliated graphene, DMDB and adduct of both after the functionalization, together with the simplified scheme of the reaction, is reported in Figure 30.

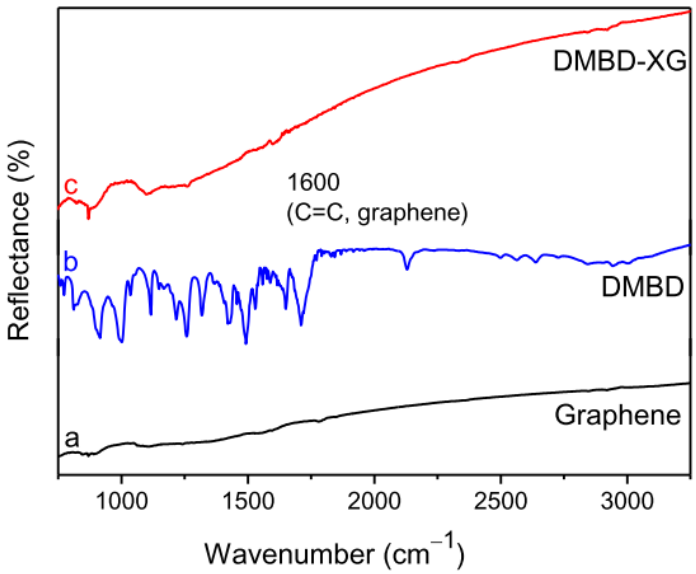


Figure 30. ATR FT-IR spectra of XG, DMDB and DMDB-XG. Reprinted with permission from "*S. Sarkar, E. Bekyarova, S. Niyogi, R.C. Haddon, Diels-Alder chemistry of graphite and graphene: graphene as diene and dienophile, Journal of the American Chemical Society 133(10) (2011) 3324-3327*". Copyright 2011 American Chemical Society.

As in the case of FT-IR spectra of MA-XG, the authors identified two peaks around 2900 $cm^{-1}$ in DMDB-XG spectrum and associated them to $C(sp^3)$-H stretching. Anyway, in this case the evidence of the achieved DA reaction on the substrate appears weaker, due to the presence of other nearby peaks of similar intensity in DMDB spectrum.

Following the above described pioneering work, literature papers took two different paths: DA functionalization on GRMs or graphite with dienophile or diene species, exploiting the diene or dienophile behaviour of the $sp^2$ sites, respectively. Chen *et al.* [58] realized a functionalization of a pristine graphite with acrylic acid as a dienophile. The authors used a thermal treatment in absence of solvents to perform the DA reaction: graphite and acrylic acid (liquid at room temperature) were stirred at 120°C for 36 h, then the residue was washed with DMF, filtered and dried under vacuum. The authors reported grafting evidences from Raman ($I_D/I_G$ rise, as seen above), FT-IR and X-ray Photoelectron Spectroscopy (XPS) spectra (reported in Figure 31). Regarding FT-IR spectra (Figure 31 (a)), the authors

observed that two peaks in acrylic acid spectrum associated to the double bond C=C (3000 $cm^{-1}$, symmetrical stretching vibration of $C=CH_2$ and 1624 $cm^{-1}$, stretching vibration of C=C) disappeared in the reacted graphite (AA@G) spectrum. Moreover, a new signal in the product (1182 $cm^{-1}$) was assigned to the deformation vibration of the ring formed by the cycloaddition. Concerning XPS spectra, the deconvolution of O1s signal in Figure 31 (b) shows the presence of two peaks assigned by the authors to C-O and C=O bonds of acrylic acid on the surface. Anyway, the stronger evidence of the achievement of DA reaction between the molecule and the substrate comes from the deconvolution of C1s signal (Figure 31 (c) for graphite and Figure 31 (d) for AA@G). In the graphite spectrum the two peaks at 284.8 eV and 291.4 eV are assigned to delocalized aromatic $sp^2$ bonds and π-π transition, respectively. In AA@G spectrum, the novel peak at 286.5 eV is assigned to $sp^3$ bonds between graphite and acrylic acid, despite possible homopolymerization of acrylic acid is expected to yield a similar signal.

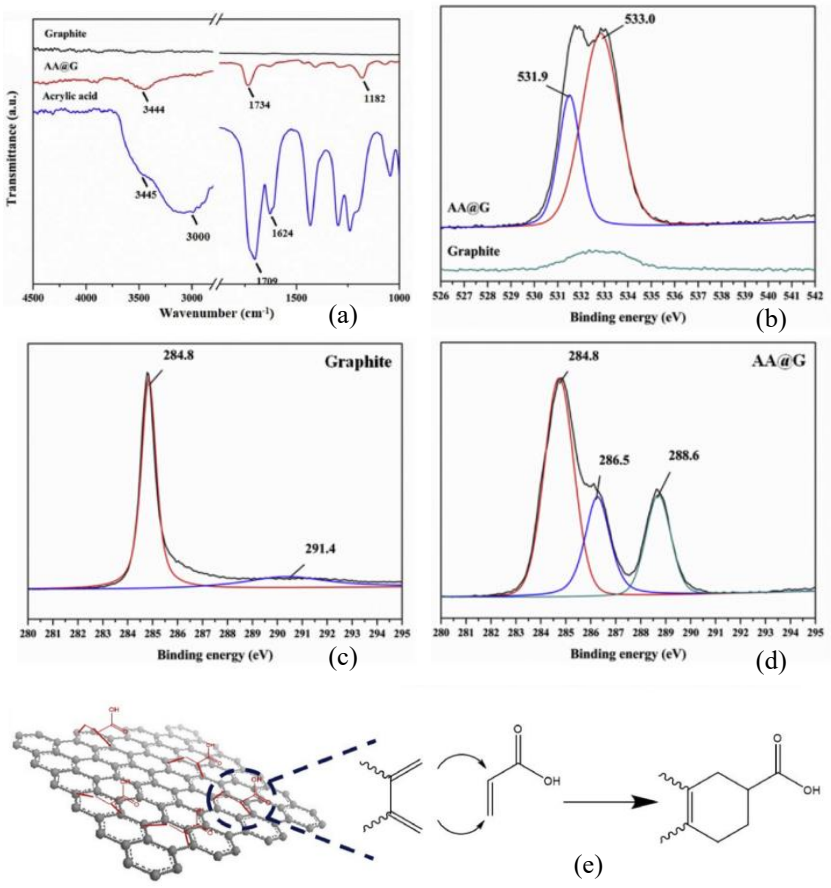


Figure 31. FT-IR spectra of graphite, acrylic acid and AA@G (a). Deconvolution of O1s high resolution XPS spectra for graphite and AA@G. Deconvolution of C1s high resolution XPS spectra for graphite (c) and AA@G (d). Schematic representation of DA

reaction on the graphite substrate (e). Adapted from "*W. Chen, K. Wu, Q. Liu, M. Lu, Functionalization of graphite via Diels-Alder reaction to fabricate poly (vinyl alcohol) composite with enhanced thermal conductivity, Polymer 186 (2020) 122075*", with permission from Elsevier.

Seo *et al.* [59, 60] worked on graphite functionalization with dienophile molecules such as maleic anhydride (MA) or maleimide (MI). The authors started from a mixture in absence of solvent, and performed the process both through a mechanochemically approach [59] via ball milling in inert atmosphere, followed by washing and freeze-drying) or via a thermal process [60] in which the mixtures were heated at 220°C or 160°C, for MA or MI respectively, for 12 h, then washed and freeze-dried. In both cases, the authors claimed that DA reaction occurred exclusively on graphite edges and not on the basal plane, relying on Houk *et al.*'s study [55]. Regarding the mechanochemically approach, the grade of functionalization achieved was investigated by the authors via TGA analysis, and attested at 15.1 wt% for MA and 17.6 wt% for MI. In the case of the thermal approach, the results were much lower: about 1.8 wt% for MA and 1.0 wt% for MI. Raman spectroscopy measures report the raise of $I_D/I_G$ ratio in the functionalized samples: from 0.01 of graphite to 0.62 for MA and 1.04 for MI in the mechanochemically approach, from 0.20 of graphite (different graphites used in the two works) to 0.54 for MA and 0.52 for MI, which is consistent with the TGA obtained values. In the thermal approach the authors reported also a direct evidence of DA reaction with the assignment of two peaks close to 2900 $cm^{-1}$ in FT-IR spectra of maleic anhydride functionalized graphite and maleimide functionalized graphite, associated to $C(sp^3)$-H stretching, as in Sarkar's work [50]. These spectra, together with the one of pristine graphite, are reported in Figure 32.

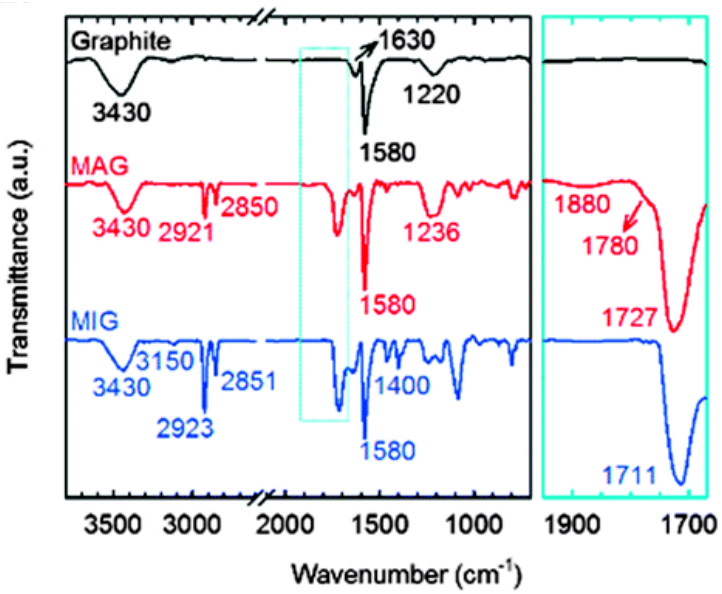


Figure 32. FT-IR spectra of pristine graphite and its adducts with MA (MAG) and maleimide (MIG). Reprinted from "*J.M. Seo, J.B. Baek, A solvent-free Diels-Alder reaction of graphite into functionalized graphene nanosheets, Chemical communications 50(93) (2014) 14651-14653*".

Regarding MA functionalization of Graphite NanoPlates (GNP) through DA reaction, Zabihi *et al.* [61] realized that with a mechanical approach using a "kitchen blender", in order to simplify the process and get closer to an industrial-available approach. Raman spectroscopy, FT-IR spectroscopy and XPS results bring good evidences of the presence of the molecule on the substrate, while its actual covalent grafting remains uncertain.

Regarding the functionalization with diene molecules, Barbera *et al.* [62] worked on the decoration of an High Surface Area nanosized Graphite (HSAG) with 1,2,5-TriMethylPyrrole (TMP), starting from a mixture, in absence of solvents and performing a thermal treatment to achieve the reaction: the mixture of TMP (liquid at room temperature) and HSAG was left for 2 h at different temperatures between 80 and 180°C. Regarding Raman spectroscopy of pristine HSAG and HSAG-TMP, the authors argue that the bulk structure of the graphite should not be altered appreciably by the functionalization; therefore, the authors did not link this feature directly to the degree of functionalization, as previous authors did [50, 58-61]. Regarding other spectroscopy measures, the authors obtained two strong and direct evidences of the reaction from FT-IR and XPS. In Figure 33, the FT-IR spectra evolution of HSAG-TMP mixture at different temperatures during the thermal treatment is reported. It is possible to see the peaks associated to C=C

stretching (at 1516 $cm^{-1}$) and to the breathing vibration of the pyrrole ring (at 1301 $cm^{-1}$) becoming very weak with the advance of the thermal treatment. The authors correlated this behaviour to the achievement of the DA grafting.

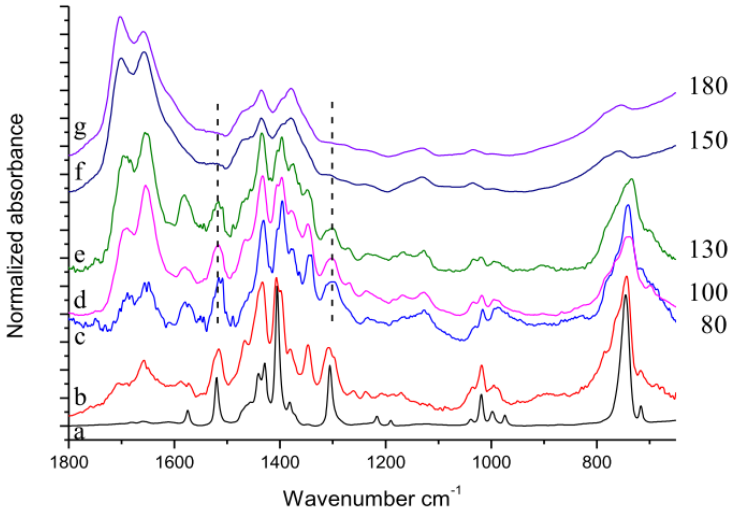


Figure 33. FT-IR spectra of TMP (a), TMP treated in air at 130°C (b), HSAG/TMP mixture in equimolar amount treated at different temperature (c)-(g). Reprinted from *"V. Barbera, L. Brambilla, A. Milani, A. Palazzolo, C. Castiglioni, A. Vitale, R. Bongiovanni, M. Galimberti, Domino reaction for the sustainable functionalization of few-layer graphene, Nanomaterials 9(1) (2018) 44"*.

In Figure 34 the XPS spectra of N1s signal for HSAG-TMP mixture at different temperatures, together with the scheme of the reaction, are reported. In the deconvolution of the N1s signal (Figure 34 (a)) it is possible to see the peak assigned to C($sp^3$)-N bond rising, compared to the C($sp^2$)-N one. The authors linked this behaviour to the realization of covalent bonds between two carbon atoms of TMP and the sites on HSAG substrate, via DA reaction, as outlined in Figure 34 (b) (the authors also hypothesizes a possible oxidation of TMP, likely even catalysed by HSAG substrate). These evidences together bring good support to the achievement of DA grafting of a diene on graphite, similarly to the case of a dienophile (acrylic acid) in the above presented work [58].

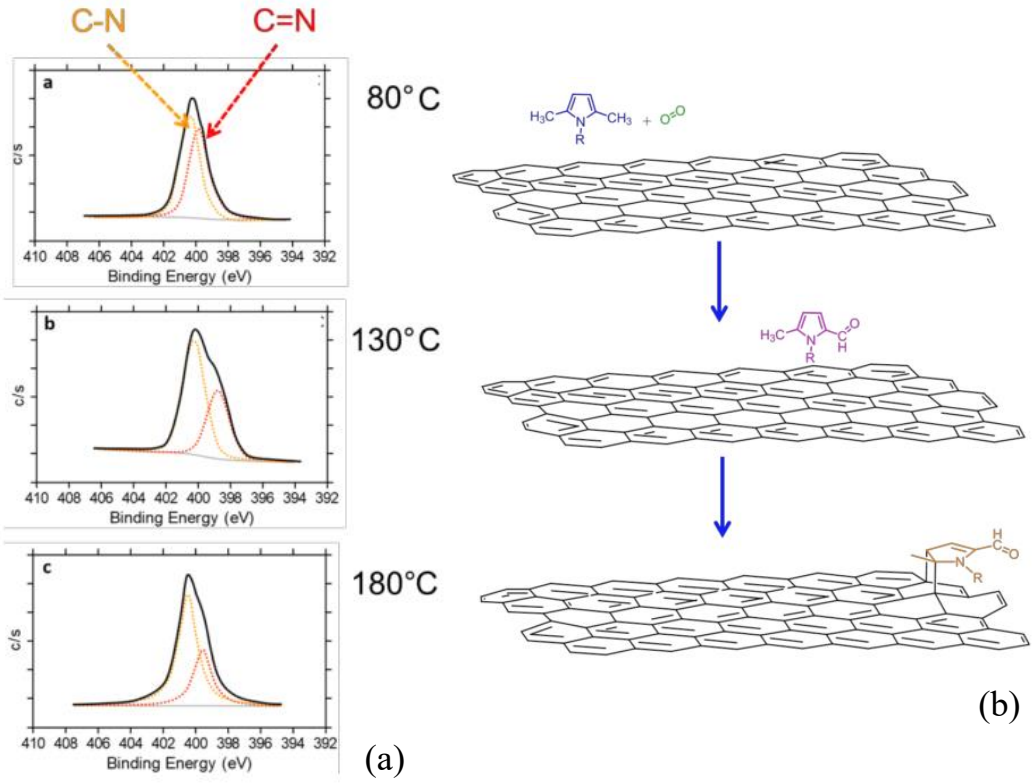


Figure 34. XPS spectra of N1s signal for HSAG-TMP mixture at different temperatures (a) and scheme of the DA grafting (b). Adapted from *"V. Barbera, L. Brambilla, A. Milani, A. Palazzolo, C. Castiglioni, A. Vitale, R. Bongiovanni, M. Galimberti, Domino reaction for the sustainable functionalization of few-layer graphene, Nanomaterials 9(1) (2018) 44".*

In general, the presented works show that the grafting characterization of small molecules on GRMs and graphites is possible but challenging: while appreciate the presence of deposited molecules on the substrates is trivial, assessing the actual covalent grafting on the substrate sites is more difficult.

**Nanocomposites with Graphene Related Materials**

One of the main limits of using GRMs as nanofillers in polymer nanocomposites is the frequent necessity to add functionalization steps [63], in order to improve the filler-matrix interaction at their interface, obtaining superior mechanical properties (as stiffness and tensile strength) and better dispersibility in the matrix. DA reversible crosslinking open to a direct covalent linking on GRMs without the need of previous functionalization steps on the filler, with the addition benefits of reversibility.

In 2019, Oh *et al.* realized nanocomposites with a polyurethane [64] or epoxy [65] modified matrix, with the aim of grafting the furan diene groups of the polymer to the surface of GNPs. The results are similar for both the matrices, so the case of modified polyurethane is presented as an example. The scheme of the prepared nanocomposite is showed in Figure 35.

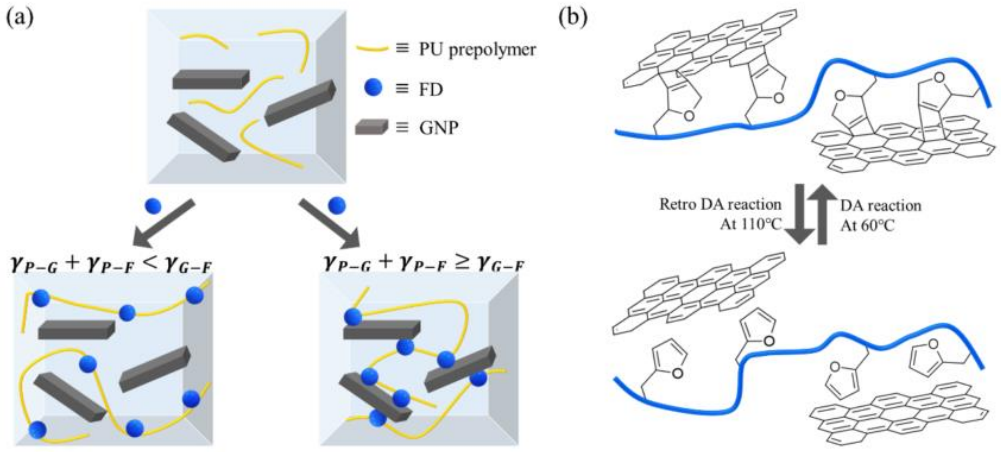


Figure 35. Scheme of the nanocomposite (a) with DA grafting on the filler (b). Reprinted from *"C.R. Oh, S.H. Lee, J.H. Park, D.S. Lee, Thermally self-healing graphene-nanoplate/polyurethane nanocomposites via Diels-Alder reaction through a one-shot process, Nanomaterials 9(3) (2019) 434"*.

The furan groups are part of a chain extender (FD in Figure 35 (a)) which react via condensation with the polyurethane prepolymer and via DA reaction with GNPs (Figure 35 (b)). The process is briefly summarized as follow: firstly, GNP is dispersed in a polyol, then a diisocyanate is added to the suspension to prepare the prepolymer with a thermal treatment at 60°C. Finally, chain extender FD with furan group, or alternatively a chain extender without furan group (as reference) is added and the mixture is left for 3 days at 70°C to perform the reactions. Firstly, the authors characterized GNP reacted with FD via Raman spectroscopy, reporting a remarkable growth of $I_D/I_G$, compared to GNP spectrum, related to grafting achievement. Moving to the prepared nanocomposites, FT-IR spectroscopy and Field Emission - Scanning Electron Microscopy (FE-SEM) measures are reported. In Figure 36 the FT-IR spectrum of the chain extender with furan group and the spectra of the nanocomposite containing FD with 0.1 wt% content of GNP, subjected to progressive heating, are shown. A peak at 1339 $cm^{-1}$ was assigned by the authors to divinyl alkyl ether =C-O-C=; the absence of the signal in the nanocomposite at room temperature (RT) is consistent with the presence of a DA adduct (see scheme in Figure 35 (b)). Indeed, this signal assigned to divinyl alkyl ether, present in FD, seems to appear and increase progressively with temperature

in the nanocomposite. This is consistent with the occurring of retro-DA reaction between 120°C and 150°C.

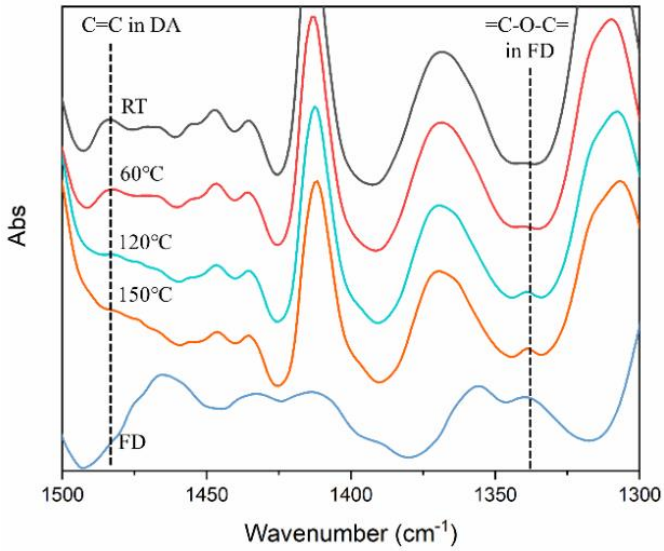


Figure 36. FT-IR spectra of FD and of polyurethane nanocomposite with 0.1 wt% content of GNP, subjected to progressive heating. Reprinted from *"C.R. Oh, S.H. Lee, J.H. Park, D.S. Lee, Thermally self-healing graphene-nanoplate/polyurethane nanocomposites via Diels-Alder reaction through a one-shot process, Nanomaterials 9(3) (2019) 434".*

FE-SEM images of 0.1_CPU and 0.1_DPU are reported in Figure 37. The authors commented these images underlining the differences between the coverage of GNP *lamellae* in the two nanocomposites: in the control sample (0.1_CPU), GNP are clearly visible, while in the nanocomposite with the supposed DA adduct (0.1_DPU), GNP appears less defined, probably being covered by a polymer layer. The authors associated this improved coating of *lamellae* to the achievement of the reaction between the polymer and the particles.

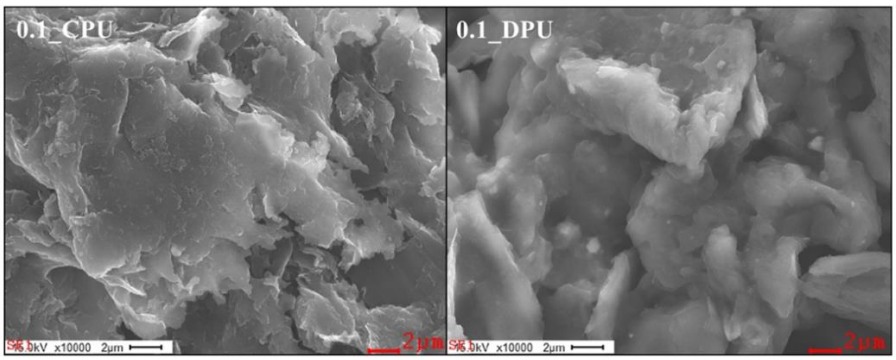


Figure 37. FE-SEM micrographs of 0.1_CPU and 0.1_DPU. Reprinted from *"C.R. Oh, S.H. Lee, J.H. Park, D.S. Lee, Thermally self-healing graphene-nanoplate/polyurethane nanocomposites via Diels-Alder reaction through a one-shot process, Nanomaterials 9(3) (2019) 434".*

Finally, in Figure 38 (a) stress-strain curves from tensile tests on DPU composites are shown: an increase in stiffness and tensile strength is reported, claimed by the authors as an effect of DA crosslinking of the polymer on GNP, although this affirmation appears weak without a proper comparing with CPU composites, since the reinforcement effect is also consistent simply with filler addition in a composite, without necessarily a covalent crosslinking at the matrix-filler interface.

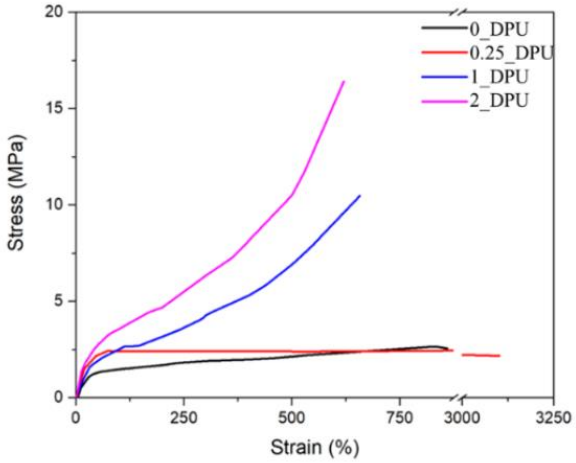


Figure 38. Stress–strain curves of the DPU with various GNP contents. Reprinted from *"C.R. Oh, S.H. Lee, J.H. Park, D.S. Lee, Thermally self-healing graphene-nanoplate/polyurethane nanocomposites via Diels-Alder reaction through a one-shot process, Nanomaterials 9(3) (2019) 434"*.

In 2019 Ramesh *et al.* [66] reported the preparation of a nanocomposite with DA functionalization on reduced Graphene Oxide (rGO), via furan groups grafted to a polystyrene maleic anhydride alternated copolymer (PSMF, scheme in Figure 39). The authors claimed successful DA grafting onto rGO via sonication in water, followed by drying at 40°C, as supported by the characterization reported below.

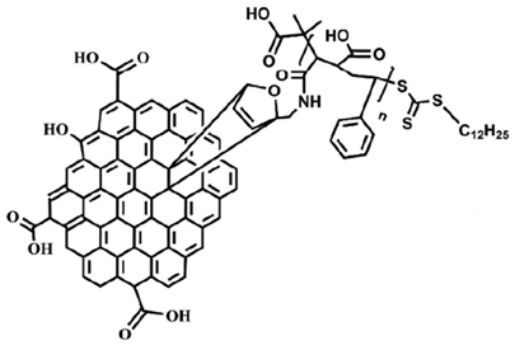


Figure 39. DA reaction scheme for poly(styrene-alt-maleic anhydride) grafted with furan groups on rGO. Adapted from *"K. Ramesh, D.S.B. Anugrah, A.K. Mishra, B.-H. Ahn, Y.-S. Gal, K.T. Lim, Green and sono synthetic approach for direct-functionalization of*

*reduced graphene oxide with poly(styrene-alt-maleic anhydride) by Diels Alder "click" reaction, Applied Surface Science 504 (2020) 144482*", with permission from Elsevier.

In Figure 40 Raman spectra for rGO, rGO nanocomposite of PSMF (rGO-PSMF), retro-rGO-PSMF (rGO-PSMF subjected to 150°C thermal treatment) and rGO/PSMF blend (rGO and PSMF only grinded and mixed together) are reported. It is clear that the $I_D/I_G$ ratio, related to the increase of defects on graphene and also to the presence of hybridized $sp^3$ carbons on the basal plane [57], is similar for rGO (1.10), retro-rGO-PSMF (1.11) and for rGO/PSMF blend (1.09). Instead, $I_D/I_G$ ratio is higher for rGO-PSMF (1.34). Besides, XPS and FT-IR characterization brings further support to the grafting achievement.

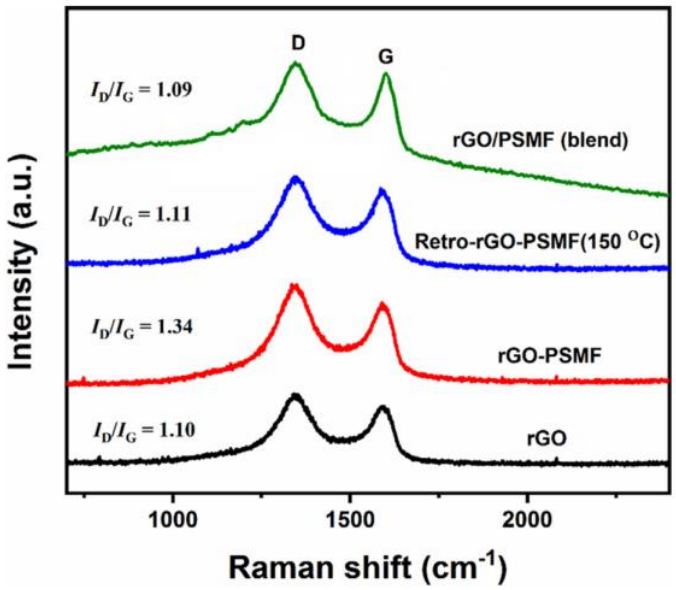


Figure 40. Raman spectra of rGO, rGO-PSMF, retro-rGO-PSMF and rGO/PSMF blend. Reprinted from *"K. Ramesh, D.S.B. Anugrah, A.K. Mishra, B.-H. Ahn, Y.-S. Gal, K.T. Lim, Green and sono synthetic approach for direct-functionalization of reduced graphene oxide with poly(styrene-alt-maleic anhydride) by Diels Alder "click" reaction, Applied Surface Science 504 (2020) 144482*", with permission from Elsevier.

**Composites with silica**

Dissociative CANs approach has been exploited in composites with silica in a few papers. Direct DA grafting on fillers surface as in the case of carbon fillers is not possible with silica, so previous functionalization on silica particles is mandatory to obtain a matrix-filler covalent grafting. Imai *et al.* [67] realized an interpenetrating polymer network combining a sol-gel process with DA thermoreversible reaction, generating an hybrid organic-inorganic network. Jia *et al.* [68] and Schäfer *et al.* [69] realized two dissociative CANs composites based

on DA reaction on previously functionalized silica particles, with an ethylene-propylene rubber and poly(butyl methacrylate), respectively, performing the preparations in solvent.

Jia *et al.* [68] prepared a dissociative CAN composite based on silica, grafting furan groups on an ethylene-propylene rubber, then mixing it with different contents of previously diene-functionalized silica (the used diene was 3-(methacryloyloxy)propyltrimethoxysilane). The process (performed in solvent) is outlined in Figure 41. The authors were able to obtain crosslinked and reprocessable composites, with enhanced stiffness and tensile strength, related to the content of functionalized silica (tensile strength from 2 to 6 MPa increasing silica content from 15 to 45 phr) as shown in Figure 42 (a) and (b). Besides, tensile test results are stable after reprocessing the composites two times (Figure 42 (c) and (d)).

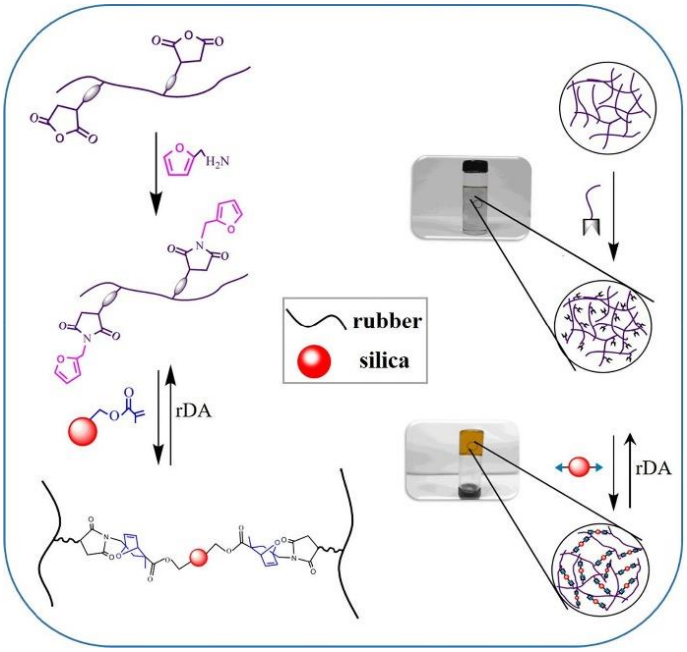


Figure 41. Scheme of silica CAN composite preparation. Reprinted from *"Z. Jia, S. Zhu, Y. Chen, W. Zhang, B. Zhong, D. Jia, Recyclable and self-healing rubber composites based on thermorevesible dynamic covalent bonding, Composites Part A: Applied Science and Manufacturing 129 (2020) 105709"*, with permission from Elsevier.

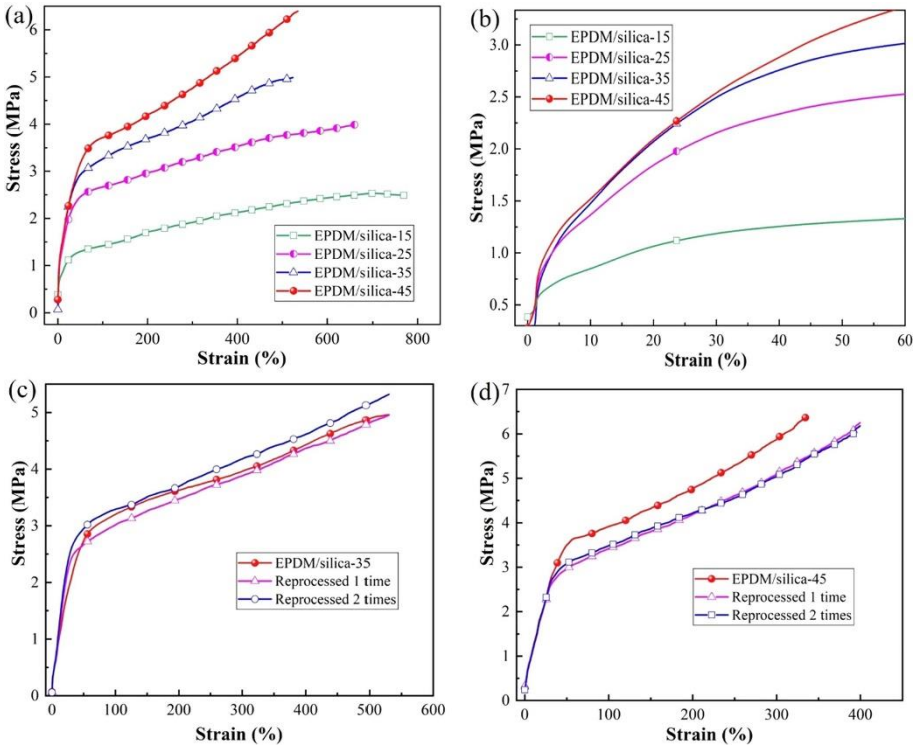


Figure 42. Stress-strain curves of the composites (a); enlarged stress-strain curves in the strain range from 0 to 60%; stress-strain curves of reprocessed composites with 35 phr (c) and 45 phr (d) modified silica. Reprinted from *"Z. Jia, S. Zhu, Y. Chen, W. Zhang, B. Zhong, D. Jia, Recyclable and self-healing rubber composites based on thermorevesible dynamic covalent bonding, Composites Part A: Applied Science and Manufacturing 129 (2020) 105709"*, with permission from Elsevier.

Overall, dissociative CANs silica composite potential and especially the use of silica nanoparticles have not been explored widely in literature yet.

## 1.3. Purposes of this work

Relying on the presented state of the art, in this work a range of dissociative CANs based on DA thermoreversible reaction were prepared, mainly via melt processing and using solvents only for pre-processing steps when needed. CANs approach represents a new way to overcome the traditional limits of thermoset and thermoplastic polymers, exploiting the advantages of a crosslinked network in terms of mechanical performances and chemical stability but with the industrial and environmental advantages of melt processing and recyclability. In the field of CANs, a dissociative approach was chosen, as the best approach for melt processing in author's opinion after literature investigation. In fact, a dissociative CAN approach, compared to an associative one, has the benefit of being independent on

the kinetic issues of an exchange reaction-based rearrangement, striking a balance between the stability at room temperature (without undesired creep under stress) and the reprocessability at high temperature. Furthermore, an associative approach often requires the presence of a catalyst, in order to regulate the exchange kinetic reaction. On the other hand, a dissociative approach in principle offers the advantages of an "On-Off" (or "Open-Close") switching network, mainly sacrificing only solvent resistance in temperature. Among dissociative CANs, DA reaction was chosen as the most suitable in terms of stability and reversibility, based on the described state of the art. Different polymer systems were selected and explored for the preparation of thermoreversible crosslinked system, including both high glass transition ($T_g$) polymers such as styrene maleic anhydride copolymer and low $T_g$ polymers such as polyethylene grafted with maleic anhydride and ethylene-propylene rubber grafted with maleic anhydride.

Reversible crosslinking potential was explored also in nanocomposites. The ethylene-propylene rubber was selected as the most suitable polymer to prepare nanocomposites, relying on the results of polymer thermoreversible crosslinking. Besides, most of applications where rubbers are exploited require the addition of fillers, to comply with the required mechanical and thermal properties [70]. The nanofillers exploited to prepare a thermoreversible nanocomposites were carbon and silica nanoparticles, two of the main class of fillers used in rubber industry. Regarding carbon nanoparticles, lamellar fillers, as GNP and rGO, were chosen for their greater industrial viability (compared for example to carbon nanotubes). The nanometric size was chosen for the well-known advantages in terms of specific area, keeping the filling content lower and obtaining similar mechanical performances than using higher contents of non-nanometric fillers. Furthermore, as discussed in the state of the art, one of the main drawbacks of GRMs in composite (*i.e.* the poor matrix-filler interface interaction), which often requires previous functionalization of the nanofillers, can be addressed with a dissociative reversible crosslinking approach via DA reaction. In fact, exploiting the already known DA reaction on GRMs in a melt processed nanocomposite with a stronger matrix-interface interaction paves the way to an industrially viable process for materials with potentially superior filler dispersion and mechanical properties. The DA grafting on $sp^2$ hybridized particles, discussed in the state of the art, was assessed exploiting a model reaction of a small dienophile (MA) on GNP. The grafting was performed both with a method already used in literature and also developing a novel vapor approach which does not include the use of solvents. Relying on the results observed in the model reaction, among lamellar nanofillers, rGO was selected for

the functionalized polymer reinforcement, then a range of nanocomposites was prepared via melt blending and consequently characterized. In addition, an alternative processing option (Press&Fold method) was explored, in order to overcome specific issues in maximum filler amount. Regarding silica nanocomposites, with the aim of increasing the matrix-filler interaction strength and consequently the mechanical strength and stiffness of the materials, a pre-processing functionalization of silica nanoparticles was performed, grafting groups able to perform DA reaction with the polymer. Then a range of nanocomposites was prepared via melt blending and characterized generating a silica nanocomposites crosslinked by the nanofillers.

*Part of the work described in this doctoral dissertation has been previously published in:*

*"F. Cantamessa, G. Damonte, O. Monticelli, R. Arrigo, A. Fina, Thermoreversible cross-linked rubber prepared via melt blending and its nanocomposites, ACS Applied Polymer Materials 4(7) (2022) 4796-4807."*

*"F. Cantamessa, F. Carniato, A. Fina, Thermoreversibly crosslinked silica-rubber composite prepared via melt processing, Reactive and Functional Polymers 186 (2023) 105552."*

# Chapter 2

# Materials and methods

In this chapter, a description of the materials and methods used in this work is provided. Firstly, the materials used in the experimental work are listed and briefly described, providing the information and the properties that may be useful for the reader. Materials are organized in three macro-groups: polymers, fillers and others (additives, reagents and solvents). Then, a detailed list of the methods, of both experimental procedures and characterization, is provided, in order to accompany the reader through this work with a clear guide of materials preparation and analysis, to guarantee the understandability of the results (Chapter 3) and the repeatability of the experiments.

## 2.1. Materials

### 2.1.1. Polymers

Styrene Maleic Anhydride (SMA) is a commercial product (Xiran® EF80), kindly provided by Polyscope Polymers (Netherlands). It is a random copolymer with a MA content of about 10 wt% and a molecular weight of 10000 g/mol. Polyethylene grafted with Maleic Anhydride (PEgMA) is a commercial product (Compoline® CO/LL 05), kindly provided by AUSER Polimeri S.R.L. (Italy). It is a linear low-density polyethylene grafted with a low MA content (about 1 wt%). Ethylene-Propylene Rubber grafted with Maleic Anhydride (EPRgMA) is a commercial product (Keltan® 1519R), kindly provided by ARLANXEO Performance Elastomers (Netherlands). It is an amorphous ethylene-propylene

copolymer grafted with a low MA content (about 2 wt%) and a molecular weight of 110000 g/mol.

### 2.1.2. Nanoparticles

The Graphite NanoPlates (GNP) and the thermally reduced Graphene Oxide (rGO) are research grade materials, kindly provided by Avanzare Innovacion Tecnologica S.L. (Spain). Regarding GNP, preparation procedure was previously reported [71]; in brief, natural graphite flakes were intercalated with sulfuric acid and then expanded in a worm-like form with a rapid high temperature treatment (1000°C in nitrogen atmosphere), then milled in order to separate nanoflakes, obtaining GNP. These nanoflakes are tens of μm wide and a few nm thick, with a specific surface area by Brunauer-Emmett-Teller (BET) model of 39 $m^2/g$, defectiveness as $I_D/I_G$ ratio by Raman spectroscopy of 0.10 and oxygen content by XPS of 5 at% (full characterization has been described elsewhere [72]).

Regarding rGO, synthetic procedure was previously reported [73]; in brief, rGO was prepared by oxidation of natural graphite, tip-sonication in water solution and then thermal reduction at 1060°C in argon atmosphere. rGO nanoflakes are tens of μm wide and a few nm thick with a specific surface area by BET of 196 $m^2/g$, defectiveness as $I_D/I_G$ ratio by Raman of 1.35 and oxygen content by XPS of 2 at% (full characterization has been described elsewhere [72]).

Amorphous precipitated silica is a commercial product (HI-SIL® EZ 200G), kindly provided by PPG Silica Products (USA). It is presented as a powder made of aggregated particles of irregular form with an indicative diameter of 10-20 nm and specific surface area by BET of 300 $m^2/g$.

### 2.1.3. Additives, reagents and solvents

Furfurylamine (FFA, ≥99%), Maleic Anhydride (MA, ≥99%), acetone (≥99%), toluene (≥99%), Tetrahydrofuran (THF, ≥99%), Orthodichlorobenzene (ODCB, ≥99%), diethyl ether (≥99%) and Irganox® 1010 were purchased by Sigma-Aldrich (Germany). 2,2-Bis[4-(4-maleimidophenoxy)phenyl]propane (BM) was purchased by TCI chemicals (Belgium). Imide-extended bismaleimide (BM1) was purchased by ThermoFisher scientific (Germany). 1-[3-(Triethoxysilyl)propyl]-1H-pyrrole-2,5-dione was purchased from Molekula (Italy).

## 2.2. Methods

### 2.2.1. Diene-functionalization of polymers

**Styrene maleic anhydride**

Grafting of furan groups on the polymer chains was performed through the well-known reaction between anhydride and amine groups [74]. SMA was grafted with furan groups through reaction with FFA both in solvent media and via melt processing.

The reaction in solvent was previously reported [75]: in this work SMA was dissolved in THF (in a concentration of 0.1 g/ml), then FFA was added (in a 1:1 molar ratio with MA groups in SMA) under stirring. After that, solvent was removed by evaporation, under stirring of the solution in the fume hood. The obtained compound, referred to as SMAgF*, was manually chopped and annealed at 180°C and 75 mbar in vacuum oven for 15 minutes, to complete the reaction and remove the residual solvent. The compound obtained after annealing is referred to as SMAgF.

The furan grafting via melt processing was performed in a W50E internal mixer (Brabender, Germany). The mixer was set at 170°C and filled with SMA at 30 rpm screw rotation speed. After that, FFA was added in a 1:1 molar ratio with MA groups in SMA, directly into the molten polymer and mixed for 5 minutes at 60 rpm. The obtained compound is referred to as SMAgF (annealing was considered unnecessary due to the already high temperature of the process).

**Polyethylene grafted with maleic anhydride**

PEgMA was grafted with furan groups through reaction with FFA in the W50E internal mixer (Brabender, Germany). The mixer was set at 150°C and filled with PEgMA at 30 rpm screw rotation speed. After that, FFA was added in a 2:1 molar ratio with MA groups in PEgMA, directly into the molten polymer and mixed for 5 minutes at 60 rpm. Here the excess amine was designed, after the first tests on SMA, to compensate for it partial volatilization during melt blending. The obtained compound, referred to as PEgF*, was manually chopped and annealed at 180°C and 75 mbar in vacuum oven for 15 minutes, in order to complete the reaction and remove the excess FFA. The compound obtained after annealing is referred to as PEgF.

**Ethylene-propylene rubber grafted with maleic anhydride**

EPRgMA was grafted with furan groups through reaction with FFA in the W50E internal mixer (Brabender, Germany). The mixer was set at 150°C and filled with EPRgMA at 30 rpm screw rotation speed, together with an antioxidant (Irganox® 1010), in the amount of 0.1 wt% of EPRgMA. After that, FFA was added in a 2:1 molar ratio with MA groups in EPRgMA, directly into the molten rubber and mixed for 5 minutes at 60 rpm. The obtained compound, referred to as EPRgF*, was manually chopped and annealed at 180°C and 75 mbar in vacuum oven for 15 minutes, in order to complete the reaction and remove the excess FFA. The compound obtained after annealing is referred to as EPRgF.

## 2.2.2. Thermoreversible crosslinking with bifunctional dienophile

**Styrene maleic anhydride grafted with furan**

SMAgF (obtained by melt processing) was blended with BM (26 wt%) in the W50E internal mixer (Brabender, Germany) for 5 minutes at 170°C and 60 rpm. The ratio between furan and maleimide functions, assuming all the anhydride sites of EPRgMA were previously reacted with FFA, was stoichiometric. The obtained product is referred to as SMAgF-26%BM. To insure completion of crosslinking, the product was subjected to annealing in oven, for three days at 50°C, according to [34].

**Polyethylene grafted with furan**

PEgF was blended with BM1 (13 wt%) in a co-rotating twin screw micro-extruder (DSM Xplore 15, Netherlands) for 5 minutes at 150°C and 100 rpm. The molar ratio between furan and maleimide functions, assuming all the anhydride sites of PEgMA were previously reacted with FFA, was stoichiometric. The obtained product is referred to as PEgF-13%BM1. To insure completion of crosslinking, it was subjected to annealing in oven, for three days at 50°C.

**Ethylene-propylene rubber grafted with furan**

EPRgF was blended with BM in different ratios in the co-rotating twin screw micro-extruder (DSM Xplore 15, Netherlands) for 5 minutes at 150°C and 100 rpm. Table 1 reports the compositions of the blends developed for different molar ratios between furan and maleimide functions, assuming all the anhydride sites of

EPRgMA were previously reacted with FFA. After blending, the compound was extruded from the chamber and collected.

Table 1. Compositions of EPRgF-BM blends.

| | Furan : maleimide molar ratio | BM content (wt%) |
|---|---|---|
| EPRgF-2.7%BM | 1 : 0.5 | 2.7 |
| EPRgF-5.4%BM | 1 : 1 | 5.4 |
| EPRgF-8.1%BM | 1 : 1.5 | 8.1 |

For characterization, the different compounds were hot-pressed at 150°C for 4 minutes to produce films of the required shape and thickness. To insure completion of crosslinking, all the materials were subjected to annealing in oven, for three days at 50°C, according with a previously reported procedure [34].

## 2.2.3. Nanocomposites embedding graphene related materials

### Model reaction of maleic anhydride on graphite nanoplates

MA was deposited on GNP both via a solvent method, already validated in literature [50], and by a new solvent deposition method developed during this work.

Regarding the solvent method, 50 mg of GNP were ultrasonicated in 100 ml of ODCB via tip-sonication at 150 W and 20 KHz (Sonics, Vibra-cel-VCX-500, 13 mm tip, USA) for 30 minutes, through steps of 5 seconds ON and 5 seconds OFF. This process was repeated 4 times with 30 minutes of resting between sets, to avoid overheating, with a total of 2 hours of ultrasonication. After that, 500 mg of MA were dissolved in the suspension (GNP:MA weight ratio = 1:10) and it was kept at 120°C for 3 hours under magnetic stirring, under reflux, according with a previously reported procedure [50]. Finally, the product was filtered through a 0.1 μm PTFE membrane, then washed with ethanol and acetone and dried overnight in vacuum (75 mbar) at room temperature. The obtained product is referred to as GNP-MA_sol.

A vapor phase MA deposition method was developed (scheme in Figure 43) as an alternative to the described solvent method: 200 mg of GNP were put in a filter paper cone, sustained by a metal support inside a vial, together with 1 g of MA (GNP:MA weight ratio = 1:5) on the bottom of the vial. Then the system was

filled with nitrogen, closed, sealed and left at 120°C for 3 hours in oven. Then the product in the filter cone, referred to as GNP-MA_vap, was removed and analysed without washing steps.

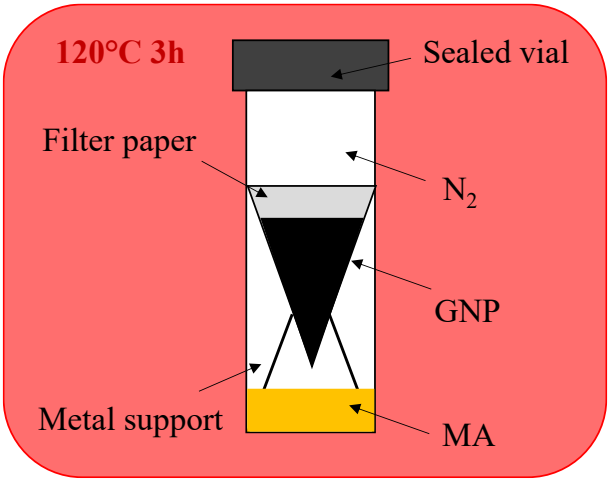


Figure 43. Scheme of the vapor deposition process.

**Nanocomposites blending**

EPRgF-5.4%BM and rGO were selected to prepare nanocomposites, with compositions reported in Table 2.

Table 2. Compositions of EPRgF-BM/rGO nanocomposites.

| | EPRgF content (wt%) | BM content (wt%) | rGO content (wt%) |
|---|---|---|---|
| EPRgF-5.4%BM/5%rGO | 89.9 | 5.1 | 5.0 |
| EPRgF-5.4%BM/10%rGO | 85.1 | 4.9 | 10.0 |

The necessary amount of rGO (0.6 or 1.2 g) was ultrasonicated in 150 ml of acetone via tip-sonication at 150 W and 20 KHz (Sonics, Vibra-cel-VCX-500, 13 mm tip, USA) for 30 minutes, through steps of 5 seconds ON and 5 seconds OFF, with beaker immersed in water/ice bath, to avoid overheating. Then, the requested amount of BM was dissolved in the suspension and the solvent was evaporated at room temperature in fume hood overnight, under magnetic stirring. The obtained mixtures of rGO and BM were finally melt blended with EPRgF with the same conditions used for EPRgF-BM products, namely 5 minutes of mixing at 150°C at 100 rpm, and then extruded. In the case of 10 wt% rGO, where the high viscosity

led to blockage of the extruder after approx. 2 min, extruding was not possible, requiring manual recovery of the composite from the mixing chamber. The nanocomposites were hot-pressed at 150°C for 4 minutes to produce specimens for characterization and annealed in oven at 50°C for 3 days.

**Press&Fold method**

Press&Fold (P&F) method [76] is an alternative processing procedure developed with the aim of increasing the filler content in nanocomposites, without encountering the typical high-viscosity problems of classic processing methods like extrusion. P&F method involves multiple hot-pressing steps, starting from a sandwich made of two polymer films and the filler between. After the first hot-pressing step, the obtained film is folded and hot-pressed again. This procedure is repeated until a satisfying degree of filler dispersion is reached (the reported work [76] with LLDPE and GNP point to a number of hot-pressing cycles > 100). Figure 44 reports the scheme of P&F procedure.

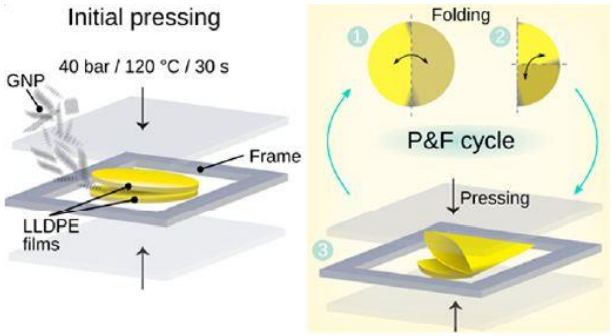


Figure 44. Scheme of Press&Fold (P&F) procedure. Reprinted from "G. *Santagiuliana, O.T. Picot, M. Crespo, H. Porwal, H. Zhang, Y. Li, L. Rubini, S. Colonna, A. Fina, E. Barbieri, A.B. Spoelstra, G. Mirabello, J.P. Patterson, L. Botto, N.M. Pugno, T. Peijs, E. Bilotti, Breaking the nanoparticle loading-dispersion dichotomy in polymer nanocomposites with the art of croissant-making, ACS nano 12(9) (2018) 9040-9050*". Copyright 2018 American Chemical Society.

In this work, P&F method was used to prepare EPRgF-BM/rGO nanocomposites as an attempt to rise rGO content higher than 10 wt%. A mixture of rGO and BM was prepared as described in the previous subsection (ultrasonication of rGO, BM dissolution, solvent removal), and added between a sandwich of hot-pressed EPRgF films (250 μm thick). After the initial pressing, the film was folded twice (Figure 44) and hot-pressed at 150°C for 15 seconds (the pressing time was kept low to minimize the total time at high temperature, related to possible degradation phenomena). This procedure was repeated several times (number of cycles) on different samples. The first nanocomposite prepared had the

composition of EPRgF-5.4%BM/10%rGO (Table 2), in order to compare it with the nanocomposite prepared via melt blending. Besides, samples of EPRgF-5.4%BM and EPRgF were prepared via P&F as reference, starting from a sandwich of two EPRgF-5.4%BM and two EPRgF films (prepared by melt processing and hot-pressing), respectively, to study the effect of P&F cycles on the matrix.

## 2.2.4. Silica nanocomposites

### Silica functionalization with dienophile groups

Silica functionalization was carried out by Prof. Fabio Carniato at the University of Eastern Piedmont and provided for the use in this PhD work. Functionalization procedure is summarized here. 1.0 g of amorphous precipitated silica (Sil) was treated in vacuum at 250°C for 3 h in order to remove physisorbed water and activate the silanol groups exposed on the surface. After this treatment, the powder was dispersed in 100 ml of toluene and stirred for 15 minutes under nitrogen flow. In parallel, a toluene solution containing 500 mg of 1-[3-(Triethoxysilyl)propyl]-1H-pyrrole-2,5-dione in 50 ml of solvent was prepared. The solution was then added to the silica suspension and the new mixture was stirred at room temperature for 18 h. Finally, the powder (Sil-M) was isolated by filtration and washed several times with diethyl ether in order to remove the unreacted silane.

### Nanocomposite blending

EPRgF was blended with Sil, Sil-M and BM in different ratios in a corotating twin screw micro-extruder (DSM Xplore 15, Netherlands) for 5 min at 150 °C and 100 rpm. Amount of Sil-M added to the compounds was calculated, taking into account of the organic functionalization (i.e. 30 wt% see chapter Results), to obtain the same content of inorganic compared to pristine Sil. Composition of the prepared compounds are reported in

Table 3. Both silicas were previously dried overnight at low temperature in vacuum oven (40°C, 75 mbar); higher temperatures were avoided in order to protect the integrity of the reactive maleimide groups of Sil-M. For characterization, the different compounds were hot pressed at 150 °C for 4 min to produce films of the required shape and thickness. To ensure completion of crosslinking, all the materials were subjected to annealing in oven for 3 days at 50 °C, according to a previously reported procedure [34].

Table 3. Compositions of Sil and Sil-M composites.

| | EPRgF content (wt%) | Sil content (wt%) | Sil-M content (wt%) | BM content (wt%) |
|---|---|---|---|---|
| EPRgF/7%Sil | 93 | 7 | 0 | 0 |
| EPRgF/10%Sil-M | 90 | 0 | 10 | 0 |
| EPRgF/14%Sil | 86 | 14 | 0 | 0 |
| EPRgF/20%Sil-M | 80 | 0 | 20 | 0 |
| EPRgF-2.7%BM/7%Sil | 90.5 | 7 | 0 | 2.5 |
| EPRgF-2.7%BM/10%Sil-M | 87.6 | 0 | 10 | 2.4 |

## 2.2.5. Characterization

Attenuated Total Reflection Fourier Transformed Infrared (ATR FT-IR) and transmission FT-IR spectroscopy measures were performed using a Frontier spectrometer (Perkin-Elmer, USA), running 16 scans with a resolution of 4 $cm^{-1}$, on the surface of chopped samples and on thin hot-pressed films (50 μm thick), respectively. Transmission FT-IR spectra of Sil and Sil-M have been collected at room temperature under vacuum conditions without dilution in KBr matrix, in the range 4000–400 $cm^{-1}$, with a spectral resolution of 4 $cm^{-1}$, by using the an Equinox 55 spectrometer (Bruker, USA). Baselines of the spectra were calculated using a spline function and removed. Spectra were then normalized when required.

CHN elemental analysis were realized by the EA3000 CHN Elemental Analyser (EuroVector, Italy). Acetanilide was used as the calibration molecular standard (C% = 71.089, H% = 6.711, N% = 10.363).

Raman spectroscopy measures were performed using an inVia Reflex Raman microscope (Renishaw PLC, UK), equipped with an excitation argon laser source (514.5 nm of wavelength). The reported spectra are the average of five measurements acquired in different areas of the same sample.

X-ray Photoelectron Spectroscopy (XPS) measures were recorded on a VersaProbe5000 X-ray photoelectron spectrometer (Physical Electronics Inc.,

USA), equipped with a monochromatic Al K-alpha X-ray source. High resolution spectra were acquired with a 100 μm spot size (24.7 W, 23.5 eV). The deconvolution of XPS high resolution peaks was performed with a Voigt function (Lorentzian/Gaussian = 20/80) after a Shirley subtraction of the background. The C1s region (294-281 eV) shows a strong asymmetric signal, with maximum at about 284.4 eV and a long tail towards higher binding energies, related to the overlapping of several peaks. Relying on previous work assignments [71], after deconvolution the several contributes were assigned in this way: the main signal at 284.4 eV was assigned to $sp^2$ C=C carbon, a second signal at 284.9 eV was assigned to $sp^3$ C-C carbon, a third signal at 285.8 eV was assigned to $sp^3$ carbon (C-O group), a fourth signal at 288.4 eV was assigned to $sp^2$ carbon (C=O group) and a last signal at 290.8 eV was assigned to π-π interactions. It is worth to report that the main signal at 284.4 eV, assigned to $sp^2$ C=C carbon, is intrinsically asymmetric, with a tail towards higher binding energies [77]; this must not be confused with the presence of other signals and need to be considered in the deconvolution process. Signal assignments are summarized in Table 4.

Table 4. XPS signal assignments in C1s region after deconvolution. The shift is referred to the main signal position (284.4 eV).

| **Binding energy** [eV] | **Shift** [eV] | **Assignment** |
|---|---|---|
| 284.4 | 0 | $sp^2$ C=C carbon |
| 284.9 | + 0.5 | $sp^3$ C-C carbon |
| 285.8 | + 1.4 | $sp^3$ carbon (C-O group) |
| 288.4 | + 4 | $sp^2$ carbon (C=O group) |
| 290.8 | + 6.4 | π-π interaction |

The morphology of the samples was studied by Scanning Electron Microscopy (SEM) using an EVO 15 SEM (Zeiss, Germany) with a beam voltage of 20 kV. The micrographs were taken from the fragile fracture surfaces obtained after soaking the samples in liquid nitrogen for 2 minutes for soft polymers.

Differential Scanning Calorimetry (DSC) tests were performed with a Q20 DSC (TA Instruments, USA) on samples of ca. 8 mg in closed aluminium pans with perforated lids. The measurements were performed under dry $N_2$ gas, running a

heating ramp from 0 to 200 °C, then a cooling ramp to 0°C and another heating ramp up to 200°C. Both heating and cooling ramp were performed at 10°C/min rate.

Thermogravimetric Analysis (TGA) tests were performed with a Discovery TGA (TA Instruments, USA) on samples of ca. 8 mg. The measurements were performed under dry $N_2$ gas, running a heating ramp from 50 to 500 °C at 10°C/min rate.

Dynamic Mechanical Thermal Analysis (DMTA) measurements were performed using a Q800 DMTA (TA Instruments, USA) equipped with tension film clamps. 8x16 $mm^2$ specimens were cut from hot-pressed 1 mm thick sheets. Tests were carried out at constant frequency (1 Hz), controlled strain (0.1%) and with a temperature ramp from -80 to 160°C at 3°C/min rate. The pre-load was set at 0.01 N.

Rheology tests were performed using an ARES rheometer (TA Instruments, USA) on hot-pressed round specimens of 26 mm of diameter and 1 mm thick. Frequency sweep measurements were carried out from 100 to 0.1 rad/s with fixed temperature (150°C) and strain (1%), after ensuring to work in viscoelastic field by strain sweep tests. Stability measurements were carried out for 1 h at fixed temperature (150°C), strain (1%) and frequency (1 rad/s). Temperature ramp measurements were carried out performing a ramp from 100 to 200°C at 3°C/min, with fixed strain (1%) and frequency (1 rad/s).

Thermal conductivity tests were performed through Transient Plate Source (TPS) method with a 2500S TPS (Hot Disk AB, Sweden), equipped with a Kapton sensor with a radius of 3.189 mm. Measurements were carried out using a bulk method and an impulse of 50 mW for 4 seconds. Three measurements were taken for each specimen and the mean value was calculated. The tests were performed keeping the samples at a temperature of 23°C, which was controlled by a silicon oil bath.

Tensile tests were performed using a 5966 dynamometer (Instron, USA). The instrument was equipped with a load cell of 50 N and the pneumatic clamps were fitted with 25x25$mm^2$ flat faces. The materials were prepared by hot-pressing films with a thickness of 250 μm thick and then cut in specimens 20 mm wide and about 100 mm long. The initial distance between the clamps was set at 50 mm. Regarding PE samples, the pre-load was set at 0.4 N and the tests were carried out at 1 mm/min up to a strain of 0.3%, then at 30 mm/min until specimens broke. Regarding softer

rubber EPR samples, the pre-load was set at 0.02 N and the tests were carried out at 1 mm/min up to a strain of 0.3%, then at 10 mm/min until specimens broke. Young's modulus (E) was calculated between 0 and 0.1% of strain. The ultimate tensile strength, referred to as tensile strength for brevity is $\sigma_{max}$ and the elongation at break is $\varepsilon_b$. Three specimens were tested for each material and the results averaged.

The evolution of mechanical properties upon recycling was studied reprocessing the films by compression molding (15 s at 150°C), then annealing them in oven (3 days at 50°C) to obtain specimens for tensile testing, according to the method described above.

Crosslinking degree was calculated after solubilisation tests. About 60 mg of each sample was left in vacuum oven at 75mbar overnight, then weighed and soaked overnight in 20 ml of toluene. After that, the remaining solid part was extracted and dried under the hood. Finally, the sample was left again overnight in vacuum oven at 75 mbar and then weighed to calculate the percentage of the initial weight, to determine the insoluble fraction. The error of the measurement was estimated in the range of 3 wt%. Crosslinking reversibility was investigated by solubilisation test, soaking 250 mg of sample in 50 ml of boiling toluene (ca. 110°C) for 3 hours. Composite samples were subtracted by the filler (rGO, Sil or Sil-M) contribute to weight, considering only the rubber matrix part. The calculation of crosslinking degree is Equation 1.

Equation 1
$$Crosslinking\ degree\ (wt\%) = \frac{M_a - M_{filler}}{M_b - M_{filler}} \cdot 100$$

Where $M_b$ and $M_a$ are the mass before and after overnight soaking and drying, respectively, and $M_{filler}$ the mass off filler (rGO, Sil or Sil-M) contained in the sample.

# Chapter 3

# Results discussion

In this chapter, the experimental results of this work are presented and discussed. on the preparation and characterization of thermoreversible networks is first reported, with the maleated polymers (SMA, PEgMA and EPRgMA) functionalization with diene moieties, resulting in SMAgF, PEgF and EPRgF, and their thermoreversible crosslinking via melt blending with bifunctional dienophile molecules (BM or BM1) via DA reaction. After that, the preparation of nanocomposites is presented, starting from carbon nanoparticles with a model reaction of DA reaction between MA and GNP and the melt blending of a rGO thermoreversible nanocomposite with a EPRgF-BM matrix, continuing then with the preparation of a silica nanocomposite, thermoreversibly crosslinked on a dienophile-functionalized silica (Sil-M).

## 3.1. Thermoreversible networks

### 3.1.1. Diene-functionalization of polymers

#### Styrene maleic anhydride

Figure 45 describes the grafting reaction scheme of dienes (furan groups) on SMA, starting from the reaction of SMA with FFA, through an amide intermediate and eventually to the furfuryl imide derivative (SMAgF).

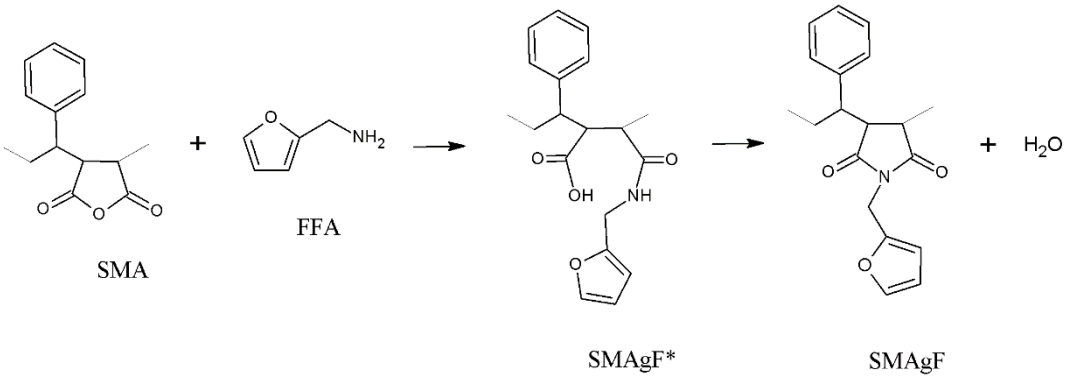


Figure 45. Scheme of the furan functionalization of SMA.

Furan grafting on SMA was investigated by ATR FT-IR spectroscopy. In Figure 46 FT-IR spectra of FFA, SMA, SMAgF* and SMAgF are reported for the solvent preparations (THF) and melt blending processing, while assignments are listed in Table 5.

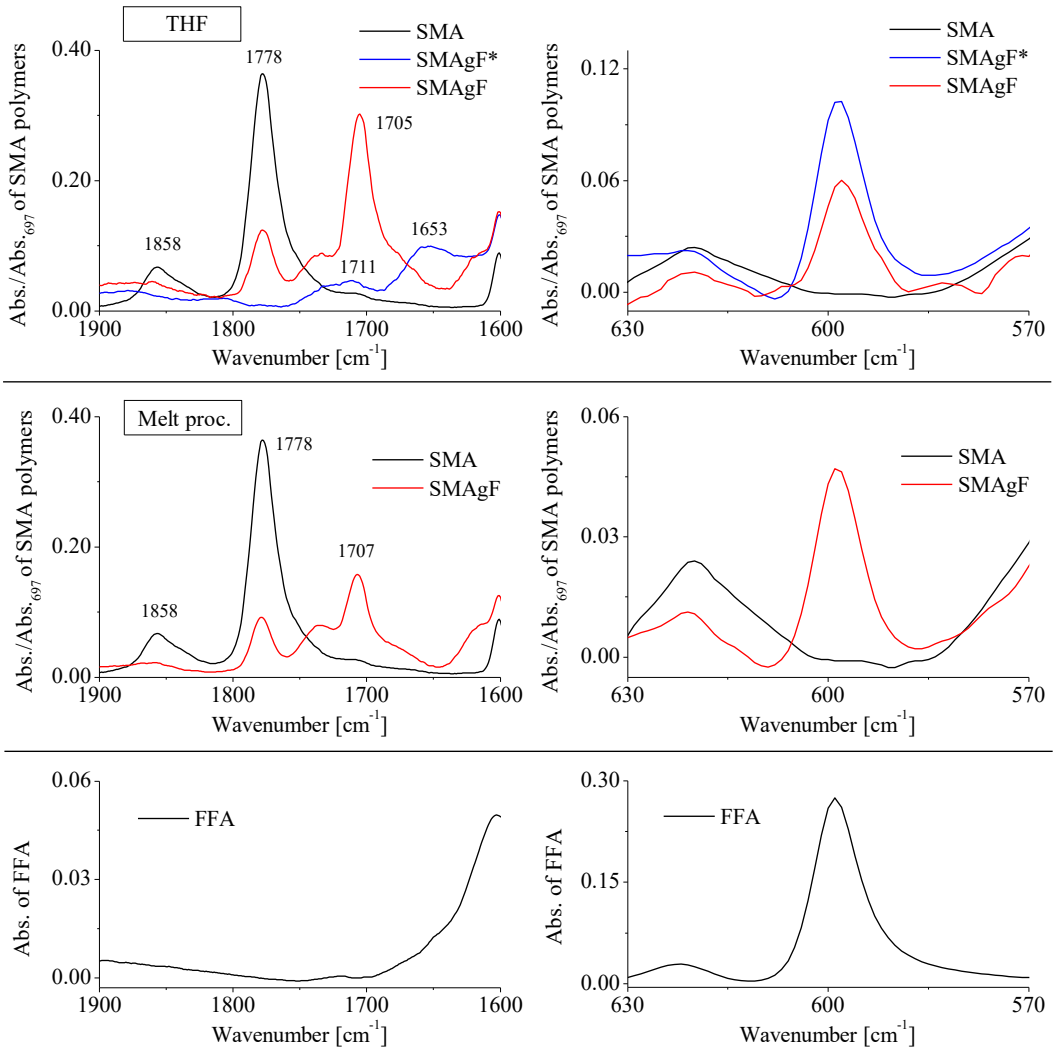


Figure 46. ATR FT-IR spectra relating to SMA functionalization with FFA in the range 1900-1600 $cm^{-1}$ and 630-570 $cm^{-1}$ for THF preparation (up) and melt processing (middle) (SMA spectra are normalized on their higher peak at 697 $cm^{-1}$, assigned to monosubstituted benzene ring out-of-plane deformation vibration [78], while FFA spectrum is not normalized).

Table 5. Assignments of FT-IR spectra for SMA, PEgMA and EPRgMA diene functionalization.

| **Wavenumber** [$cm^{-1}$] | **Assignment** |
|---|---|
| *1866-1858* | C=O asymmetric stretching of anhydride |
| *1791-1778* | C=O symmetric stretching of anhydride |

| | |
|---|---|
| *1778-1776* | C=O symmetric stretching of imide |
| *1712-1705* | C=O stretching of carboxylic acid |
| *1715-1705* | C=O asymmetric stretching of imide |
| *1660-1650* | C=O stretching of secondary amide |
| *599* | Furan ring deformation |

Regarding THF preparation, in the 1900-1600 $cm^{-1}$ range pristine SMA spectrum shows two absorption bands centered at 1858 and 1778 $cm^{-1}$, that are typical of cyclic anhydride C=O asymmetric and symmetric stretching, respectively [78, 79]. SMAgF* shows two broad and weak peaks at 1711 and 1653 $cm^{-1}$, assigned to C=O stretching of carboxylic acid and secondary amide, respectively, likely relatable to FFA reaction with the anhydride through the ring opening [78]. After thermal annealing SMAgF shows two peaks at 1778 $cm^{-1}$ and 1705 $cm^{-1}$, that together can be assigned to imide groups (C=O symmetric and asymmetric stretching, respectively), obtained by the amides and carboxylic acid groups condensation [80], while 1778 $cm^{-1}$ signal is also assigned to residual anhydride groups, condensed from carboxylic acid groups during the thermal treatment. Further evidence for the achievement of furan grafting on the rubber chain can be obtained by the analysis of the FT-IR region for furan ring deformation. Indeed, the band at 599 $cm^{-1}$ in the FFA spectrum was previously assigned to furan ring deformation [78, 81]. The same signal is clearly visible in SMAgF spectra, and since FFA has a boiling temperature of 145°C, its presence after the thermal treatment (180°C in vacuum) confirms the furan grafting on the SMA polymer chains.

Regarding the melt blending method, the FT-IR spectrum is similar to the equivalent formulation prepared in solvent: the process temperature (170°C) appears to allow efficient diene functionalization, since in SMAgF the couple of 1778 and 1707 $cm^{-1}$ signals are detected, assignable to C=O symmetric and asymmetric stretching, respectively, of imide groups, and to residual anhydride, as in the case of THF preparation, together with the presence in SMAgF of the furan ring deformation vibration signal at 599 $cm^{-1}$.

**Polyethylene grafted with maleic anhydride**

Figure 47 reports the grafting reaction scheme on PEgMA, starting from the reaction of PEgMA with FFA, through an amide intermediate and eventually to the furfuryl imide derivative (PEgF), performed by melt processing.

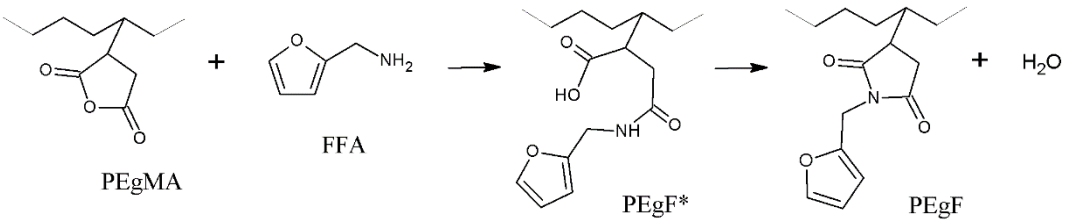


Figure 47. Scheme of the furan functionalization of PEgMA.

Furan grafting on PEgMA was assessed by transmission FT-IR spectroscopy. In Figure 48 FT-IR spectra of PEgMA, PEgF* and PEgF are reported, while assignments are summarized in Table 5.

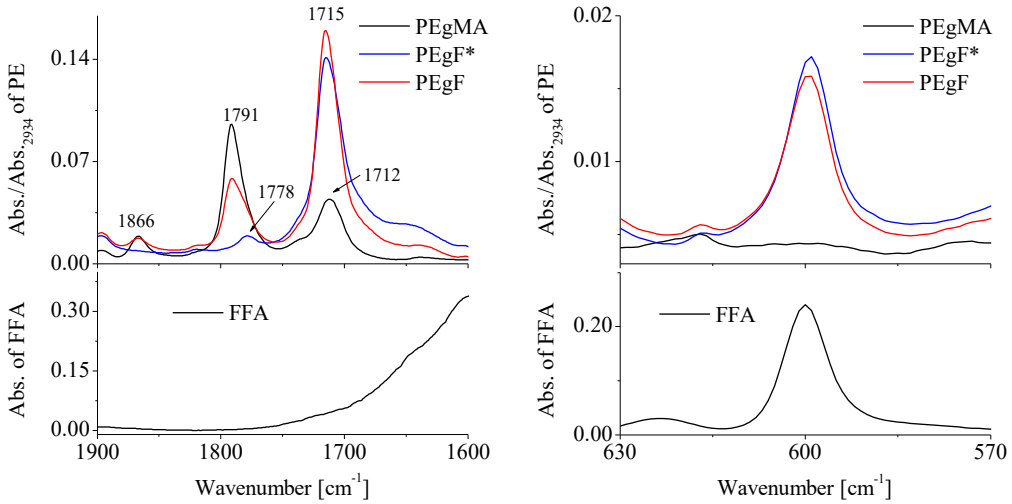


Figure 48. Transmission FT-IR spectra relating to PEgMA functionalization with FFA in the range 1900-1600 cm$^{-1}$ and 630-570 cm$^{-1}$ (PE spectra are normalized on their higher peak at 2934 cm$^{-1}$, assigned to C-H stretching vibration on the aliphatic chain of the polymer, while FFA spectrum is not normalized).

In the 1900-1600 cm$^{-1}$ range pristine PEgMA spectrum exhibits two peaks at 1866 and 1791 cm$^{-1}$, assigned to C=O asymmetric and symmetric stretching of anhydride, respectively, and a peak at 1712 cm$^{-1}$, assigned to C=O stretching of carboxylic acid [78, 79], due to the hydrolysis of anhydride groups to dicarboxylic acids [82]. PEgF* shows a strong peak at 1715 cm$^{-1}$ which can be assigned to the

overlapping of signal from carboxylic acid groups as well as from imide groups (C=O asymmetric stretching [80]), together with the signal at 1778 $cm^{-1}$ (C=O symmetric stretching). In PEgF the broader and asymmetric band around 1791 $cm^{-1}$ appears as a convolution of two signals: 1791 $cm^{-1}$ for C=O symmetric stretching of residual anhydride condensed after thermal annealing and 1778 $cm^{-1}$ for C=O symmetric stretching of imide, that together with the persistence of the strong peak at 1715 $cm^{-1}$ (not consistent anymore with carboxylic acid after the high-temperature annealing), brings evidence of the formation of imide groups. Besides, the achievement of furan grafting on the chain is proved by the presence of the signal at 599 $cm^{-1}$, assigned to furan ring deformation [78, 81], in PEgF* and also in PEgF after the high-temperature vacuum annealing, not consistent with the presence of FFA after the thermal treatment.

**Ethylene-propylene rubber grafted with maleic anhydride**

Figure 49 describes the grafting reaction scheme, starting from the reaction of EPRgMA with FFA, through an amide intermediate and eventually to the furfuryl imide derivative (EPRgF), performed by melt processing.

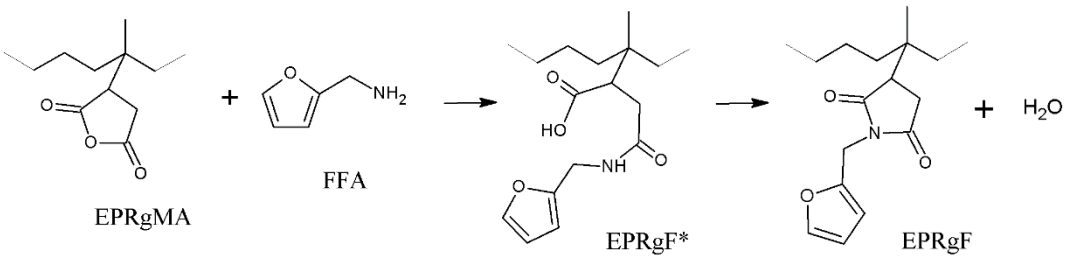


Figure 49. Scheme of the furan functionalization of EPRgMA.

Furan grafting on EPRgMA was assessed by FT-IR spectroscopy. In Figure 50 FT-IR spectra of FFA, EPRgMA, EPRgMA_ann, EPRgF* and EPRgF are reported, while assignments are summarized in Table 5.

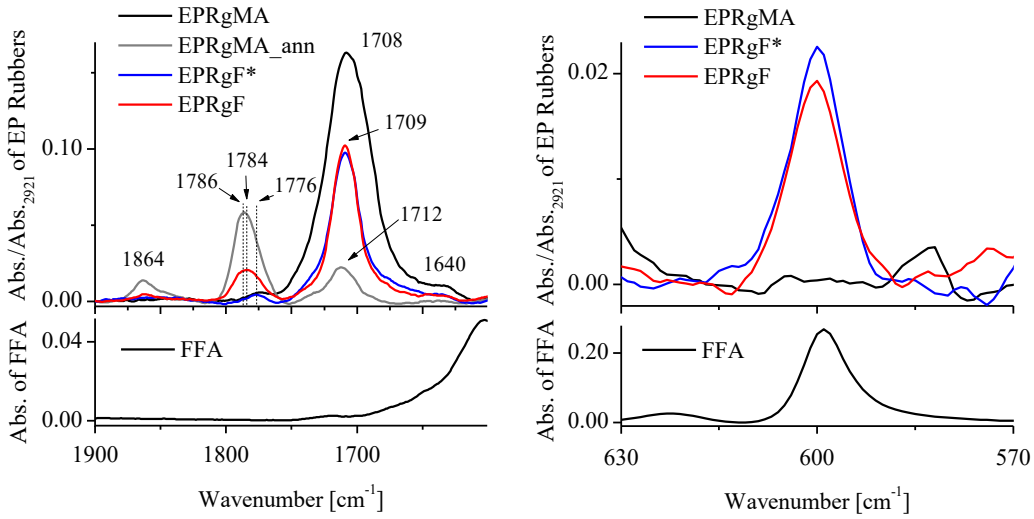


Figure 50. ATR FT-IR spectra relating to EPRgMA functionalization with FFA in the range 1900-1600 $cm^{-1}$ and 630-570 $cm^{-1}$ (EP Rubbers spectra are normalized on their higher peak at 2921 $cm^{-1}$, assigned to C-H stretching vibration on the aliphatic chain of the rubbers, while FFA spectrum is not normalized).

In the 1900-1600 $cm^{-1}$ range, as received EPRgMA spectrum shows a strong absorption band centered at 1708 $cm^{-1}$, assigned to C=O stretching of carboxylic acid [78, 79], confirming the hydrolysis of anhydride groups to dicarboxylic acids [82]. EPRgMA_ann spectrum exhibits a decreased carboxylic acid C=O signal at 1712 $cm^{-1}$ and two new bands, at 1864 and 1786 $cm^{-1}$, that are typical of cyclic anhydride C=O asymmetric and symmetric stretching, respectively [78, 79], supporting for the actual conversion to anhydride, via condensation of carboxylic groups under high temperature and reduced pressure [83]. The IR spectrum for melt mixed EPRgMA was found equivalent to the spectrum for EPRgMA_ann (Figure 51), confirming efficiency of conversion during melt processing.

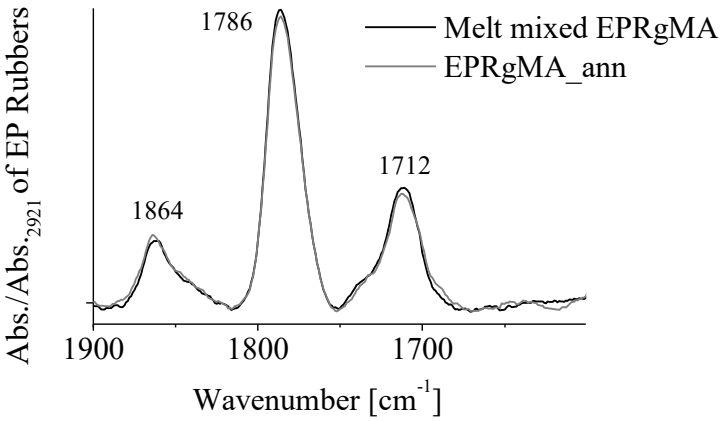


Figure 51. ATR FT-IR spectra in the range 1900-1600 $cm^{-1}$ of EPRgMA after melt processing and after annealing.

EPRgF* exhibits a strong peak at 1709 $cm^{-1}$, with an intensity intermediate between that of EPRgMA and EPRgMA_ann, which can be explained by residual carboxylic acid groups as well as by the formation of imide groups [80]. Instead, EPRgF presents a band at 1864 $cm^{-1}$ together with another at 1784 $cm^{-1}$, while a slightly sharper and similarly intense peak at 1709 $cm^{-1}$ was retained compared to EPRgF*. This suggests that the thermal annealing in vacuum promoted the condensation of carboxyl groups to anhydride and may complete the condensation of possible amide groups with adjacent carboxyl group to increase the concentration of imide groups. This is further supported by the shape of the broad band centred at 1784 $cm^{-1}$, which is downshifted and broader than for EPRgMA_ann, suggesting an overlap between the signals of C=O symmetric stretching of the anhydride and C=O symmetric stretching of the imide at 1776 $cm^{-1}$. Overall, these results demonstrate that the grafting of FFA was indeed obtained, although the conversion of available MA groups was not quantitative, despite excess of amine, which likely depends on the competition between the amine-anhydride reaction and the FFA evaporation under melt blending conditions. Further evidence for the achievement of furan grafting on the rubber chain can be obtained by the analysis of the FT-IR region for furan ring deformation. The band at 599 $cm^{-1}$ in the FFA spectrum, previously assigned to furan ring deformation [78, 81], is clearly visible in EPRgF* and EPRgF spectra, thus confirming the furan grafting on the EPR polymer chains.

## 3.1.2. Thermoreversible crosslinking with bifunctional dienophile

### Styrene maleic anhydride grafted with furan

In order to obtain a thermoreversible crosslinking of SMA, SMAgF (obtained by melt processing) was blended with BM in stoichiometric ratio. In Figure 52, the scheme of the SMAgF-BM crosslinking reaction is reported.

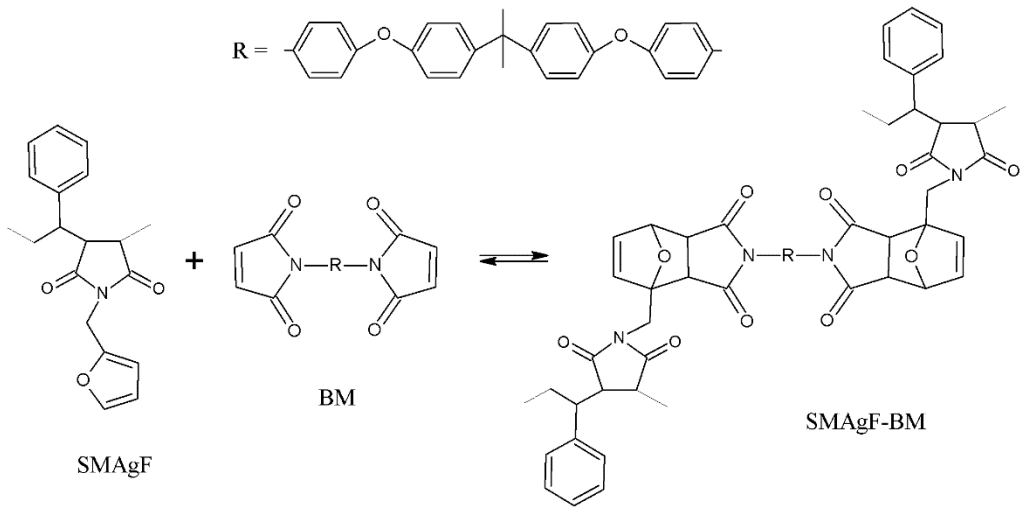


Figure 52. Scheme of SMAgF crosslinking with BM.

The SMAgF-BM blend resulted to be very brittle and the attempts to hot-pressing provided discontinuous and cracked films. This is likely due to the low molecular weight of pristine SMA (10000 g/mol). Although mechanical properties were not investigable, ATR FT-IR spectra of SMAgF-BM were studied (Figure 53 (a), (b) and (c)), with assignments summarized in Table 6.

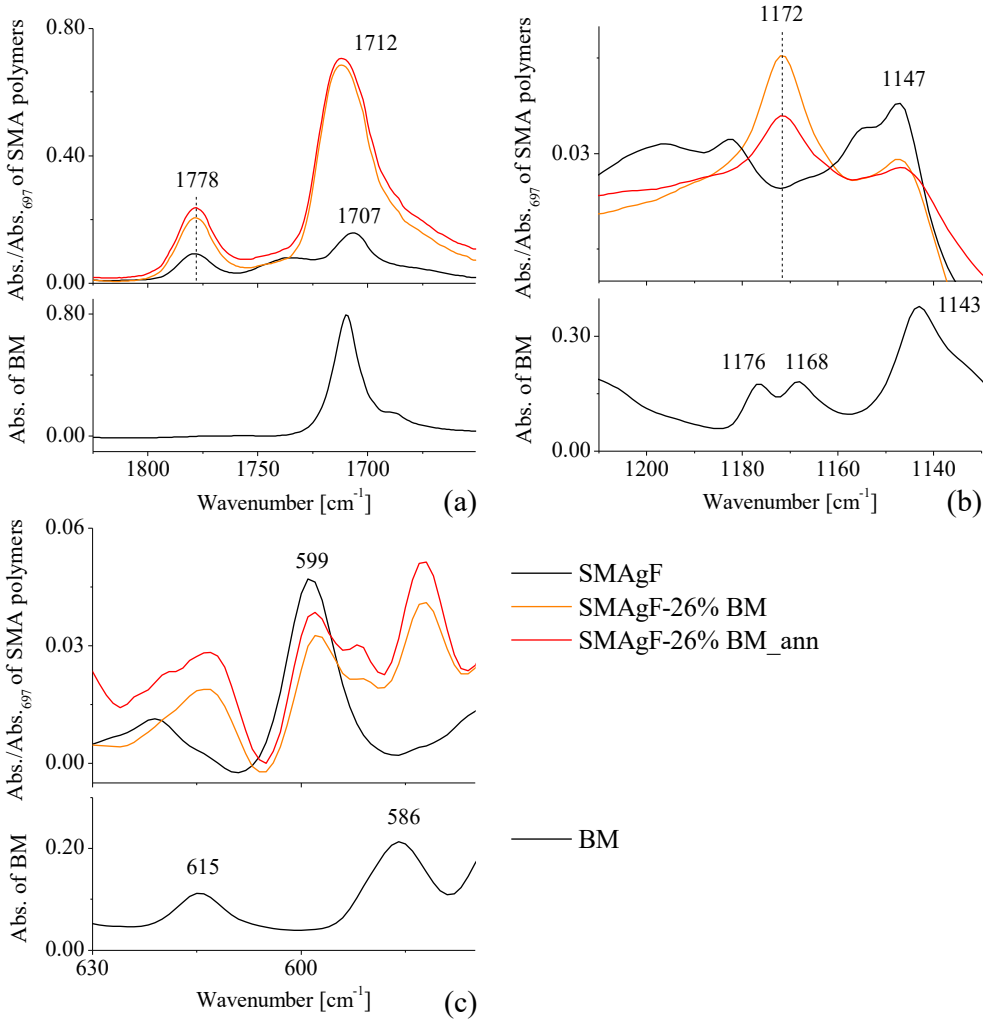


Figure 53. ATR FT-IR spectra of SMAgF and its crosslinked network in the range 1825-1650 $cm^{-1}$ (a), 1210-1130 $cm^{-1}$ (b) and 630-575 $cm^{-1}$ (c).

Table 6. Assignments of FT-IR spectra for SMAgF-26%BM characterization.

| **Wavenumber** [$cm^{-1}$] | **Assignment** |
|---|---|
| *1778* | C=O symmetric stretching of imide |
| *1715-1710* | C=O asymmetric stretching of imide |
| *1172* | C-O-C stretching band in furan ring |
| *599* | Furan ring deformation |

In the 1825-1650 $cm^{-1}$ region (Figure 53 (a)), BM spectrum shows a strong peak at 1710 $cm^{-1}$, assigned to C=O asymmetric stretching of maleimide. SMAgF-26%BM spectra shows a strong C=O asymmetric stretching signal at 1712 $cm^{-1}$ as well as the C=O symmetric stretching at 1778 $cm^{-1}$, which appear related to the presence of the imide in BM. FT-IR spectra in the range 1210-1130 $cm^{-1}$ (Figure 53 (b)) were also studied, as the C-O-C stretching band in furan ring can be observed at 1143 $cm^{-1}$ in SMAgF [78]. In the SMAgF-26%BM spectra a peak at 1172 $cm^{-1}$ is clearly visible, which does not correlate to the bands in BM spectrum at 1176 $cm^{-1}$ and 1168 $cm^{-1}$ and it was previously associated to a shift of C-O-C stretching due to DA adduct formation [84]. In the low FT-IR wavenumber region (Figure 53 (c)), BM spectrum shows two peaks at 615 and 586 $cm^{-1}$, while in the SMAgF-26%BM spectra, a decrease of the peak at 599 $cm^{-1}$, assigned to furan ring deformation, was found, which further supports the formation of the DA adduct. Despite that, the assessed crosslinking is not sufficient to generate continuous and not-cracked films, likely due to the low molecular weight of SMA, which is typically related to low toughness in polymers [85]. Indeed, a low and possibly inhomogeneous crosslinking degree in this low molecular weight polymer can produce dangling chains and free chains which, in fact, behave as a low molecular weight thermoplastic polymer under its glass transition temperature, and so very brittle.

**Polyethylene grafted with furan**

In order to obtain a thermoreversible crosslinked network, PEgF was blended with an oligomeric aliphatic bismaleimide (BM1) in stoichiometric ratio. This was selected based on the predicted greater affinity with a polyethylene based polymer. In Figure 54, the scheme of the PEgF-BM1 crosslinking reaction is reported.

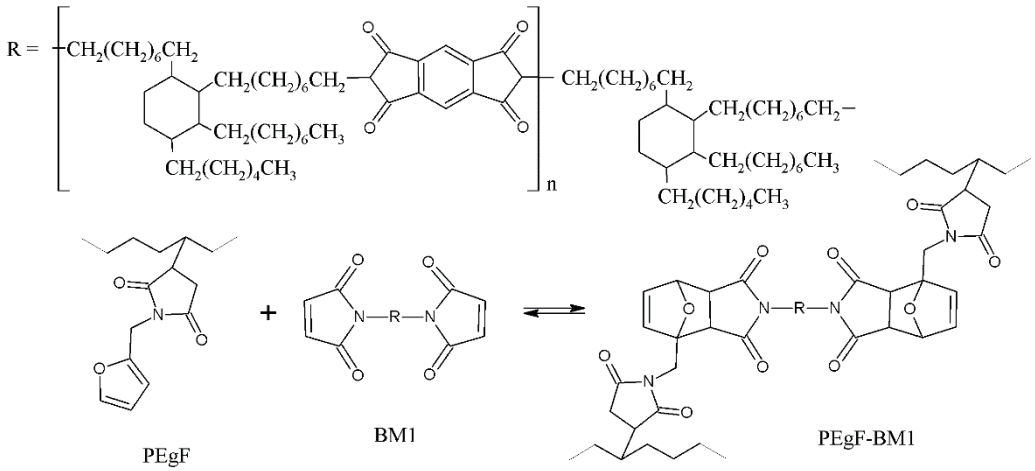


Figure 54. Scheme of PEgF crosslinking with BM1.

To investigate DA crosslinking formation between furan and maleimide groups, transmission FT-IR spectrum of PEgF-BM1 was studied (Figure 55 (a) and (b)).

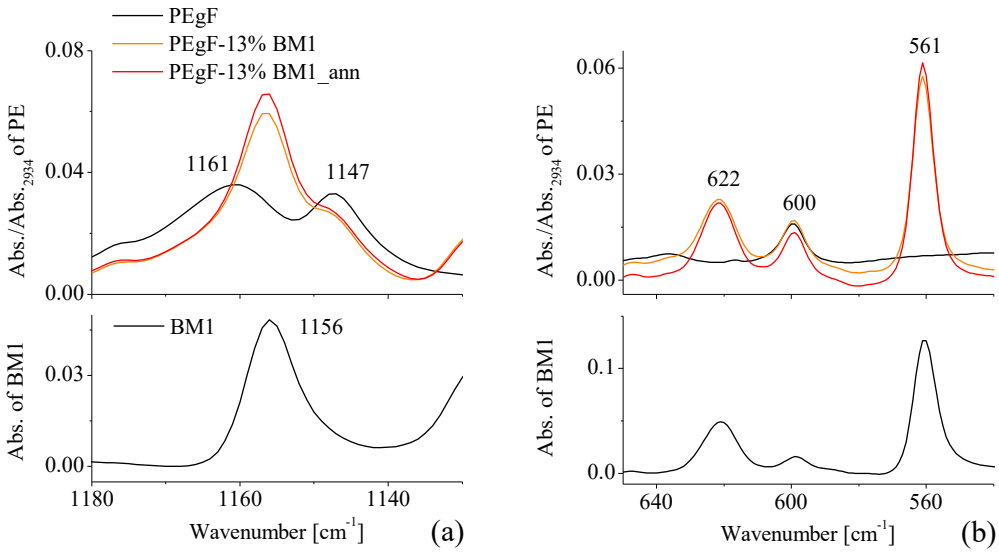


Figure 55. Transmission FT-IR spectra of PEgF and its crosslinked network in the range 1180-1130 $cm^{-1}$ (a) and 650-540 $cm^{-1}$ (b).

The C=O region (1900-1600 $cm^{-1}$) is not useful to investigate the DA crosslinking reaction due to the intense carbonyl signals of BM1 chain. In the mid-range C-O-C region (1180-1130 $cm^{-1}$) the signal at 1147 $cm^{-1}$ previously assigned to furan ring is clearly visible in PEgF, but its possible shifting after crosslinking is hardly detectable due to the presence of a band at 1156 $cm^{-1}$ in BM1. Also in the

low-range region of the spectrum the numerous signals of BM1 make the investigation of DA crosslinking difficult to assess by FT-IR spectroscopy.

The effect of the possible crosslinking on mechanical properties was also evaluated by tensile tests on PEgMA, PEgF and its BM1 blend samples, either as obtained or after annealing (Figure 56 and Table 7).

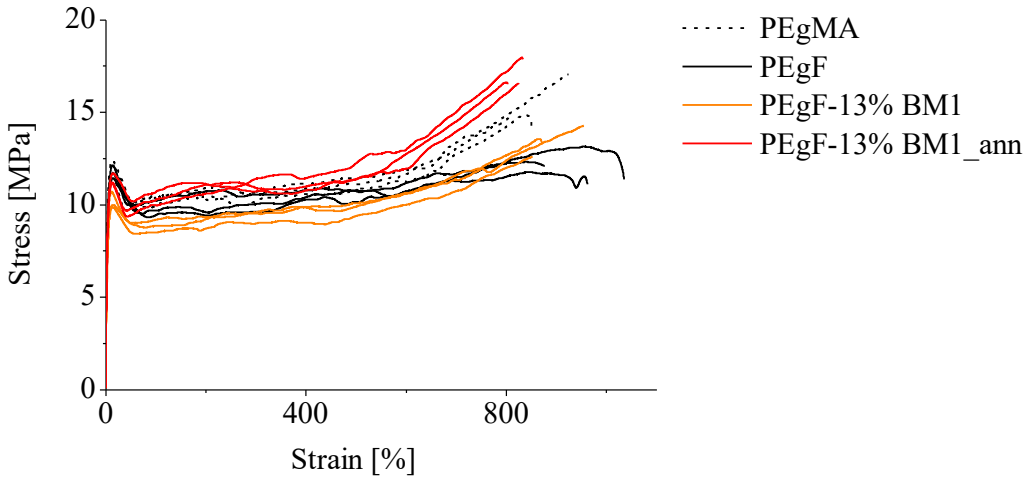


Figure 56. Stress-strain curves of PEgMA, PEgF and PEgF-13%BM1.

Table 7. Average Young's modulus E, tensile strength $\sigma_{max}$ and elongation at break $\varepsilon_b$ with their standard deviations of PEgMA, PEgF and PEgF-13%BM1.

| | **Average ± *st. dev.* of E** [GPa] | **Average ± *st. dev.* of $\sigma_{max}$** [MPa] | **Average ± *st. dev.* of $\varepsilon_b$** [%] |
|---|---|---|---|
| *PEgMA* | 0.40 ± *0.03* | 15.5 ± *1.3* | 860 ± *59* |
| *PEgF* | 0.36 ± *0.04* | 12.1 ± *0.7* | 947 ± *65* |
| *PEgF-13%BM1* | 0.26 ± *0.01* | 13.5 ± *0.8* | 891 ± *56* |
| *PEgF-13%BM1_ann* | 0.33 ± *0.01* | 17.1 ± *0.8* | 819 ± *17* |

In PEgF, furan grafting brings to a slight decrease in stiffness and tensile strength, compared to pristine PEgMA. This can be explained by the conversion of maleic acid or maleic anhydride groups, that are producing hydrogen bonds between the chains in PEgMA, whereas such groups are much less abundant in PEgF after FFA grafting. Blending PEgF with BM1 does not bring relevant changes in mechanical properties, except for the increase of tensile strength (from 12.1 MPa

of PEgF to 17.1 MPa for PEgF-13%BM1_ann), but not remarkably higher than pristine PEgMA (15.5 MPa), as can be seen in Figure 56. Therefore, these preliminary studies on PEgMA point out poor crosslinking effects, likely due to a very low or absent crosslinking density, which can be the result of the low MA content (1 wt%) in PEgMA (and accordingly of furan groups in PEgF) and to the relatively high molecular weight of the crosslinker (3000 g/mol).

**Ethylene-propylene rubber grafted with furan**

To obtain a thermoreversible crosslinking of the rubber, BM (selected as a shorter crosslinker compared to BM1) was blended with EPRgF, in different percentages. In Figure 57, the scheme of the crosslinking reaction is reported.

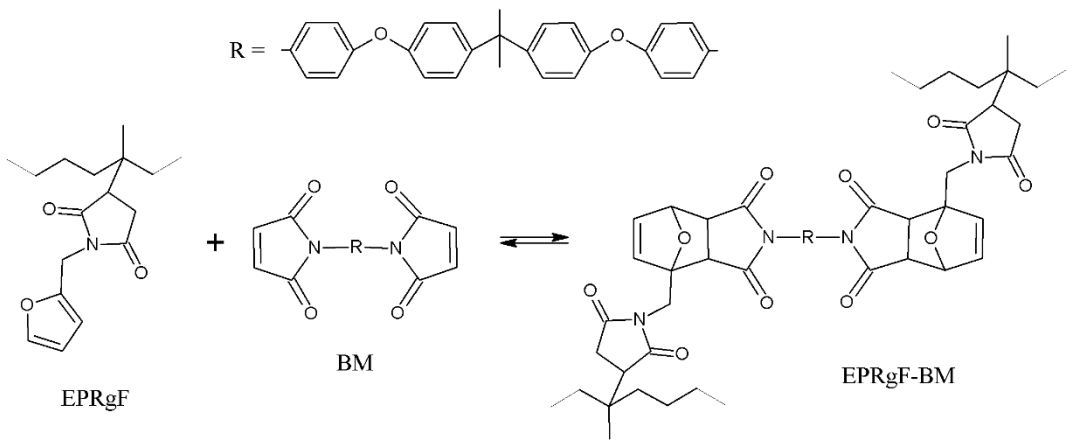


Figure 57. Scheme of EPRgF crosslinking with BM.

The morphology of EPRgF-BM was observed by SEM imaging (Figure 58), which did not show evidences for phase separation at the microscale, regardless the concentration of BM, thus confirming homogeneous distribution of BM in EPRgF, despite its partially aromatic structure.

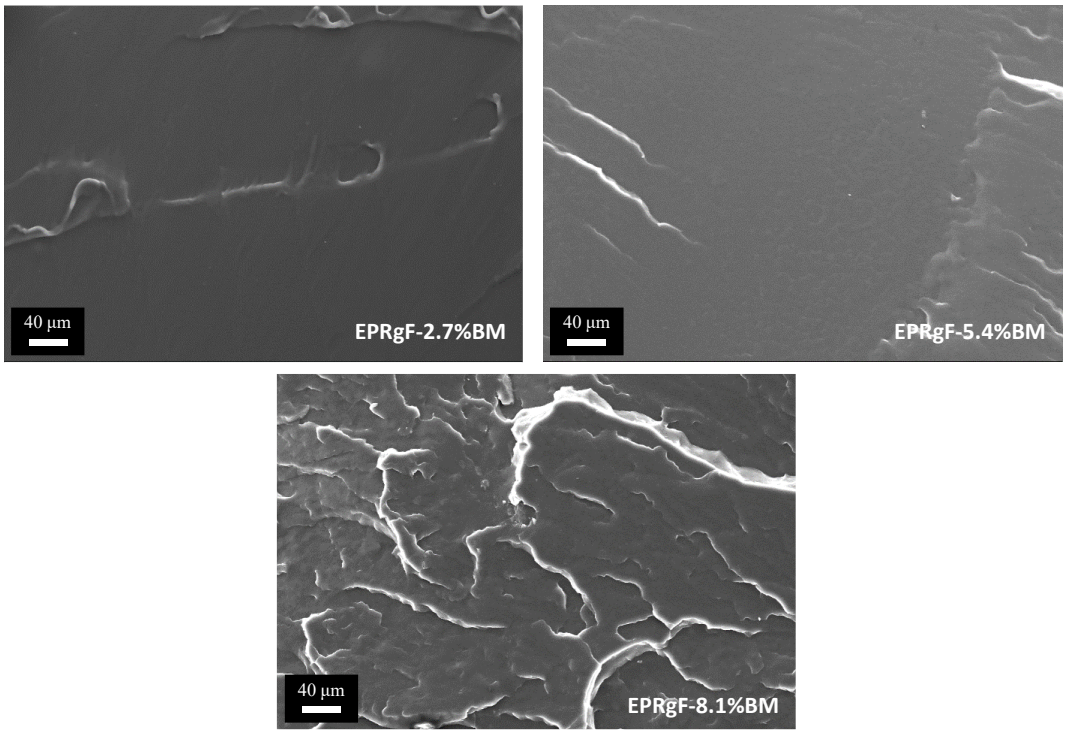


Figure 58. SEM images of EPRgF-2.7%BM, EPRgF-5.4%BM and EPRgF-8.1%BM.

DSC was also carried out as an attempt to identify temperatures for DA and retro-DA reactions. Indeed, the direct and retro reactions are reported to generate an exothermic (adduct formation) and endothermic (adduct dissociation) peak, respectively [86]. Unfortunately, the thermograms for the different EPRgF-BM (Figure 59) do not show clear signals for DA transitions, likely due to the low concentration of crosslinking and the limited sensitivity of DSC technique.

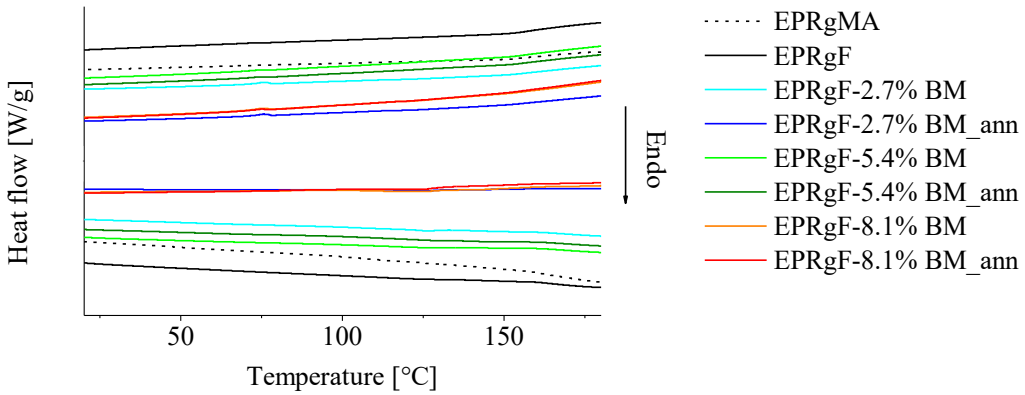


Figure 59. DSC thermograms of EPRgMA, EPRgF and EPRgF-BM.

To detect DA adduct formation between furan and maleimide moieties, ATR FT-IR spectra of the EPRgF-BM compounds were studied in details (Figure 60 (a), (b) and (c)), leading to assignments summarized in Table 8.

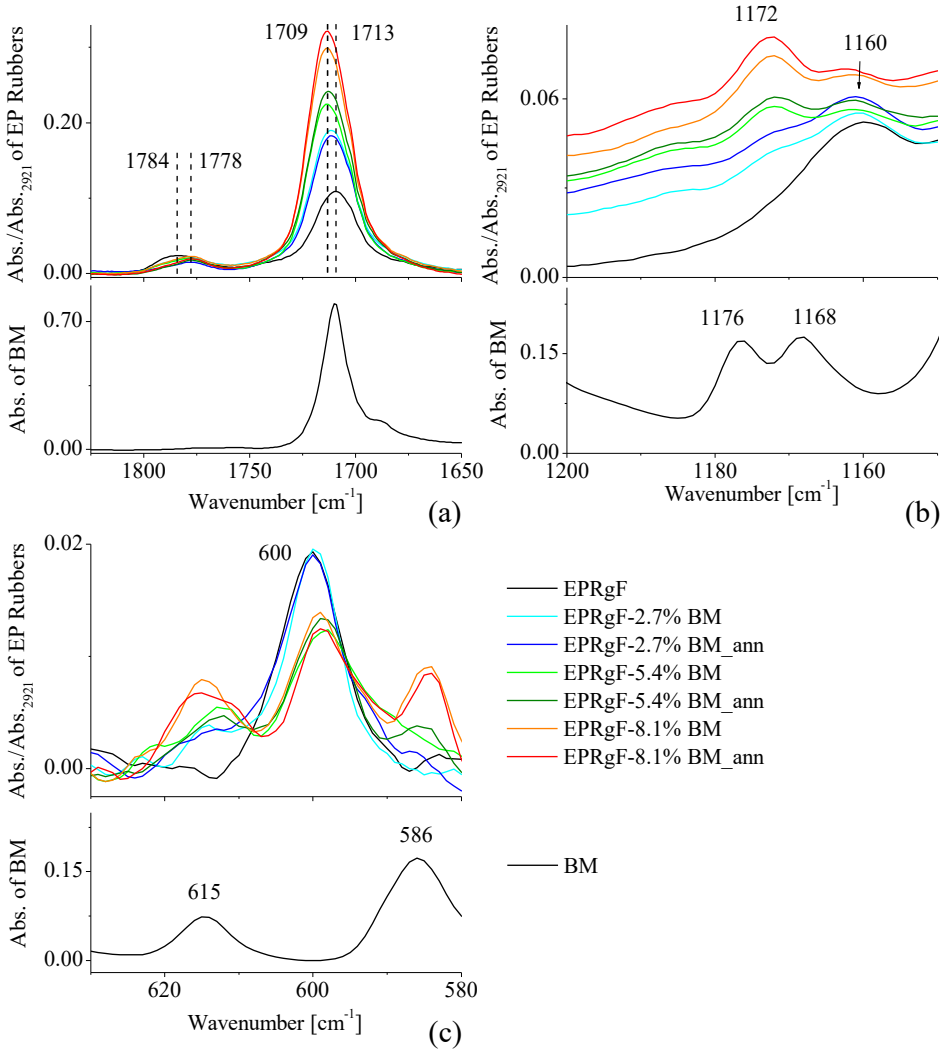


Figure 60. ATR FT-IR spectra of EPRgF and its crosslinked networks in the range 1825-1650 $cm^{-1}$ (a), 1200-1150 $cm^{-1}$ (b) and 630-580 $cm^{-1}$ (c).

Table 8. Assignments of FT-IR spectra for EPRgF-BM characterization.

| **Wavenumber** [$cm^{-1}$] | **Assignment** |
|---|---|
| *1778* | C=O symmetric stretching of imide |
| *1713* | C=O asymmetric stretching of imide |

| | |
|---|---|
| *1172-1160* | C-O-C stretching band in furan ring |
| *600* | Furan ring deformation |

In the C=O stretching region (Figure 60 (a)), BM spectrum shows a strong band at 1710 $cm^{-1}$, assigned to C=O asymmetric stretching of maleimide. EPRgF-BM spectra exhibit strong C=O asymmetric stretching signal centred around 1713 $cm^{-1}$, which appears related to the presence of the imide in BM, as these signals increase in intensity with increasing the BM concentrations and are not significantly modified by thermal annealing. Moreover, all the EPRgF-BM spectra show a C=O symmetric stretching at 1778 $cm^{-1}$, which is significantly shifted compared to EPRgF (1784 $cm^{-1}$) spectrum. This behaviour may be related to the formation of the DA adduct between furan and maleimide, that generate a change of the C=O vibration mode of cyclic imides, depending on their chemical environment, in agreement with a previous literature report [84]. FT-IR spectra in the range 1200-1150 $cm^{-1}$ (Figure 60 (b)) were also studied, as the C-O-C stretching band in furan ring can be observed at 1160 $cm^{-1}$ in EPRgF [78]. In the EPRgF-BM spectra, such signal appears of lower intensity, while a peak at 1172 $cm^{-1}$ is clearly visible, of increasing intensity with BM concentration and almost independent on the thermal annealing. This band does not seem correlated to the bands in BM spectrum at 1176 $cm^{-1}$ and 1168 $cm^{-1}$ and it was previously associated to a shift of C-O-C stretching due to DA adduct formation [84]. In the low FT-IR wavenumber region (Figure 60 (c)), BM spectrum shows two peaks at 615 and 586 $cm^{-1}$, which do not overlap significantly with of furan ring deformations in the range of 600 $cm^{-1}$. In the EPRgF-BM spectra, the characteristic peaks of BM at approx. 586 $cm^{-1}$ is clearly visible, increasing in intensity with BM concentration. On the other hand a decrease of the peak at 600 $cm^{-1}$, assigned to furan ring deformation was found, which further supports the formation of the DA adduct.

With the aim of proving accomplished crosslinking in the rubber, solubility tests were carried out, knowing both EPRgMA and EPRgF are highly soluble in toluene at room temperature. Conversely, all the BM-added rubbers turned out to be poorly soluble in the same solvent. Instead, the EPRgF-BM showed swelling in toluene and the solid residue was collected to determine the crosslinking degree (Figure 61) for each formulation, after solvent removal.

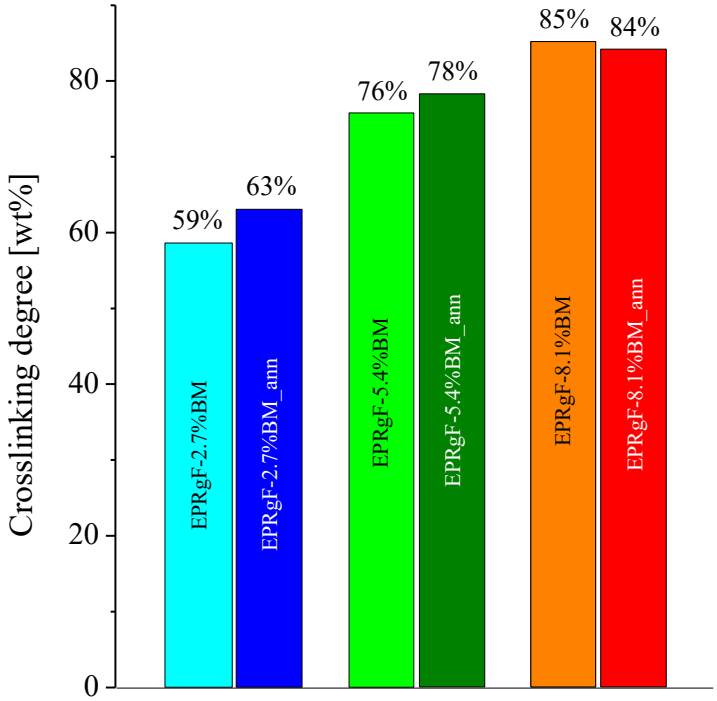


Figure 61. Percentage of remained rubber after overnight soaking in toluene.

The crosslinking degree increases up to about 85% with 8.1 wt% BM content. Furthermore, the thermal annealing brings an increase of crosslinking degree for the lower BM concentrations, evidencing for a slight optimization of crosslinking when the materials is given time to complete DA adduct formation, whereas variation within the experimental error was found for EPRgF-8.1%BM. These results suggest maximum crosslinking is reached at 8.1%BM, which cannot be enhanced further by thermal annealing.

To prove the reversible character of DA crosslinking, solubility test on EPRgF-5.4%BM_ann in boiling toluene has also been performed. It resulted that the crosslinked formulation, with an insoluble fraction at room temperature, after 3 hours in boiling toluene were completely solubilized. In Figure 62, pictures of a EPRgF-5.4%BM_ann film soaked toluene were captured before (a) and after (b) 3 hours in boiling toluene.

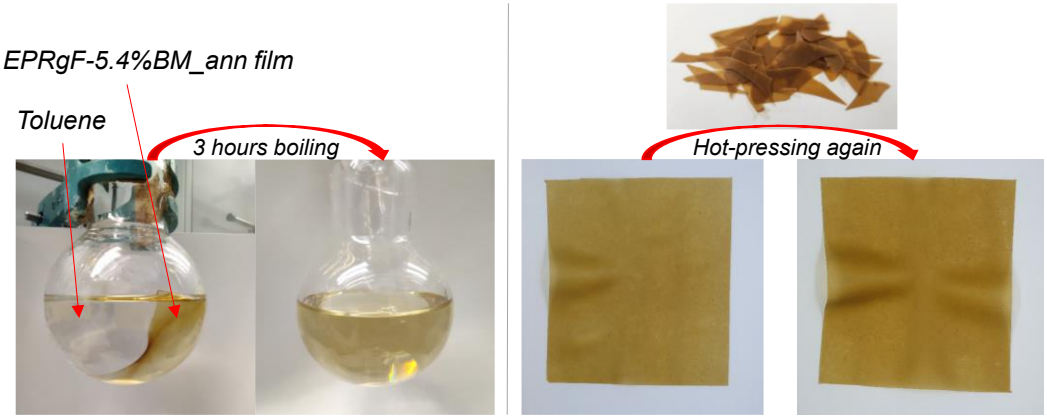


(a) (b) (c) (d)

Figure 62. EPRgF-5.4%BM_ann film in toluene before and after 3 hours boiling. A solid film is clearly visible in (a), whereas a solution in (b). Re-moulding via hot-pressing of a EPRgF-5.4%BM film (c) in a new one (d).

The great difference in solubility at room temperature vs high temperature (ca. 110°C) evidences for the achievement of a covalent crosslinking at room temperature, yet thermoreversible via retro DA reaction at high temperature. To bring further evidence of reversible crosslinking, EPRgF-BM films were chopped and hot-pressed again at 150°C into a new film. It turned out that it was always possible to obtain homogenous films (Figure 62 (c) and (d)), suggesting the material flows similarly to a thermoplastic polymer, thanks to the promotion of retro-Diels-Alder reaction at this temperature and to the consequent temporary breaking of crosslinks.

To further investigate the rubber behaviour at processing temperature (150°C), rheology tests were performed at the same temperature (Figure 63).

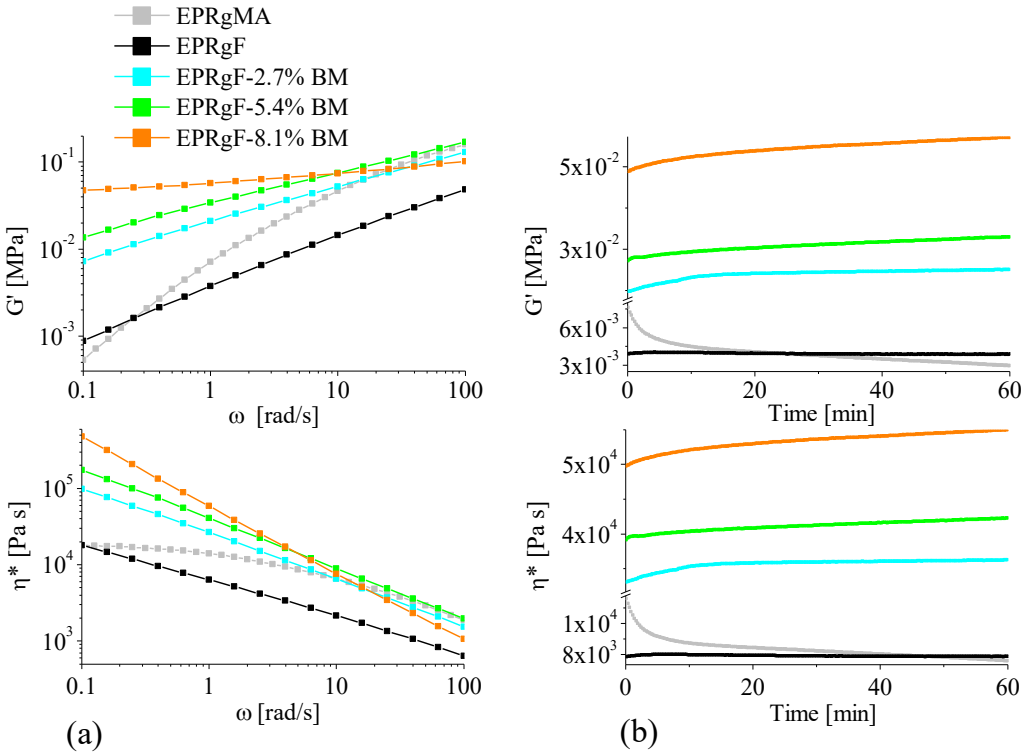


Figure 63. Storage modulus (G′) and complex viscosity (η*) in function of angular frequency (ω) (a) and time (b), at constant temperature and strain, for EPRgMA, EPRgF and EPRgF-BM networks.

In frequency sweep mode (Figure 63 (a)), G′ plots for EPRgF-BM networks show a significantly lower slope at low frequencies, compared to EPRgMA and EPRgF, which is consistent to a crosslinked character, bringing evidence of the presence of DA adducts linking the chains even at 150°C. This is further confirmed by the lower slope for EPRgF-8.1%BM compared to EPRgF-2.7%BM and EPRgF-5.4%BM, which is in agreement with the higher crosslinking degree observed at low temperature. Complex viscosity curves for the rubber networks show high viscosity at low frequencies, approx. one order of magnitude higher than EPRgMA and EPRgF, with a progressive increase with the content of BM (consistent with G′ curves) and clear shear thinning behaviour leading to a drastic decrease of viscosity with increasing frequency. Isothermal (150°C) stability measurements (Figure 63 (b)) confirm these observations, showing a progressive annealing of the samples, with slightly increasing G′ and η* with time. Indeed, while the retro DA was shown to be thermally activated at lower temperature (Figure 62), it should be noted that the DA is an equilibrium reaction, which can be shifted to the dissociated side when increasing temperature [87], while still retaining a fraction of bound chains. These contribute to the high viscosity and solid-like behaviour of the EPRgF-BM

formulations, especially when containing relatively high BM concentrations. While partial cleavage of the network may be sufficient to solubilize the rubber in a solvent at relatively low temperature, re-association of furan and maleimide moieties is strongly favoured in the molten state, which therefore requires significantly higher temperatures to obtain a melt-processable fluid, also taking into account of the viscosity of the pristine polymer. In fact, despite DA-crosslinked polymers are traditionally considered as dissociative networks, these present some similarities with an associative dynamic network, where the crosslink density depends on the temperature and in principle remains constant during processing. Therefore, in this case, boundaries between covalent associative and covalent dissociative networks does not appear well defined, which was in fact recently discussed already for 1,2,3-triazolium-based dissociative networks [88].

To further investigate dynamic crosslinking in EPRgF-BM rubbers as a function of temperature, rheology measurement in temperature ramp were performed (Figure 64).

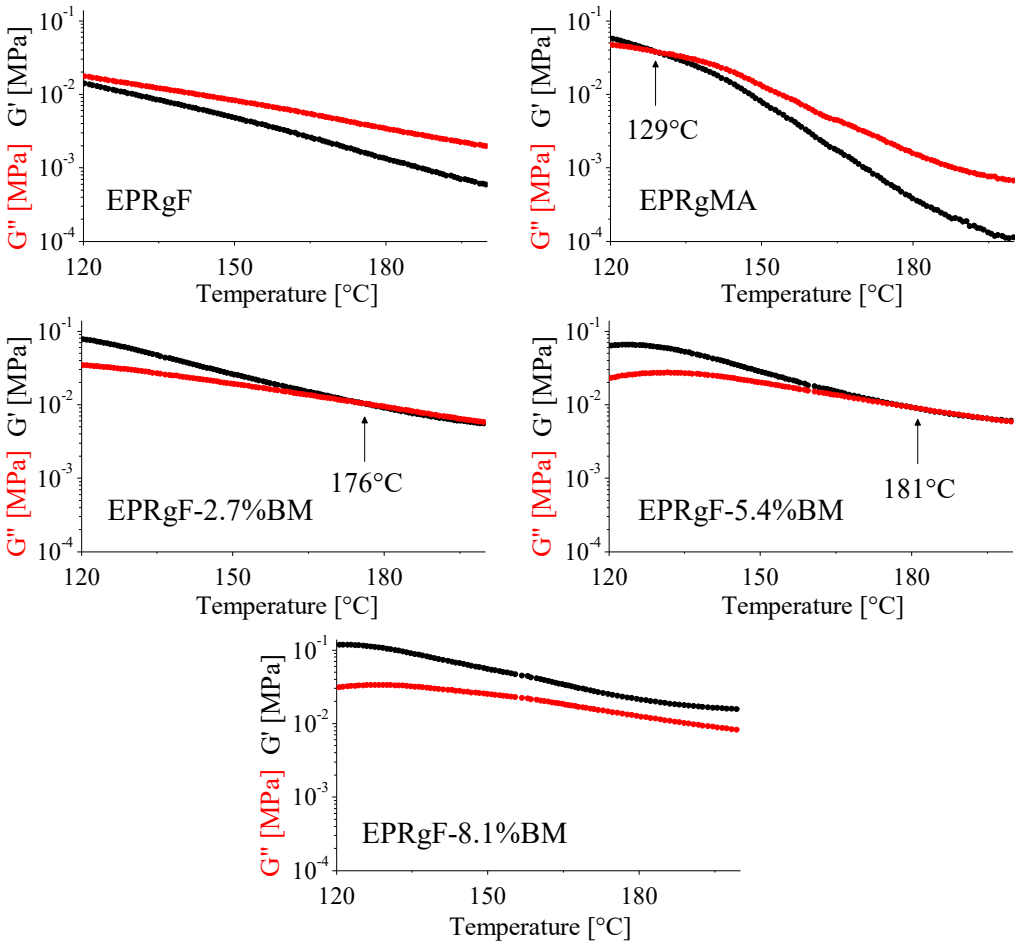


Figure 64. Storage modulus (G´) and loss modulus (G´´) in function of temperature, at constant frequency and strain, for EPRgMA, EPRgF and EPRgF-BM networks.

EPRgF shows a liquid-like behaviour as expected as these temperatures, with G´´> G´ over the whole temperature range. The higher G' of EPRgMA at low temperatures may be explained by hydrogen bonding between chains through carboxylic and/or anhydride groups, which are not possible or strongly limited in EPRgF, where the majority of MA groups were previously reacted with FFA. In EPRgF-BM, G' is dominant over the whole temperature range at 8.1% BM content, whereas a transition from solid-like to liquid-like behaviour is found at lower BM contents. The temperature at which this transition is observed depends on the BM content, namely 176°C for EPRgF-2.7%BM, 181°C for EPRgF-5.4%BM), which is significantly higher than the temperature (ca. 110°C) sufficient to dissolve the rubber in solvent. This confirms an equilibrium state for the DA reaction in the melt, which is shifted in temperature and depends on the concentration of BM, namely increasing the effective crosslinking at 150°C with increasing BM content.

At room temperature, the effect of crosslinking on the rubber has been also investigated through its mechanical properties, performing tensile testing on EPRgMA, EPRgF and EPRgF-BM with different amount of crosslinking agent, both before and after thermal annealing. Figure 65 reports the resulting stress-strain curves of the three EPRgF-BM formulations, both as obtained and after a thermal annealing. In Table 9, the corresponding average Young's modulus (E), tensile strength ($\sigma_{max}$) and elongation at break ($\varepsilon_b$) are reported with their standard deviations.

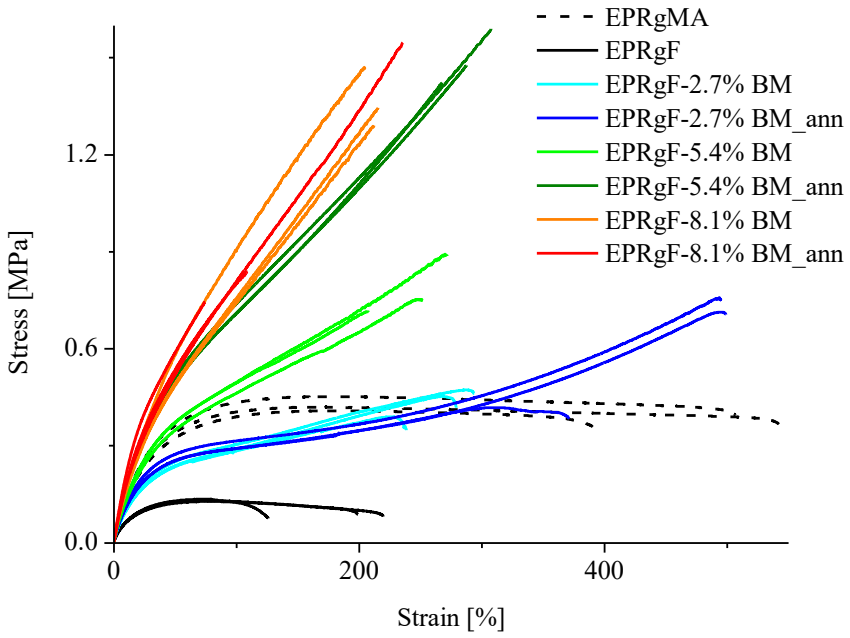


Figure 65. Stress-strain curves of EPRgMA, EPRgF and EPRgF-BM networks.

Table 9. Average Young's modulus E, tensile strength $\sigma_{max}$ and elongation at break $\varepsilon_b$ with their standard deviations of EPRgMA, EPRgF and EPRgF-BM.

| | **Average ± *st. dev.* of E** [MPa] | **Average ± *st. dev.* of $\sigma_{max}$** [MPa] | **Average ± *st. dev.* of $\varepsilon_b$** [%] |
|---|---|---|---|
| EPRgMA | 1.14 ± *0.46* | 0.43 ± *0.02* | 482 ± *78* |
| EPRgF | 0.49 ± *0.14* | 0.13 ± *0.00* | 182 ± *49* |
| EPRgF-2.7%BM | 1.05 ± *0.14* | 0.44 ± *0.04* | 270 ± *29* |
| EPRgF-2.7%BM_ann | 1.11 ± *0.10* | 0.63 ± *0.18* | 455 ± *73* |

| | | | |
|---|---|---|---|
| EPRgF-5.4%BM | 1.38 ± *0.10* | 0.79 ± *0.09* | 244 ± *33* |
| EPRgF-5.4%BM_ann | 1.44 ± *0.26* | 1.50 ± *0.09* | 288 ± *20* |
| EPRgF-8.1%BM | 1.37 ± *0.28* | 1.36 ± *0.09* | 211 ± *5* |
| EPRgF-8.1%BM_ann | 1.68 ± *0.11* | 1.04 ± *0.44* | 140 ± *85* |

EPRgMA is a soft and highly stretchable polymer, displaying an E of approx. 1.14 MPa and elongation at break in the order of 500%. A drastic decrease of Young's modulus, elongation and tensile strength was observed for EPRgF, compared to EPRgMA. The higher performances of EPRgMA are explained, as already said in rheology measurements at low temperatures, by hydrogen bonding between chains. Regarding BM-crosslinked polymers, a progressive reinforcement of the rubber was obtained with the concentration of BM, with clear enhancement of the elastic modulus (approx. 1.44 MPa for EPRgF-5.4%BM_ann) and tensile strength (approx. 1.50 MPa for the same material, versus 0.43 MPa for EPRgMA), along with a decrease in elongation at break. Upon annealing, a general enhancement in mechanical properties was obtained, with differences depending on the BM concentration. At low BM content (2.7 wt%), annealing does not lead to significant improvements in modulus and thickness, but elongation at break increases significantly, possibly related to recovery of microdefects during annealing. On the other hand, EPRgF-5.4%BM exhibit a significant enhancement in tensile strength upon annealing (approx. from 0.79 to 1.50 MPa), which appears to confirm the increase in the crosslinking density after the thermal treatment. EPRgF-8.1%BM presents similar properties compared to annealed EPRgF-5.4%BM, but its annealing leads to a limited enhancement in the modulus and a reduction in elongation. This is consistent with the unmodified crosslinking degree for EPRgF-8.1%BM after annealing (Figure 61).

To investigate the evolution of mechanical properties upon material recycling, multiple reprocessed EPRgF-5.4%BM was tested again in tensile mode (Figure 66 and Table 10).

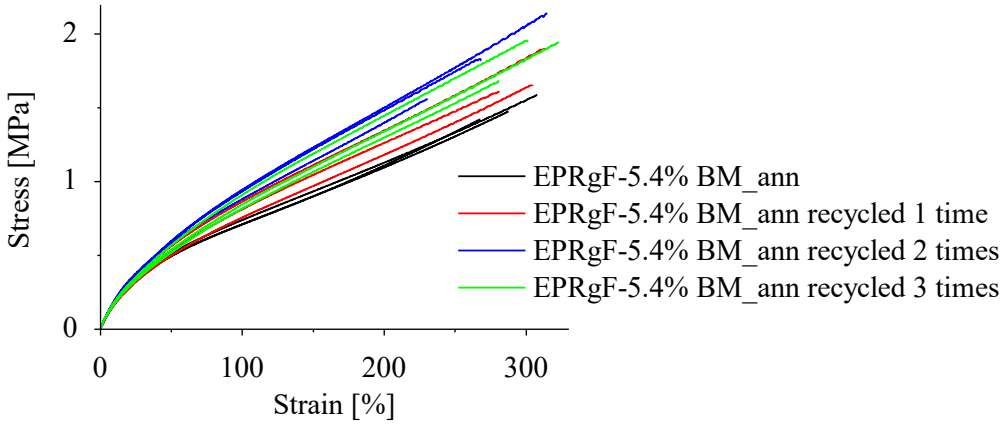


Figure 66. Stress-strain curves of EPRgF-5.4%BM_ann, reprocessed 3 times.

Table 10. Average Young's modulus E, tensile strength $\sigma_{max}$ and elongation at break $\varepsilon_b$ with their standard deviations of EPRgF-5.4%BM_ann, reprocessed 3 times.

| | **Average ± *st. dev.* of E** [MPa] | **Average ± *st. dev.* of $\sigma_{max}$** [MPa] | **Average ± *st. dev.* of $\varepsilon_b$** [%] |
|---|---|---|---|
| EPRgF-5.4%BM_ann | 1.44 ± *0.26* | 1.50 ± *0.09* | 288 ± *20* |
| EPRgF-5.4%BM_ann recycled 1 time | 1.77 ± *0.16* | 1.72 ± *0.16* | 300 ± *16* |
| EPRgF-5.4%BM_ann recycled 2 times | 1.84 ± *0.05* | 1.84 ± *0.29* | 271 ± *42* |
| EPRgF-5.4%BM_ann recycled 3 times | 1.92 ± *0.13* | 1.86 ± *0.15* | 301 ± *21* |

The results obtained evidence a progressive increase in stiffness, leading to a 1.92 ± 0.13 MPa modulus after three recycling steps, compared to 1.44 ± 0.26 MPa for pristine EPRgF-5.4%BM. Tensile strength was also slightly increased from 1.50 ± 0.09 MPa to 1.86 ± 0.15 MPa after the three recycling steps, whereas the elongation at break remain almost constant in the range of 300%.

With the aim of exploring viscoelastic properties of the rubber DMTA measures were performed, as reported in Figure 67.

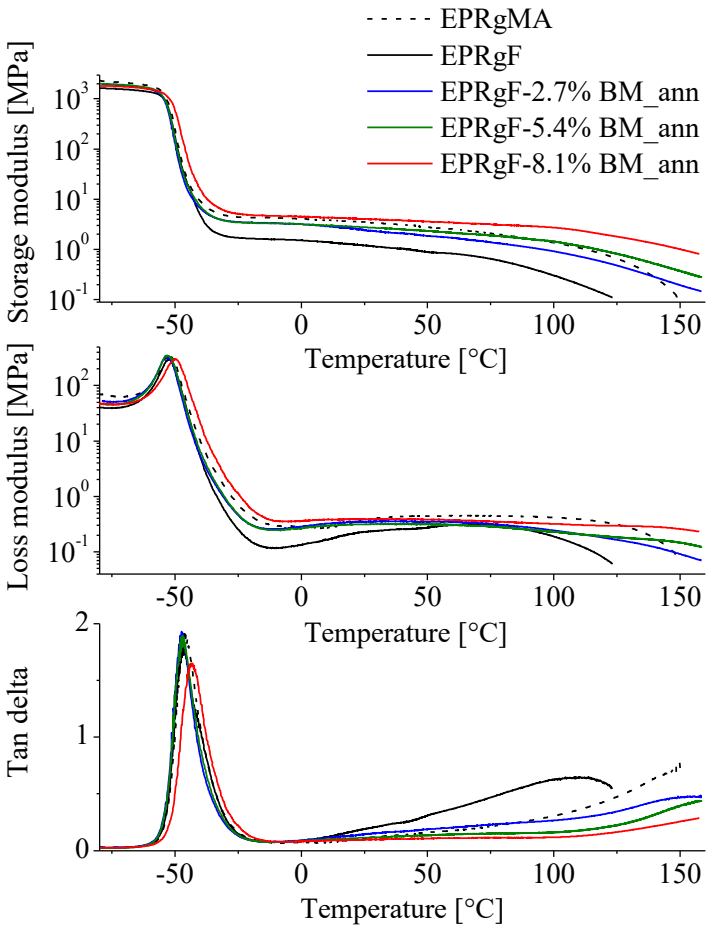


Figure 67. DMTA curves of EPRgMA, EPRgF and its BM crosslinked networks.

The glass transition of the rubbers (pristine, furan-functionalized and crosslinked) has been assessed via DMTA, the main relaxation showing a peak around -47°C, with the only exception of EPRgF-8.1%BM_ann, that presents a slight increase (-43°C). The materials do not show other transitions in the analysed temperature range, bringing evidence of their monophasic nature, consistently with SEM analysis. Starting at -20°C, the materials present a clear rubber *plateau* for both storage and loss moduli. It is worth noting that EPRgF show a decrease of the storage modulus *plateau* respect to EPRgMA (-65% at 20°C), while adding BM brings to its progressive increase (+225% at 20°C for EPRgF-8.1%BM_ann, respect to EPRgF, confirming tensile tests results) and its slower decay at higher temperatures. This behaviour is due to the bonding strength between the chains: in EPRgMA hydrogen bonds generates the *plateau* until around 100°C, then the modulus decreases rapidly. For thermoreversibly crosslinked EPRgF-BM materials, storage modulus starts to decrease around 100°C, but slower and not

dramatically as EPRgMA and EPRgF, consistently with the activation of the retro-DA equilibrium reaction.

## 3.2. Nanocomposites

### 3.2.1. Nanocomposites embedding graphene related materials

Before proceeding with nanocomposite preparation, a model reaction with a small molecule (MA, as dienophile) was used to investigate the diene nature of GNP and its possible DA reaction.

**Model reaction of maleic anhydride on graphite nanoplates**

Figure 68 reports the Diels-Alder reaction scheme between GNP and MA, as described in literature [50].

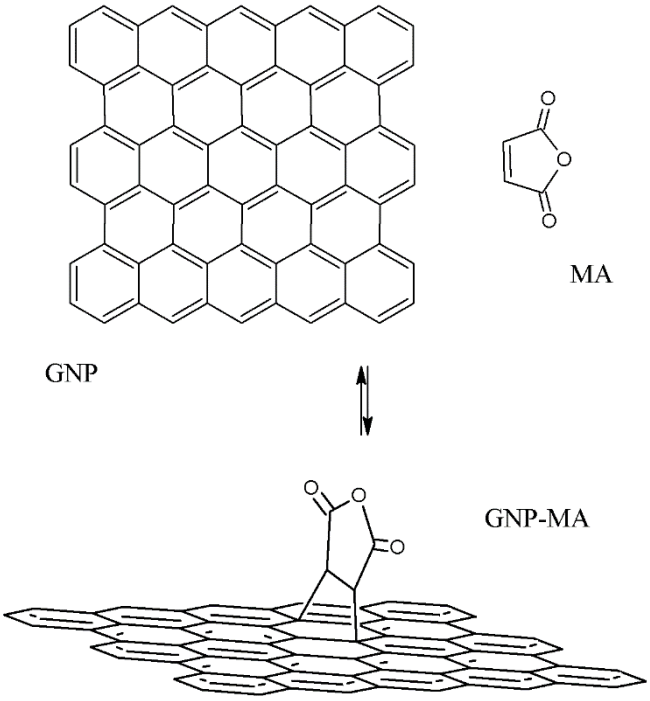


Figure 68. Diels-Alder reaction scheme between GNP plane and MA.

In order to assess the deposition of MA on GNP by solvent and vapor method, by a quantitative point of view, GNP, MA, GNP-MA_sol and GNP-MA_vap were subjected to TGA analysis (Figure 69).

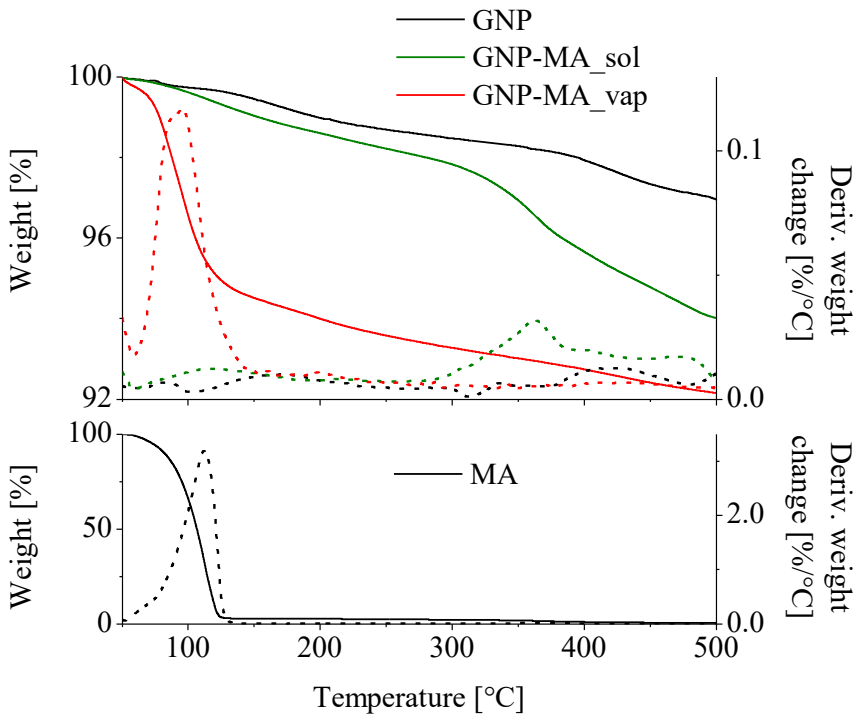


Figure 69. TGA curves of GNP, GNP-MA_sol, GNP-MA_vap (up) and MA (down), with weight loss in % and its derivative.

MA is very volatile and start to evaporate around 50°C, with a nearly complete volatilization around 130°C (Figure 69, down). GNP exhibits a very low weight loss at this temperature (0.4 wt% at 130°C), likely due to a very small fraction of absorbed water (GNP is intrinsically hydrophobic, contrary to GO, due to its low oxidation [89]). GNP then shows a small progressive weight loss until 400°C (around 2 wt%), relatable to the conversion of oxidized groups with release of small molecules [89], then starting oxidative degradation above 400°C. GNP-MA_sol exhibits a slightly higher weight loss than GNP (0.7 wt% at 130°C), suggesting a negligible MA deposition, and a secondary weight loss step around 350°C, possibly related to the volatilization of a strongly adsorbed/intercalated ODCB fraction. Regarding GNP-MA_vap, the weight loss at low temperature is remarkably higher (5.1 wt% at 130°C) and occurring at the same temperature than pristine MA suggests the presence of MA, deposited by vapor phase on GNP.

To investigate phase transitions of GNP-MA, DSC measures were performed (Figure 70).

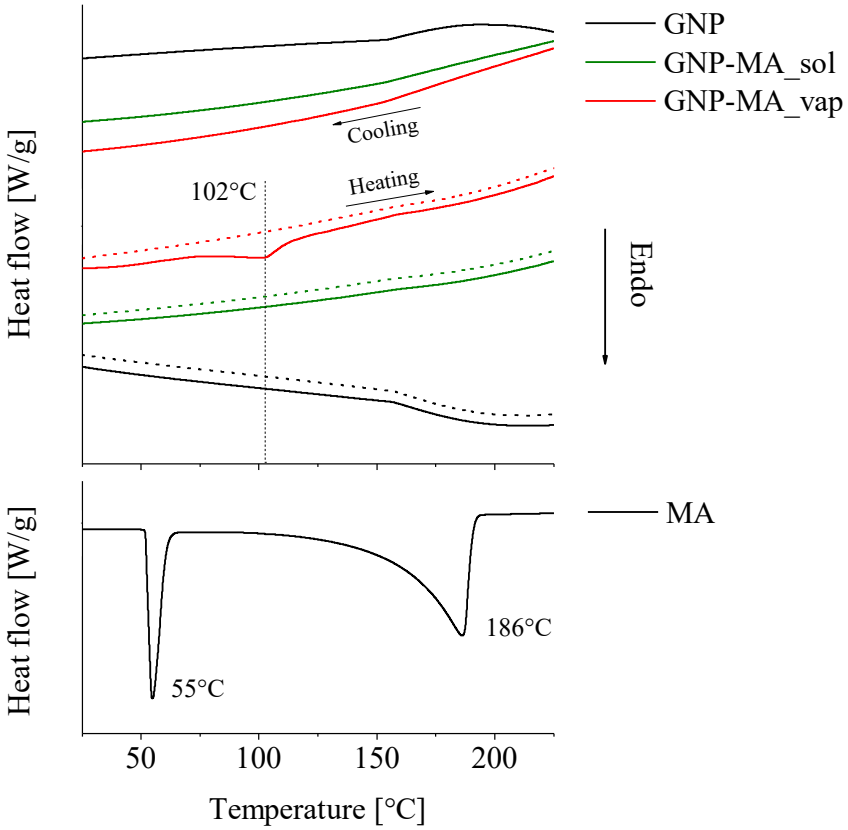


Figure 70. DSC curves of GNP, GNP-MA_sol, GNP-MA_vap (up) and MA (down). Continuous lines represent the first heating ramp and the cooling ramp, dashed lines represent the second heating ramp.

Pristine MA curve presents two endothermic signals relatable to melting and volatilization with peak temperatures at 55 and 186°C, respectively. The only clear signal in the GNP-MA curves is a small endothermic broad peak with its maximum at 102°C in GNP-MA_vap, linkable to the volatilization of MA observed in TGA, since the onset temperature for pristine MA volatilization in DSC (Figure 70, down) is around 100°C. However, no melting signal for MA is observed around 50°C in GNP-MA_vap. This is explainable by a low crystallinity of deposited MA and/or by the organization in small crystals of irregular form, generating different melting point with low intensity signals not discernible from the baseline.

In order to confirm MA presence on GNP, ATR FT-IR spectroscopy was performed. Figure 71 reports the spectra, while assignments are summarized in Table 11.

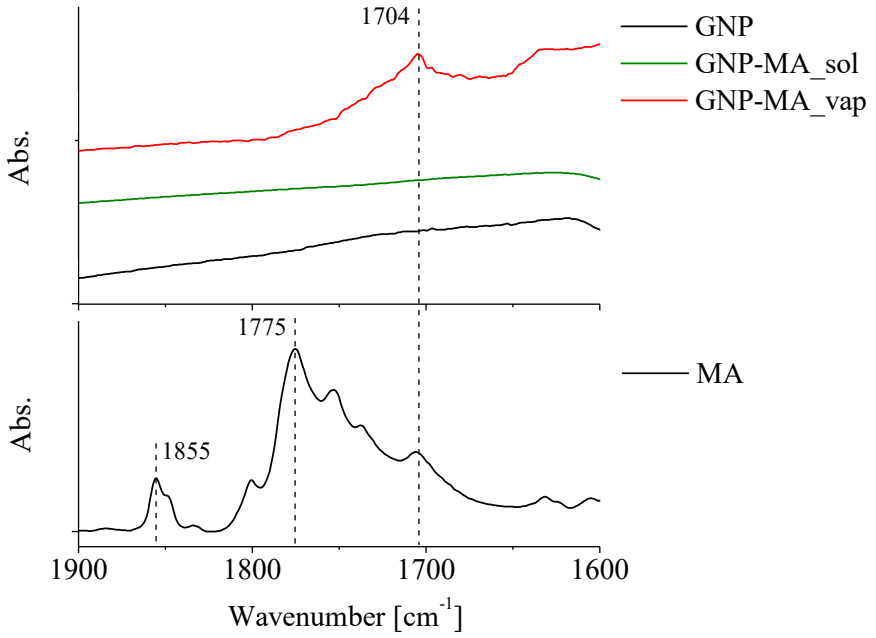


Figure 71. ATR FT-IR spectra of GNP, GNP-MA_sol, GNP-MA_vap (up) and MA (down), in the range 1900-1600 $cm^{-1}$.

Table 11. Assignments of FT-IR spectra for GNP-MA characterization.

| **Wavenumber** [$cm^{-1}$] | **Assignment** |
|---|---|
| *1855* | C=O asymmetric stretching of maleic anhydride |
| *1775* | C=O symmetric stretching of maleic anhydride |
| *1704* | C=O stretching of maleic acid |

MA spectrum in the 1900-1600 $cm^{-1}$ range (Figure 71, down) exhibits the typical couple of signals assigned to C=O stretching of maleic anhydride (1855 and 1775 $cm^{-1}$) and a signal assigned to its hydrolysed form (maleic acid, 1704 $cm^{-1}$) [78, 79]. This last MA signal appears clearly in GNP-MA_vap (Figure 71, up), indicating its presence on GNP in a mostly hydrolysed form. On the contrary, GNP-MA_sol does not show any signal relatable to MA, confirming the low deposition observed in TGA.

After evaluating the deposition of MA on GNP by a quantitative and qualitative point of view, to investigate the actual achievement of DA reaction between MA and GNP, Raman spectroscopy (Figure 72 and Table 12) and XPS (Figure 73 and Table 13) were performed.

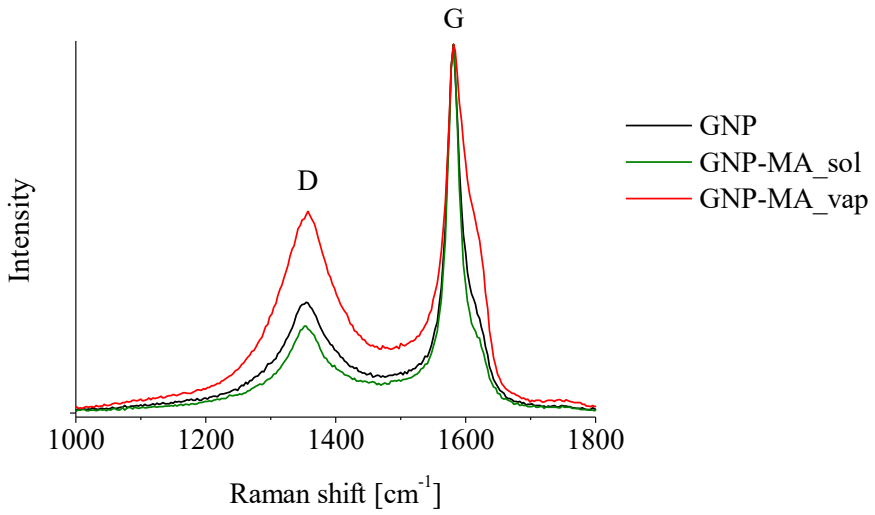


Figure 72. Raman spectra for GNP, GNP-MA_sol and GNP-MA_vap in the 1000-1800 $cm^{-1}$ range.

Table 12. Ratio between D peak and G peak intensities from Raman, for GNP, GNP-MA_sol and GNP-MA_vap.

| | $I_D/I_G$ |
|---|---|
| GNP | 0.30 |
| GNP-MA_sol | 0.24 |
| GNP-MA_vap | 0.55 |

Regarding Raman spectroscopy on GNP, it is well-known that in carbon $sp^2$ based materials the ratio between the intensity of D peak ($I_D$, due to the breathing modes of $sp^2$ atoms in rings) and the intensity of G peak ($I_G$, linked to the bond stretching of the pairs of $sp^2$ atoms in rings) is related to the density of defects, as edges and $sp^3$ sites on basal planes, which affect the vibrational mode of the $sp^2$ plane [57]. Thus, the higher is the $I_D/I_G$ ratio, the higher is the defectiveness of the GNP, intended as the presence of edges, $sp^3$ sites due to covalently grafted species/oxidation and with a lower effect also to physically absorbed species, which can also perturb the vibrational modes of the $sp^2$ plane. Since the defectiveness is also done by $sp^3$ sites on the $sp^2$ planes of GNP, the $I_D/I_G$ ratio can also be used as an indicator of the achievement of DA reaction of MA on planes [50] (see the scheme in Figure 68). This pristine GNP exhibits a $I_D/I_G$ ratio of 0.30, while in GNP-MA_sol it is slightly lower (0.24). This value suggest a cleaning effect of solvent

on GNP, with negligible presence of MA, as observed in TGA and DSC. On contrary, GNP-MA_vap shows a $I_D/I_G$ ratio of 0.55. It is possible that this almost doubling of $I_D/I_G$ ratio (also clearly visible in the spectra in Figure 72) indicates the achievement of DA reaction of MA on GNP in GNP-MA_vap. Indeed, $I_D/I_G$ ratio was already used as a diagnostic parameter for DA reaction of MA on GNP or graphite in literature [50, 59-61].

To further investigate the achievement of DA reaction between MA and $sp^2$ diene sites of GNP, XPS was performed. It is worth noting that XPS measurements are performed in high vacuum ($10^{-6}$ Pa), which is likely to remove all unbound MA, thus allowing to investigate the presence of strongly adsorbed species. In Figure 73 (a) the C1s region of XPS spectra for GNP, GNP-MA_sol and GNP-MA_vap are compared, while in Figure 73 (b), (c) and (d) the deconvolutions of these single spectra in the different contributes are reported, respectively. In Table 13 the integrated area percentages of the single contributes are reported.

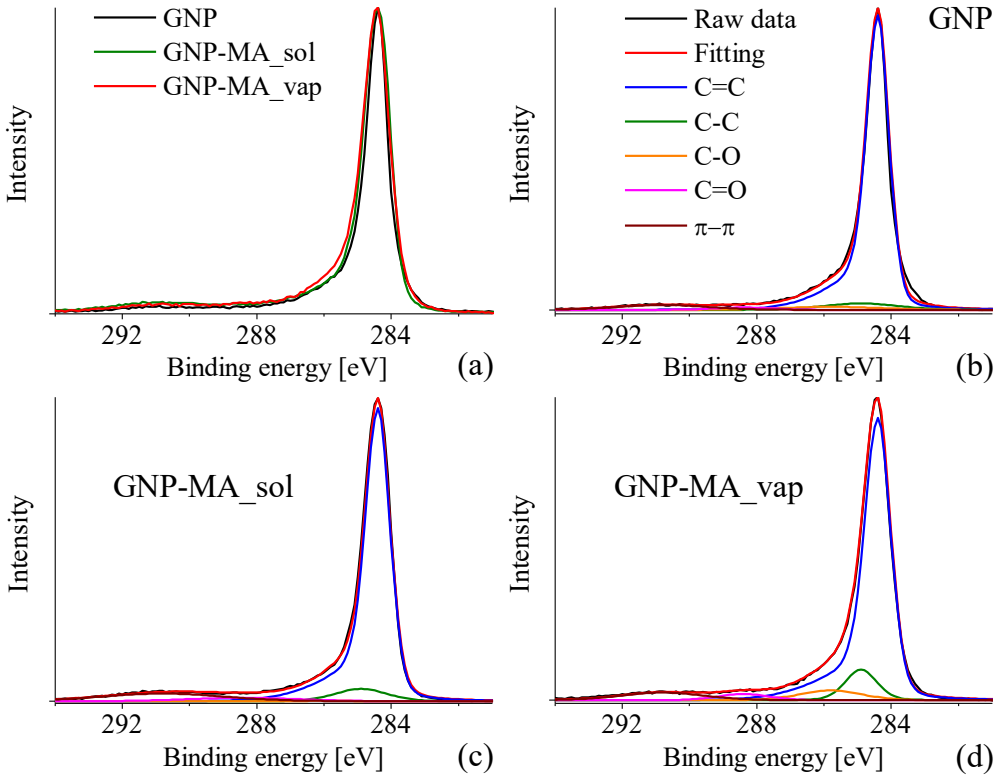


Figure 73. C1s region (294-281 eV) of XPS spectra (raw data) for GNP, GNP-MA_sol and GNP-MA_vap (a). Deconvolutions of the single spectra in the different contributes for GNP (b), GNP-MA_sol (c) and GNP-MA_vap (d).

Table 13. Integrated area percentages of the single contributes, compared to the total, for the C1s region of XPS spectra of GNP, GNP-MA_sol and GNP-MA_vap.

| | C=C *(area %)* | C-C *(area %)* | C-O *(area %)* | C=O *(area %)* | π-π *(area %)* |
|---|---|---|---|---|---|
| GNP | 84.7 | 5.3 | 3.5 | 1.6 | 4.9 |
| GNP-MA_sol | 80.6 | 6.3 | 0.8 | 3.1 | 9.2 |
| GNP-MA_vap | 77.0 | 8.8 | 5.5 | 3.0 | 5.8 |

The binding energy of the C1s electrons is affected by the chemical environment of the carbon atoms. Therefore in XPS, by fitting and deconvolution of the C1s signal, it is possible to assess the presence of different chemical environments for carbon atoms, corresponding to different binding energy shifts. Moreover, integrating the curves of contributes, it is possible to estimate their presence also by a quantitative point of view (Table 13). Relying on previous studies [71], the assignments to different carbon bonds (C=C, C-C, C-O and C=O, reported in details in Methods section with their shifts, Table 4), obtained after the deconvolution of C1s peak, indicates in GNP-MA_sol a slight increase of C-C contribute (from 5.3 at% for GNP to 6.3 at%), a drop in C-O contribute (from 3.5 at% for GNP to 0.8 at%), a similar increase than GNP-MA_vap in C=O contribute (from 1.6 at% for GNP to 3.1 at%) and a drastic increase in π-π contribute (from 4.9 at% for GNP to 9.2 at%). Especially this last contribute, assigned to π-π interactions, could indicate ODCB contaminations in GNP-MA_sol. Regarding GNP-MA_vap, an increase of C-O (from 3.5 at% for GNP to 5.5 at%) and C=O (from 1.6 at% for GNP to 3.0 at%) contributes, consistently with the presence of MA on GNP, was observed. Besides, a remarkable increase of C-C contribute from 5.3 at% of carbon atoms for GNP to 8.8 at% for GNP-MA_vap, suggest the achievement of MA grafting on GNP surface with DA reaction occurring [62] (see the reaction scheme of Figure 68).

Relying on the characterization reported in this subsection, the solvent preparation of GNP-MA_sol does not seem to be very effective, bringing negligible effects on GNP. Instead, the characterization of GNP-MA_vap brings strong evidences of effective deposition and interaction between GNP and MA, with also good indications of DA covalent grafting of MA on GNP from Raman spectroscopy and XPS.

**Nanocomposites blending**

Relying on the characterization of the interaction between GNP and a small dienophile (MA), described in the previous subsection, this behaviour can be exploited in nanocomposites, in order to enhance filler dispersion and filler-matrix interface strength in a thermoreversible nanocomposite. EPRgF-5.4%BM was chosen as the most suitable matrix as a compromise between the crosslinking degree (Figure 61) and the viscosity during extrusion. However, poor dispersion of GNP was obtained in the selected polymer matrix, owing to the strong aggregation of relatively large GNP flakes (Figure 74).

EPRgF-5.4%BM/5%GNP

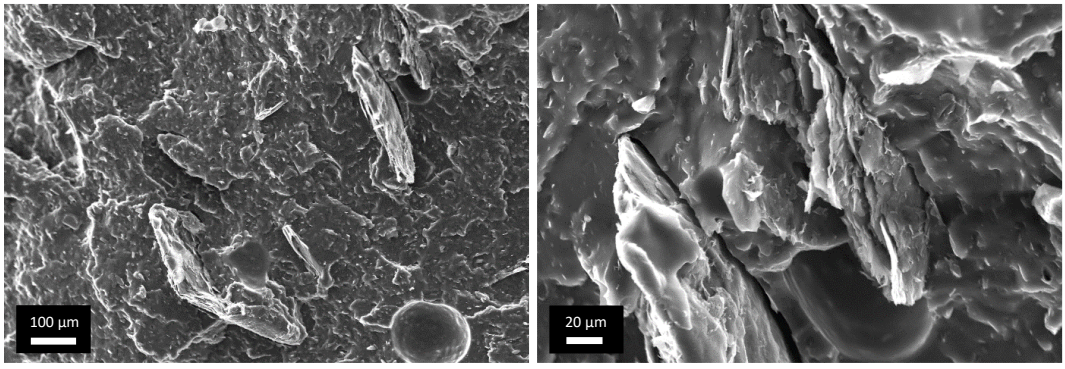


Figure 74. SEM images of EPRgF-5.4%BM/5%GNP, with evidence of large aggregations of GNP flakes.

To enhance dispersion of carbon nanoflakes, rGO was used instead of GNP. In Figure 75 SEM micrographs of the prepared nanocomposites are reported.

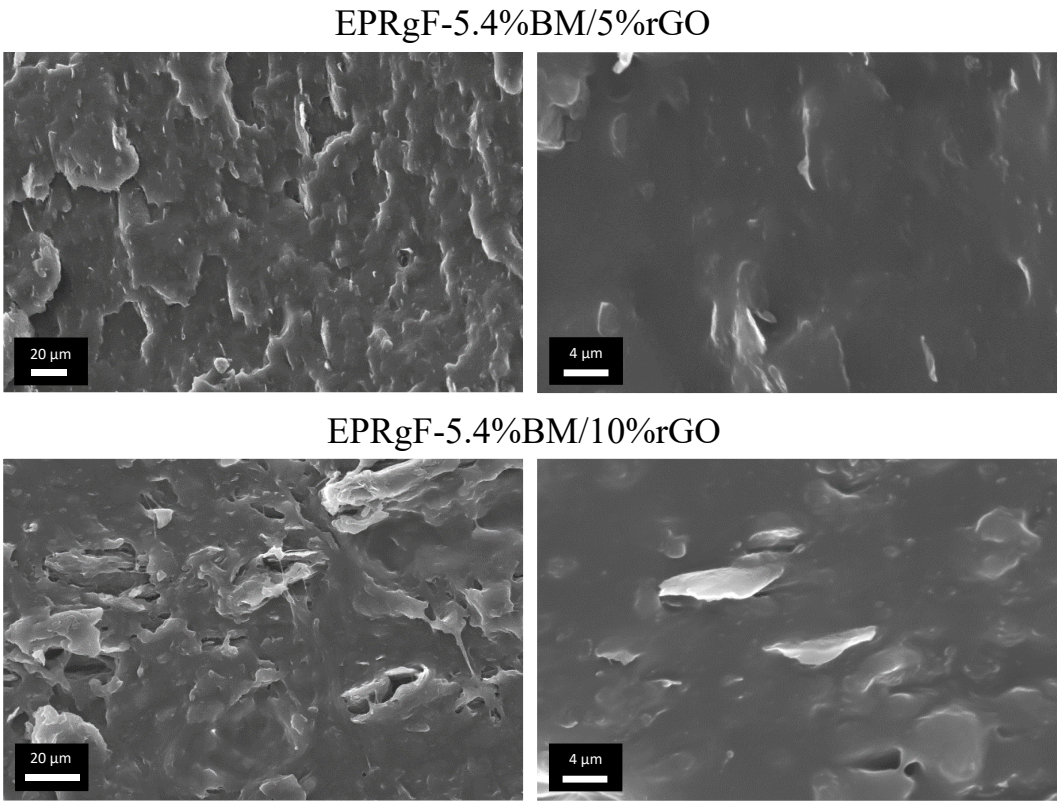


Figure 75. SEM images of EPRgF-5.4%BM/5%rGO and EPRgF-5.4%BM/10%rGO at different magnification.

SEM micrographs evidences for good distributions and dispersions of rGO at the microscale in 5 wt% composite, whereas more aggregates appear in the composite with 10 wt% rGO, probably due also to the shorter mixing time allowed before blocking of the micro-extruder. In both the composites at higher magnification, rGO *lamellae* sizing in the order of µm are clearly visible and typically oriented in the direction of flow during mixing/extrusion.

In order to check the crosslinking degree of the nanocomposites, these were subjected to solubilisation test (Figure 76).

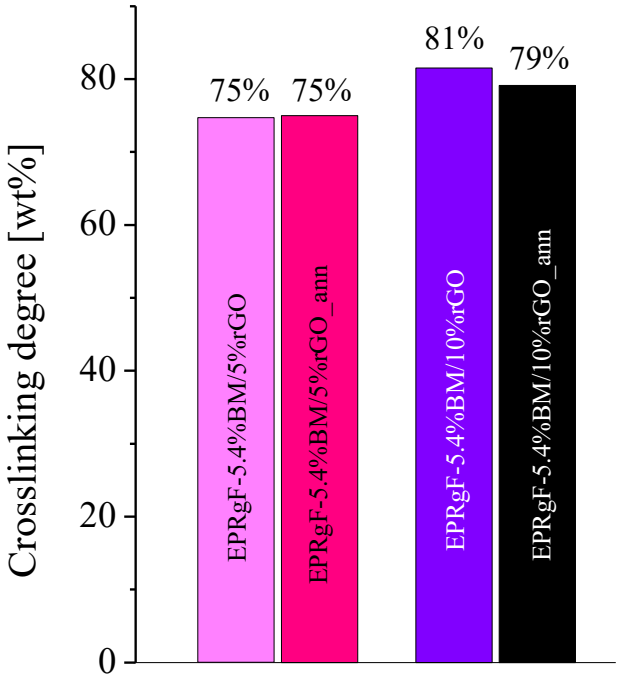


Figure 76. Percentage of remained nanocomposite after overnight soaking in toluene.

EPRgF-5.4%BM/5%rGO shows a crosslinking degree similar to EPRgF-5.4%BM, without any further contribute of annealing. Adding rGO brings a slight but noteworthy enhancement of crosslinking degree (from 75% to 81%) in EPRgF-5.4%BM/10%rGO, suggesting an active role of rGO in the covalent crosslinking of the material, through DA reaction with BM.

To further investigate rGO dispersion in the composites, rheology was addressed (Figure 77). Indeed, rheology provides information on the organization of nanoflakes in the bulk, complementing local analyses obtained by SEM [90].

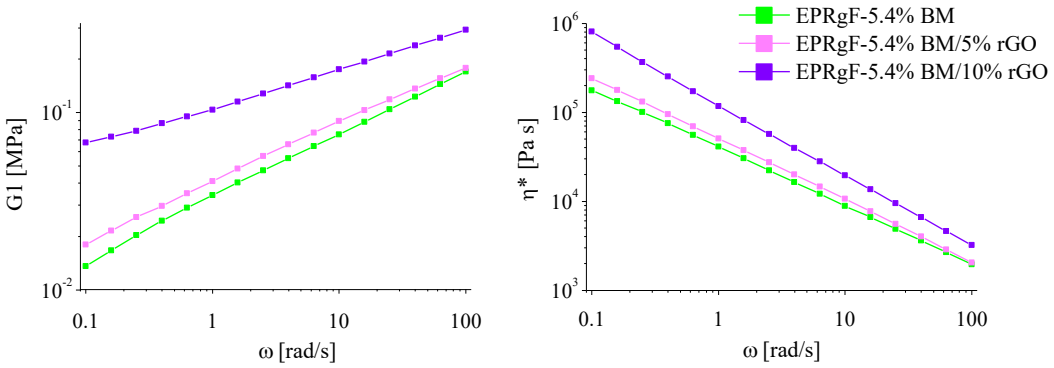


Figure 77. Storage modulus (G´) and complex viscosity (η*) in function of angular frequency (ω), for EPRgF-5.4%BM and its nanocomposites.

Addition of 5%rGO to EPRgF-5.4%BM brings limited increase to G´ and η* plots, whereas much higher effects are observed when adding 10%rGO. Indeed, EPRgF-5.4%BM/10%rGO exhibits a lower slope of G´ at low angular frequencies, which may be explained by the physical percolation of rGO, in addition to the interactions between BM-bound EPRgF chains. The presence of an effect of physical percolation is an indicator of a good distribution of rGO in the matrix [90], as observed by SEM in EPRgF-5.4%BM/5%rGO (Figure 75) and bringing evidence of better dispersion than the SEM-observed one for EPRgF-5.4%BM/10%rGO.

Mechanical properties of the nanocomposites were investigated by tensile test in the same conditions of the corresponding EPRgF-BM. The stress-strain curves are shown in Figure 78 and the corresponding average Young's modulus (E), tensile strength ($\sigma_{max}$) and elongation at break ($\varepsilon_b$) are reported in Table 14, with their standard deviations.

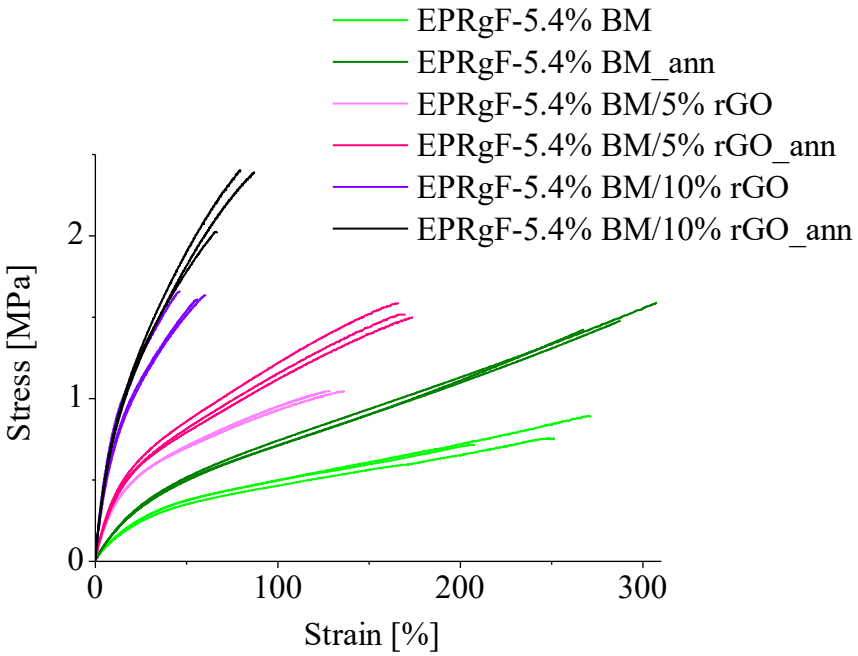


Figure 78. Stress-strain curves of crosslinked rubber - rGO composites.

Table 14. Average Young's modulus E, tensile strength $\sigma_{max}$ and elongation at break $\varepsilon_b$ with their standard deviations of EPRgF-5.4%BM and its nanocomposites.

| | **Average ± *st. dev.* of E** [MPa] | **Average ± *st. dev.* of $\sigma_{max}$** [MPa] | **Average ± *st. dev.* of $\varepsilon_b$** [%] |
|---|---|---|---|
| EPRgF-5.4%BM | 1.38 ± *0.10* | 0.79 ± *0.09* | 244 ± *33* |
| EPRgF-5.4%BM_ann | 1.44 ± *0.26* | 1.50 ± *0.09* | 288 ± *20* |
| EPRgF-5.4%BM/5%rGO | 3.91 ± *0.30* | 1.04 ± *0.02* | 129 ± *8* |
| EPRgF-5.4%BM/5%rGO_ann | 4.16 ± *0.08* | 1.53 ± *0.04* | 170 ± *4* |
| EPRgF-5.4%BM/10%rGO | 8.30 ± *1.07* | 1.64 ± *0.03* | 55 ± *7* |
| EPRgF-5.4%BM/10%rGO_ann | 8.14 ± *1.78* | 2.27 ± *0.21* | 78 ± *10* |

In nanocomposites, the inclusion of rGO determines a remarkable increase in stiffness (+189% at 5%rGO and +465% at 10%rGO) and tensile strength ($\sigma_{max}$ +51% at 10%rGO), comparing the annealed samples of nanocomposites and reference matrix, at the expense of a strong decrease in elongation at break (i.e. about one fourth at 10%rGO). The effect of annealing is similar to that observed in

the matrix, bringing an enhancement in tensile strength (+38% for EPRgF-5.4%BM/10%rGO) and elongation at break without notable effects on stiffness. Only a few papers reported mechanical properties of nanocomposites in DA crosslinked matrices. Jia *et al* [68] reported crosslinking of EPRgF on dienophile-functionalized silica, leading to a 2.5 MPa tensile strength and 800% fracture strain, when adding 13 wt% functionalized silica. Polgar *et al* reported BM-crosslinked EPRgF filled with carbon nanotubes (CNT) [53], yielding significantly higher tensile strength (7 MPa) with 10 wt% of CNT, together with an 80% elongation at break. Results obtained in this work using rGO are comparable to the previous reports: for instance, EPRgF-5.4%BM/10%rGO_ann has a 2.3 ± *0.2* MPa tensile strength with approx. 80% fracture strain, which appears competitive with previously reported nanocomposites, especially when considering the materials in this work were obtained by melt processing instead of the conventional solvent mixing.

In order to investigate the thermal conductivity of the composites, TPS measures were performed on the different formulations.

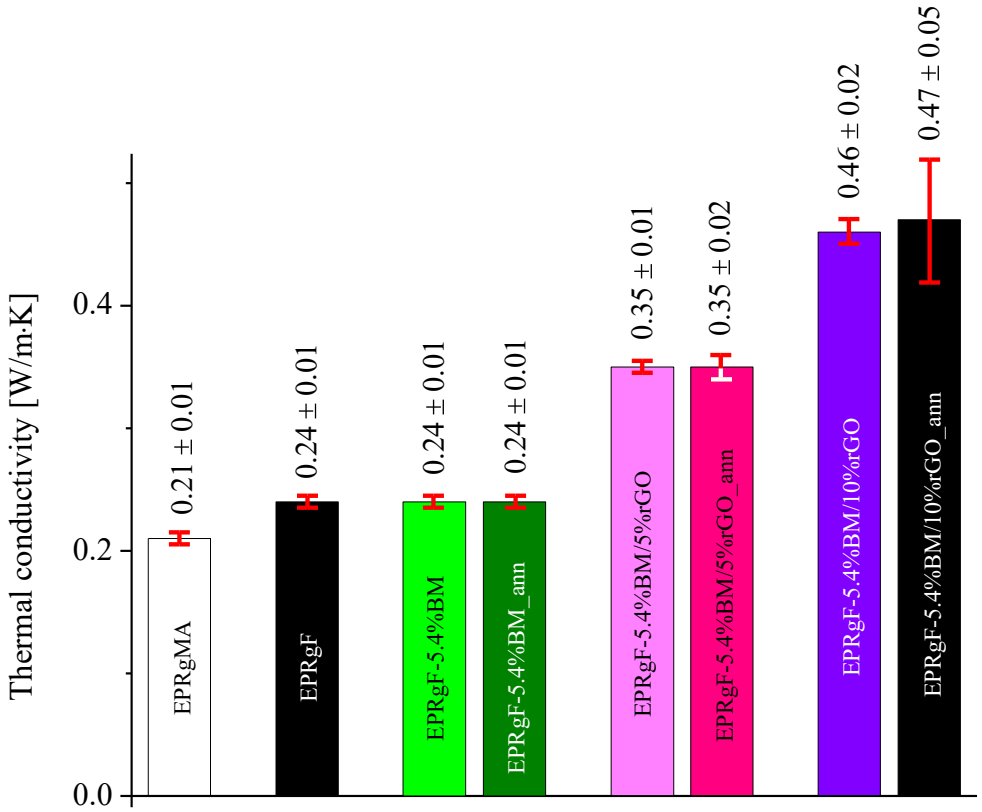


Figure 79. Thermal conductivity values of rubbers and rGO composites with their standard deviation (red bar).

The thermal conductivity of pristine EPRgMA (0.21±0.01 W/m·K) is almost unmodified by the furan grafting and crosslinking, yielding 0.24±0.01 for EPRgF and EPrgF-5.4%BM. On the other hand, addition of rGO gives to the rubber a clear enhancement of thermal conductivity, that rise to 0.35±0.02 W/m·K (+70%) with 5 wt% rGO and 0.47±0.05 W/m·K (+124%) with 10 wt% rGO, compared to the pristine rubber, with no significant effect of thermal annealing. Thermal conductivity obtained in this work is higher than reported in rubbers filled with other conductive particles: in particular, hexagonal boron nitride (14 wt%, particles of 2-3 μm) in siloxane rubber yielded 0.4 W/m·K [91] whereas expanded graphite (9 wt%, particles ca. 300 μm) in silicone rubber exhibited a 0.25 W/m·K conductivity [92]. Therefore, inclusion of rGO appears as a promising strategy to enhance rubber thermal conductivity keeping the filling percentage low. This is in fact required in application where high flexibility and deformability to high strain is required, such as in modern flexible electronics [93], including next generations of wearable and implantable devices [94, 95].

**Press&Fold method**

The problems faced with viscosity via standard processing via extrusion pushed to try Press&Fold method as an alternative processing way to increase rGO content in the nanocomposite. Two samples of EPRgF and EPRgF-5.4%BM were prepared with P&F method at 20 and 50 cycles, to study the effect of multiple hot-pressing step on the rubber. The process generates films with an irregular and rough surface, as shown in Figure 80, in EPRgF and even more in EPRgF-5.4%BM, suggesting occurring of undesired irreversible crosslinking and difficulty in re-molding of the films.

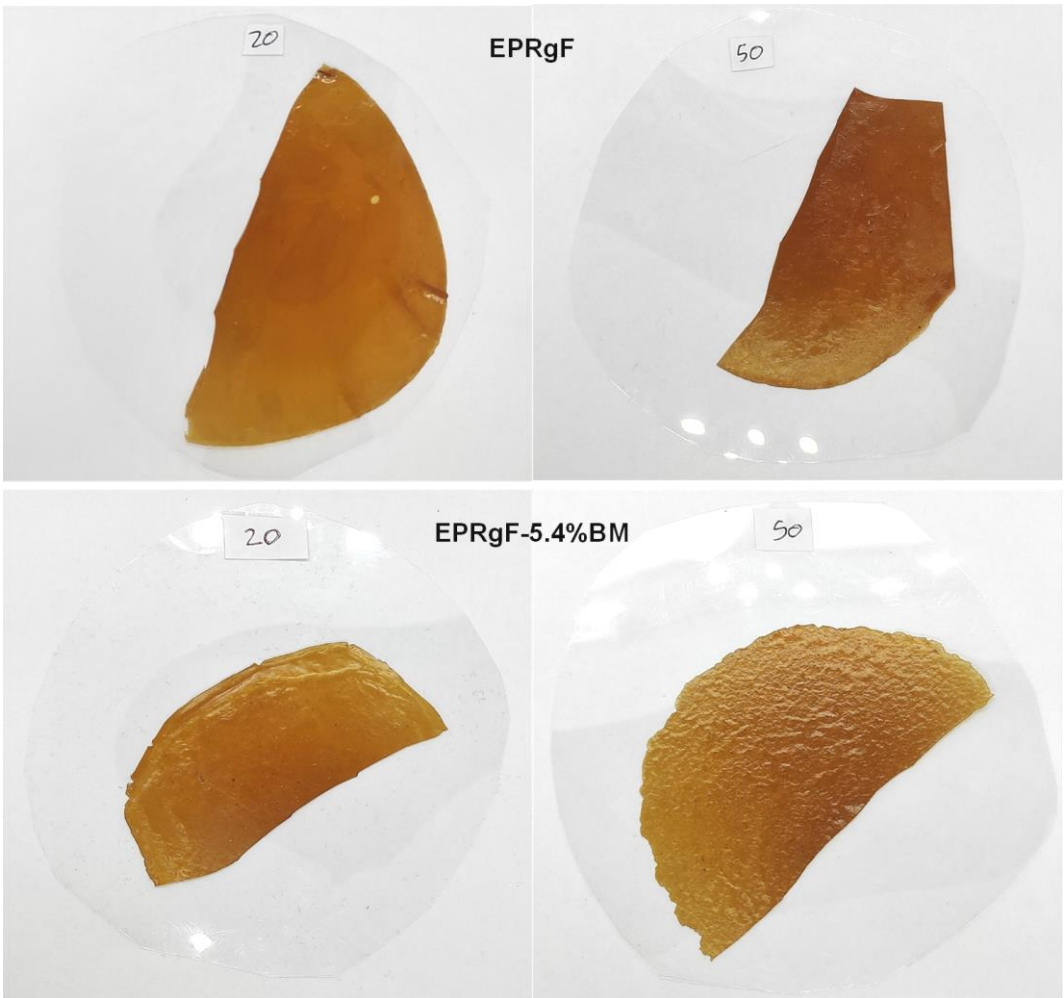


Figure 80. Picture of EPRgF_20P&F (up, left), EPRgF_50P&F (up, right), EPRgF-5.4%BM_20P&F (down, left) and EPRgF-5.4%BM_50P&F films (down, right).

In Figure 81 stress-strain curves from tensile test for EPRgF-5.4%BM prepared via melt blending (for reference) and the two EPRgF-5.4%BM samples prepared via P&F are reported, while mechanical properties are showed in Table 15.

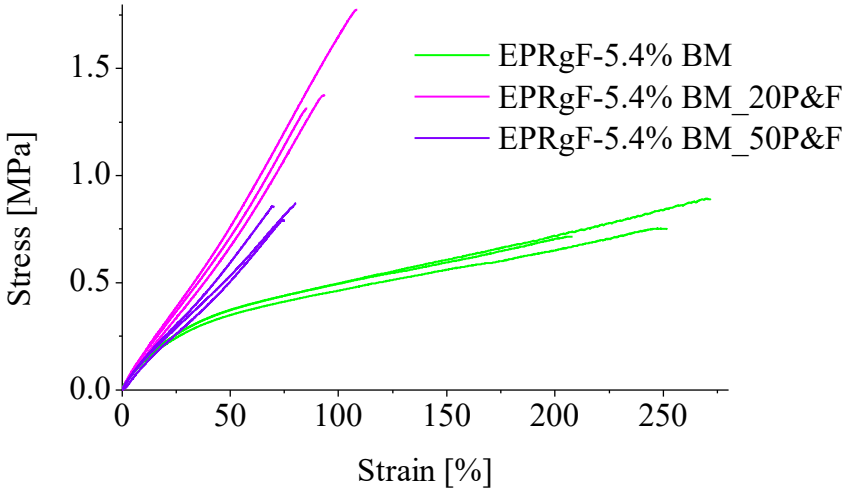


Figure 81. Stress-strain curves of EPRgF-5.4%BM prepared via melt blending and via P&F method.

Table 15. Average Young's modulus E, tensile strength $\sigma_{max}$ and elongation at break $\varepsilon_b$ with their standard deviations of EPRgF-5.4%BM prepared via melt blending and via P&F method.

| | **Average ± *st. dev.* of E** [MPa] | **Average ± *st. dev.* of $\sigma_{max}$** [MPa] | **Average ± *st. dev.* of $\varepsilon_b$** [%] |
|---|---|---|---|
| EPRgF-5.4%BM | 1.38 ± *0.10* | 0.79 ± *0.09* | 244 ± *33* |
| EPRgF-5.4%BM_20P&F | 0.98 ± *0.34* | 1.48 ± *0.25* | 96 ± *12* |
| EPRgF-5.4%BM_50P&F | 0.76 ± *0.50* | 0.84 ± *0.04* | 75 ± *5* |

The results of tensile testing point out a clear change in the mechanical behaviour of the material, with a drop in stiffness (from 1.38 to 0.76 MPa at 50 P&F cycles) and elongation at break (from 244 to 75 %). Regarding EPRgF-5.4%BM_20P&F, it presents a higher tensile strength than the melt blended one (1.48 *vs* 0.79 MPa), but the trend, going to 50 P&F cycles, is decreasing (0.84 MPa). This behaviour could be consistent with an undesired further crosslinking of the material, subjected to multiple hot-pressing steps. Indeed, as reported in the state of the art, although DA adduct are chosen as the most stable and reversible option

among the addition reactions suitable for dissociative CANs [18], furan rings were already reported as possibly subjected to ring-opening (via oxidation [28] or hydrolysis [29]) and undesired irreversible crosslinking, via inter-chain condensation [27]. Moreover, another source of matrix degradation might be bismaleimide homopolymerization, as previously reported in literature [96], and the intensification of the film degradation in the presence of BM (Figure 80) suggests a potential role of BM. FT-IR spectroscopy measures were performed (Figure 82), in order to check for possible variations in the furan zone, previously used in EPRgF characterization, but no notable differences were detected here or in other zones of the spectra. However, FT-IR signal might not be sensible enough to detect the ring-opening and irreversible crosslinking of a small fraction of groups, sufficient to compromise the reprocessability step by step in P&F process. Regarding BM homopolymerization, its possible occurrence in EPRgF-5.4%BM is likely undetectable, due to the lack of diagnostic signals.

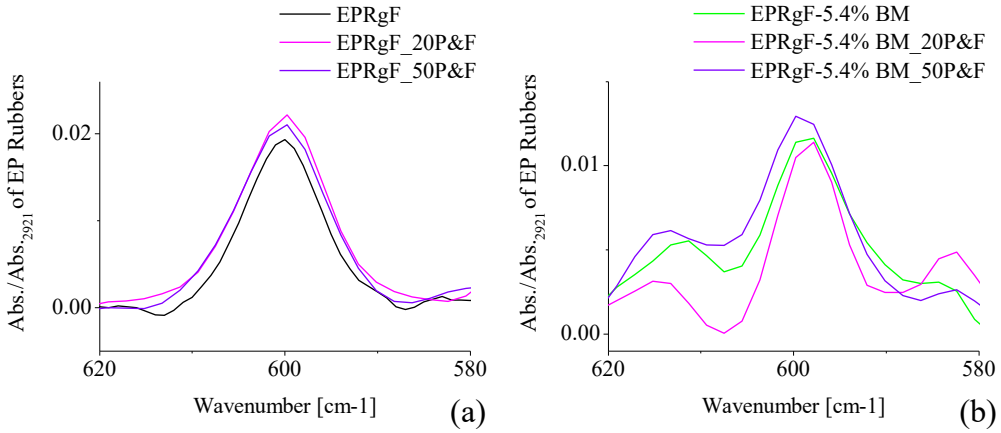


Figure 82. ATR FT-IR spectra, relating to EPRgF (a) and EPRgF-5.4%BM (b) subjected to 20 and 50 P&F cycles, in the range 620-580 $cm^{-1}$ (spectra are normalized on their higher peak at 2921 $cm^{-1}$, assigned to C-H stretching vibration on the aliphatic chain of the rubbers).

Although this rubber matrix does not seem fully stable for this alternative processing method after these preliminary test, some samples at different P&F cycles were prepared with 10%rGO and subjected to SEM characterization and tensile testing. SEM characterization (Figure 83) shows rGO aggregation in the range of 100 µm, likely due to the low number of P&F cycles performed (40), in order to avoid matrix degradation. In Figure 84 the stress-strain curves, together with the ones for EPRgF-5.4%BM and EPRgF-5.4%BM/10%rGO previously prepared via melt blending, are reported, while mechanical properties are listed in Table 16.

EPRgF-5.4%BM/10%rGO_20P&F

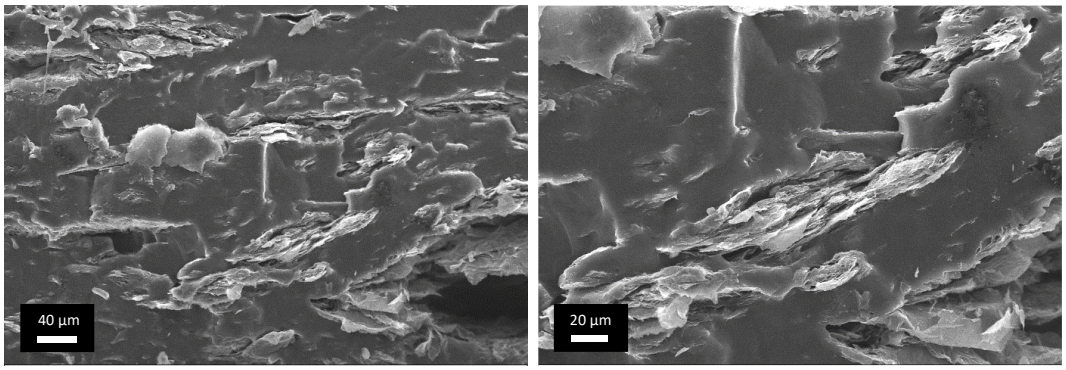


EPRgF-5.4%BM/10%rGO_30P&F

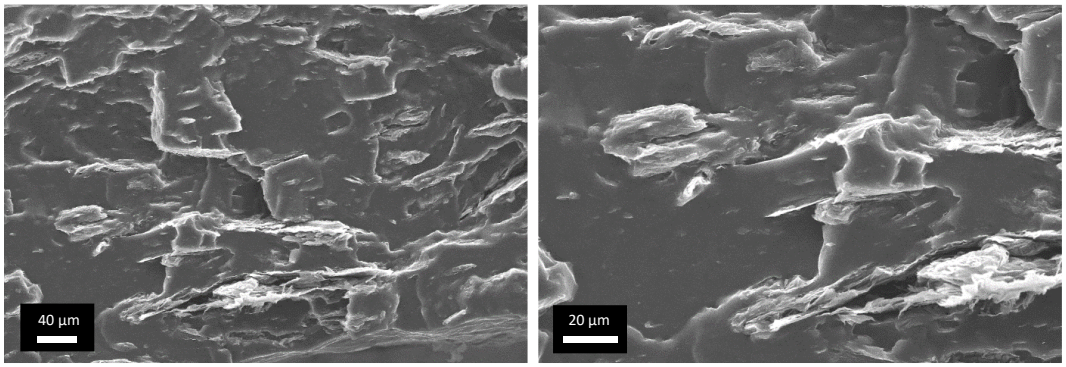


EPRgF-5.4%BM/10%rGO_40P&F

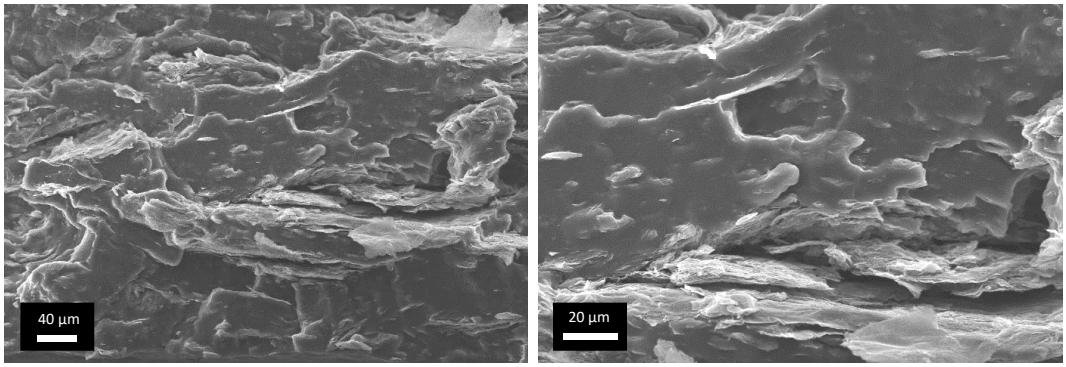


Figure 83. SEM images of EPRgF-5.4%BM/10%rGO prepared with P&F method after 20, 30 and 40 P&F cycles, at different magnifications.

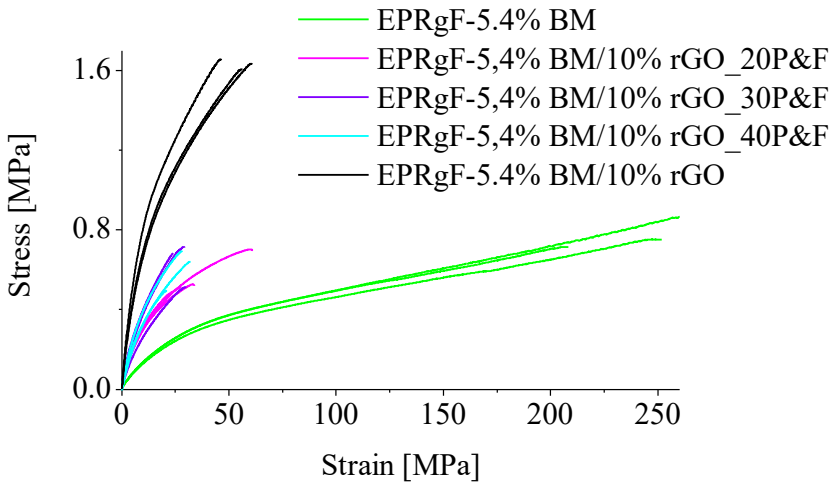


Figure 84. Stress-strain curves of EPRgF-5.4%BM and EPRgF-5.4%BM/10%rGO, prepared via melt blending, and the composites prepared via P&F method.

Table 16. Average Young's modulus E, tensile strength $\sigma_{max}$ and elongation at break $\varepsilon_b$ with their standard deviations of EPRgF-5.4%BM and EPRgF-5.4%BM/10%rGO, prepared via melt blending, and the composites prepared via P&F method.

| | **Average ± *st. dev.* of E** [MPa] | **Average ± *st. dev.* of $\sigma_{max}$** [MPa] | **Average ± *st. dev.* of $\varepsilon_b$** [%] |
|---|---|---|---|
| EPRgF-5.4%BM | 1.38 ± *0.10* | 0.79 ± *0.09* | 244 ± *33* |
| EPRgF-5.4%BM/10%rGO _20P&F | 3.81 ± *1.38* | 0.58 ± *0.10* | 41 ± *17* |
| EPRgF-5.4%BM/10%rGO _30P&F | 3.42 ± *1.29* | 0.63 ± *0.11* | 28 ± *3* |
| EPRgF-5.4%BM/10%rGO _40P&F | 3.84 ± *0.36* | 0.61 ± *0.10* | 27 ± *6* |
| EPRgF-5.4%BM/10%rGO | 8.30 ± *1.07* | 1.64 ± *0.03* | 55 ± *7* |

The attempt to prepare the 10 wt% rGO composite via P&F method is clearly unsuccessful regarding the mechanical performances. Indeed, after 40 P&F cycles the tensile strength is not improved but slightly decreased (0.61 *vs* 0.79 MPa of EPRgF-5.4%BM prepared via melt blending), contrary to EPRgF-5.4%BM/10%rGO, prepared via melt blending (1.64 MPa). Stiffness is improved (3.84 MPa for EPRgF-5.4%BM/10%rGO_40P&F) but remarkably lower than EPRgF-5.4%BM/10%rGO prepared via melt blending (8.30 MPa). This behaviour is likely due to the matrix degradation, as observed in the preliminary tests on

EPRgF-5.4%BM, and to the poor dispersion of rGO after few cycles (the number of P&F cycles necessary to obtain a good filler dispersion is remarkably higher, typically > 100 [76]). Therefore, the impossibility to reach higher number of P&F cycles due to the matrix degradation is a limit to prepare a nanocomposite with a satisfying filler dispersion.

## 3.2.2. Silica nanocomposites

### Silica functionalization with dienophile groups

The scheme of the amorphous silica functionalization[1] with 1-[3-(Triethoxysilyl)propyl]-1H-pyrrole-2,5-dione is reported in Figure 85.

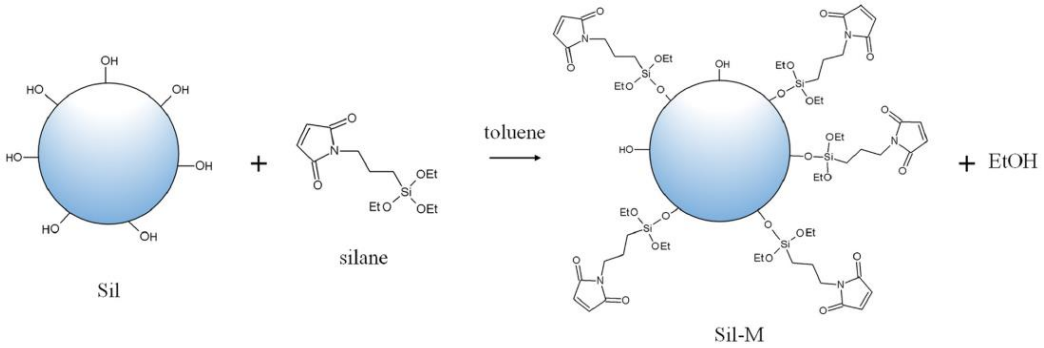


Figure 85. Scheme of Sil-M preparation.

The functionalization was qualitatively monitored by infrared spectroscopy. The spectrum of the inorganic Sil at room temperature and under vacuum conditions in the 4000-1400 $cm^{-1}$ range, is composed by some bands typical of the siliceous matrices. In particular, a sharp peak at 3750 $cm^{-1}$, followed by a wide component centred at *ca.* 3500 $cm^{-1}$ are assigned to the stretching modes of isolated and hydrogen-bonded silanols, respectively, exposed on the surface (Figure 86). After reaction with the silane, an evident erosion of the peak at 3750 $cm^{-1}$ was detected, as a consequence of the reaction of the Si-OH groups with the silane reactant. Furthermore, a new peak at ca. 1700 $cm^{-1}$ appears and it is attributed to the stretching modes of the N-C=O groups of the maleimide functionality (Figure 86). The presence of this component confirms the integrity of the molecule during the anchoring reaction on the silica surface. Additional less intense peaks in the

[1] Functionalization of silica was carried out by Prof. Fabio Carniato at the University of Eastern Piedmont, being a research partner in this work.

3100-2900 $cm^{-1}$ range are attributed to the stretching modes of CH and $CH_2$ groups of the organic component.

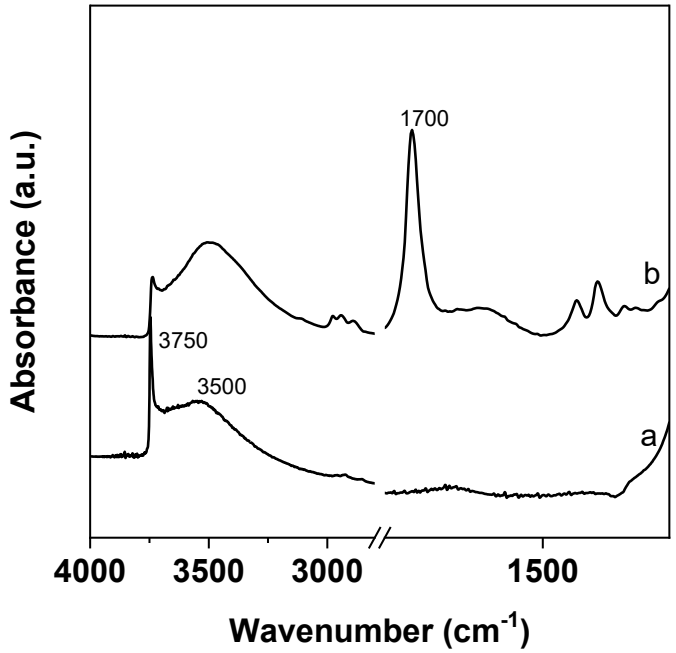


Figure 86. FT-IR spectrum of Sil (a) and Sil-M (b) samples in the 4000-1400 $cm^{-1}$ range.

The presence of the 1-[3-(Triethoxysilyl)propyl]-1H-pyrrole-2,5-dione on the silica surface was also quantified by CHN elemental analysis, evidencing that 1.01 mmol of silane on grams of Sil-M (corresponding to 30 wt%) are indeed reacted with the surface silanol groups.

**Nanocomposite blending**

In order to enhance stiffness and tensile strength of the rubber, Sil-M was added to EPRgF to prepare an extrudable and thermoreversibly crosslinked composite rubbers. Two composites were prepared adding only Sil-M (10 and 20 wt%) and one adding Sil-M (10 wt%) together with BM (2.7 wt% of the content of EPRgF), as a further medium of crosslinking. Reference composites were also prepared with Sil (7 and 14 wt%) and Sil (7 wt%) together with BM (2.7 wt% of the content of EPRgF). Figure 87 reports a scheme of Sil-M and BM crosslinking mechanisms.

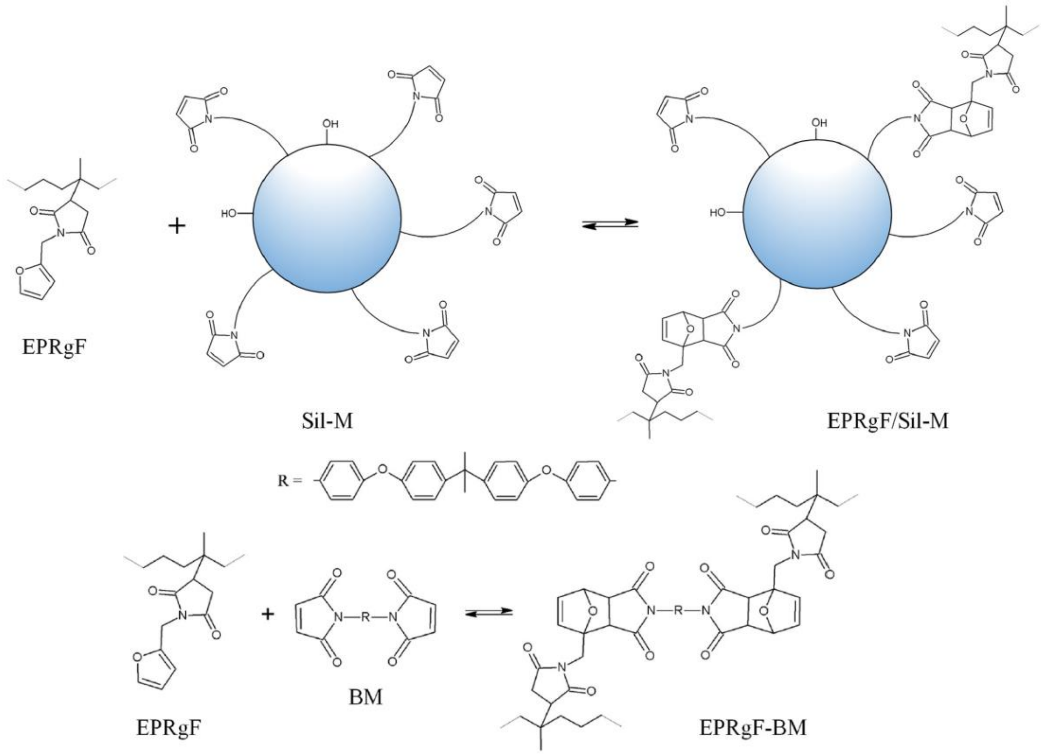


Figure 87. Scheme of crosslinking of EPRgF with Sil-M (up) and BM (down).

In order to investigate the filler dispersion in the matrix, SEM micrographs were taken, reported in Figure 88 for every composite at the same magnification.

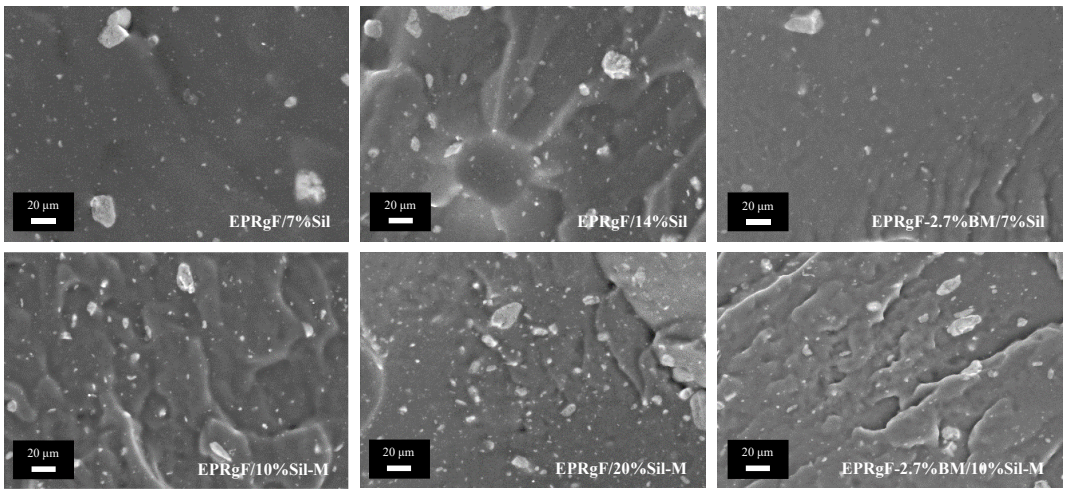


Figure 88. SEM images of the composites at the same magnification.

All the micrographs show the presence in the composites of some silica agglomerates in the range of 20 µm, likely due to the non-optimized extrusion process, as well as many smaller aggregates in the range of few microns or less,

well distributed in the polymer matrix. To further investigate the filler dispersion in the composites and the rubber properties at processing temperature, rheology measures were carried out (Figure 89).

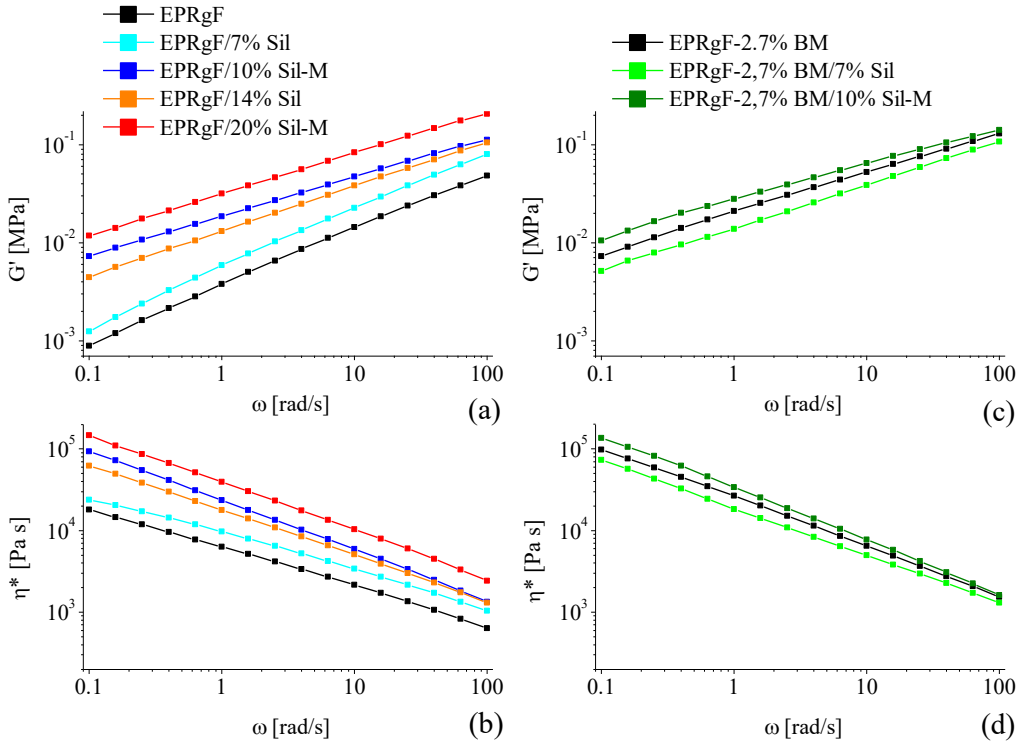


Figure 89. Storage modulus (G') and complex viscosity (η*) as a function of angular frequency (ω) for EPRgF/Sil-M (a,b) and EPRgF-2.7%BM/Sil-M (c,d).

While the inclusion of inorganic particles is expected to increase storage modulus (*G'*) and complex viscosity ($\eta^*$) curves (Figure 89 a, b), significant differences were observed in rheological plots between Sil and Sil-M. Indeed, increase in *G'* and $\eta^*$ is systematically higher for Sil-M compared to Sil at the same content of inorganic particles. Furthermore, slopes in *G'* plot at low frequency are also significantly changed, depending on the type and concentration of silica, compared to the reference polymer. For instance, while 7% Sil has minor effect on the slope of *G'* in the low frequency region, 10% Sil-M (corresponding to the same inorganic content given the organic functionalization) exhibits a lower slope in *G'*. This is well known to correlate with restriction in the flow of polymer chains, which may occur in the presence of a percolate network of nanofillers [90] or by physical/chemical crosslinking of the polymer chains [97]. Given the moderate concentration of silica and its imperfect dispersion, the rheological measurements support the capability of Sil-M to act as a crosslinking agent, by the formation of DA adducts between furan groups grafted on EPR and maleimide groups onto Sil-

M. Indeed, while the retro Diels Alder reaction is expected to occur above 110°C [20], it was previously reported that the full dissociation of DA bonds in the molten state is not possible at 150°C, owing to the equilibrium of the reaction and the high concentration of reactive moieties in the melt [87]. At the higher silica content, differences between Sil and Sil-M are less remarkable in terms of *G'* slope, suggesting that the interactions between silica particles represent the main contribution to the rheological behaviour at low frequency, with additional chemical crosslinking via DA causing an increase in the *G'* plot, without changing its slope. In BM-containing rubbers (Figure 89 c, d), adding 7 wt% Sil and 10 wt% Sil-M causes a limited increase in *G'* and $\eta^*$ curves. Indeed, EPRgF-2.7%BM rheological plots exhibit features typical of a weakly crosslinked network, owing to the DA reaction, and the inclusion of Sil and Sil-M simply increase the viscosity and storage modulus, as a consequence of additional chain movement restriction by the presence of dispersed particles (both Sil and Sil-M) and the increase in crosslinking density (Sil-M only).

In order to investigate the actual crosslinking efficiency in the different solutions adopted, the crosslinking degree was calculated through solubility tests (Figure 90).

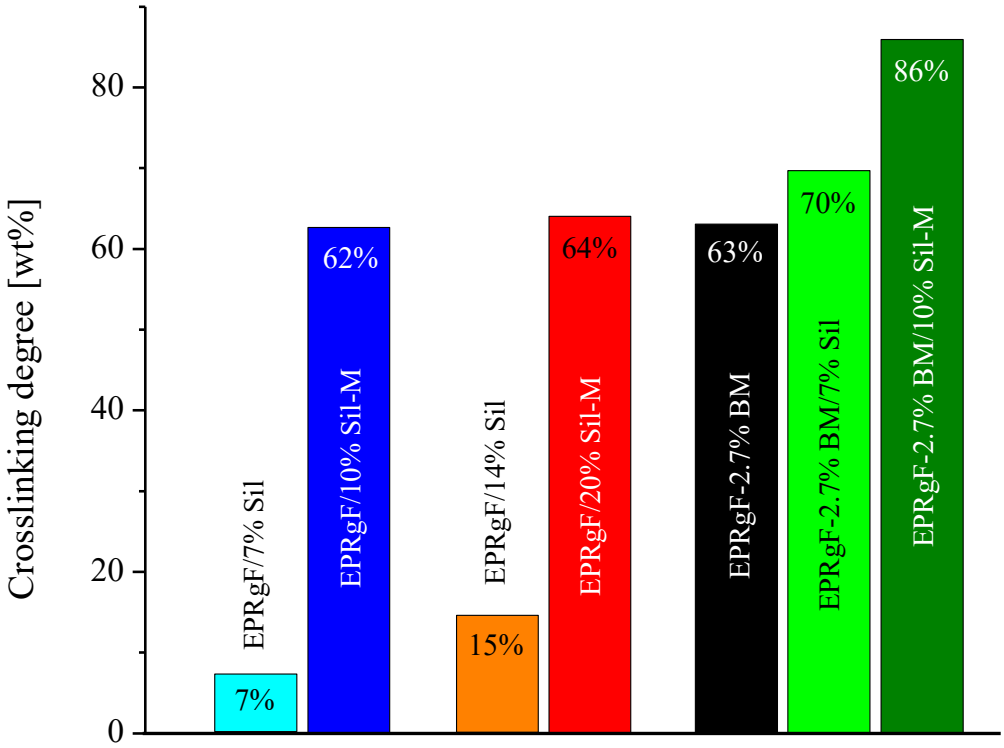


Figure 90. Crosslinking degrees obtained by solubilisation tests.

EPRgF is fully soluble in toluene, and inclusion of pristine silica is not expected to significantly affect its solubility. However, a limited insoluble fraction was surprisingly observed (7% for EPRgF/7%Sil and 15% for EPRgF/14%Sil), which may be explained by adsorption of EPRgF onto Sil, possibly via the formation of hydrogen bonds. On the other hand, the inclusion of Sil-M caused dramatic increase in the crosslinking degree, namely 62% and 64% for EPRgF/10%Sil-M and EPRgF/20%Sil-M, respectively. The small difference in crosslinking degree when doubling the Sil-M content suggests that the higher silica fraction cannot be exploited in the DA reaction because of the limitation in the dispersibility of Sil-M. Attempting to increase the crosslinking degree, BM was included in some additional formulations, to complement Sil-M in the DA reaction with furan groups that could not react onto Sil-M. The crosslinking degree of EPRgF-2.7%BM, taken as reference DA rubber, is 63%, which is approx. corresponding to the insoluble fractions in EPRgF/10%Sil-M and EPRgF/20%Sil-M. The combination of Sil-M and BM as crosslinking media yields considerably higher crosslinking degrees, namely 86% for EPRgF-2.7%BM/10%Sil-M, whereas inclusion of Sil leads to about 7% increase in the crosslinking degree, which is consistent to the increase observed in EPRgF and discussed above.

Tensile tests were carried out on the composites in order to investigate the reinforcement obtained. The resulting stress-strain curves are reported in Figure 91, together with the corresponding average values for Young's modulus E, tensile strength ($\sigma_{max}$) and elongation at break ($\varepsilon_b$) reported in Table 17.

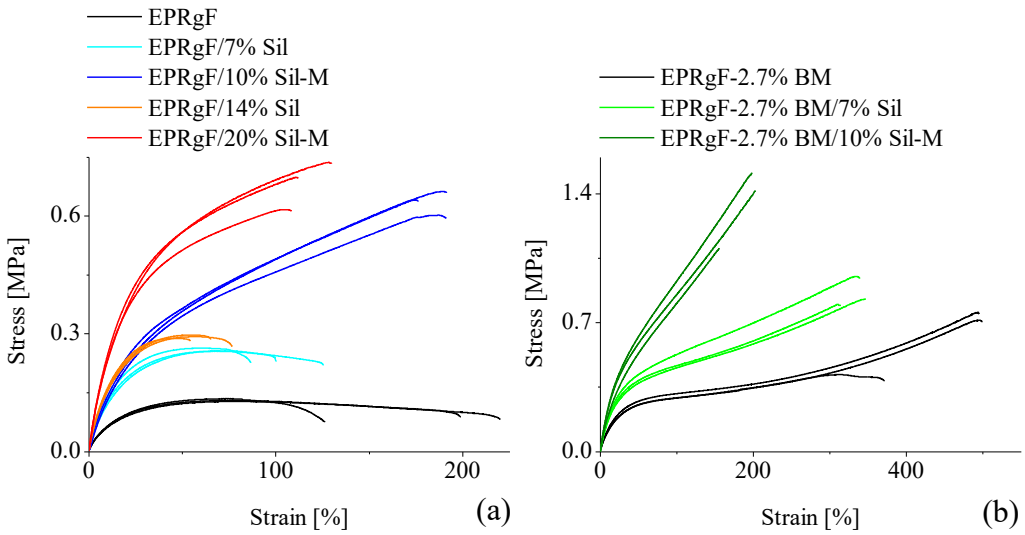


Figure 91. Stress-strain curves from tensile testing on the silica composites without (a) and with (b) BM.

Table 17. Average Young's modulus E, tensile strength $\sigma_{max}$ and elongation at break $\varepsilon_b$ with their standard deviations, of the silica composites.

| | **Average ± *st. dev.* of E** [MPa] | **Average ± *st. dev.* of $\sigma_{max}$** [MPa] | **Average ± *st. dev.* of $\varepsilon_b$** [%] |
|---|---|---|---|
| *EPRgF* | 0.49 ± *0.14* | 0.13 ± *0.01* | 182 ± *49* |
| *EPRgF/7%Sil* | 1.12 ± *0.15* | 0.26 ± *0.01* | 106 ± *19* |
| *EPRgF/10%Sil-M* | 1.65 ± *0.15* | 0.63 ± *0.03* | 194 ± *13* |
| *EPRgF/14%Sil* | 1.92 ± *0.03* | 0.29 ± *0.01* | 66 ± *11* |
| *EPRgF/20%Sil-M* | 1.85 ± *0.36* | 0.68 ± *0.06* | 121 ± *10* |
| *EPRgF-2.7%BM* | 1.11 ± *0.10* | 0.63 ± *0.18* | 455 ± *73* |
| *EPRgF-2.7%BM/7%Sil* | 1.14 ± *0.20* | 0.86 ± *0.08* | 338 ± *14* |
| *EPRgF-2.7%BM/10%Sil-M* | 1.97 ± *0.24* | 1.34 ± *0.21* | 188 ± *27* |

Adding 7 and 14 wt% of pristine silica to EPRgF brings a two-fold and four-fold increase in stiffness, respectively (from 0.49 MPa for EPRgF to 1.12 MPa for EPRgF/7%Sil and 1.92 MPa for EPRgF/14%Sil), while the tensile strength doubles with 7 wt% of Sil (from 0.13 MPa to 0.26 MPa) and does not further increase significantly with 14 wt% (0.29 MPa). Besides, the progressive decrease of elongation at break was obtained, corresponding to the typical reinforcement with inorganic particles. Adding Sil-M to EPRgF clearly brings approx. two-fold tensile strength, compared to Sil reference composites, namely 0.63 MPa for EPRgF/10%Sil-M and 0.68 MPa for EPRgF/20%Sil-M, while the stiffness is only enhanced from 1.12 MPa to 1.62 MPa in EPRgF/10%Sil-M, compared to pristine Sil composites. Furthermore, elongation at break obtained in the presence of Sil-M (194 and 121% for 10 and 20%wt Sil-M content, respectively), is significantly higher that the Sil counterparts, suggesting a toughening effect from the crosslinks via Sil-M particles. Addition of silica in EPR-BM crosslinked composites (Figure 91 b) also resulted in significant stiffness increase, with higher modulus for 10% Sil-M (1.97 MPa) compared to pristine Sil (1.14 MPa). Unfortunately, no toughening effect was observed with Sil-M in this case but, thanks to the remarkable elongation at break of EPRgF-2.7%BM (455%), a rather satisfactory value of 188% is still retained for EPRgF-2.7%BM/10%Sil-M.

Since recyclability is one of the main advantage of adopting a reversible network solution, the mechanical properties of the Sil-M composites were investigated after repeated hot-pressing (Figure 92).

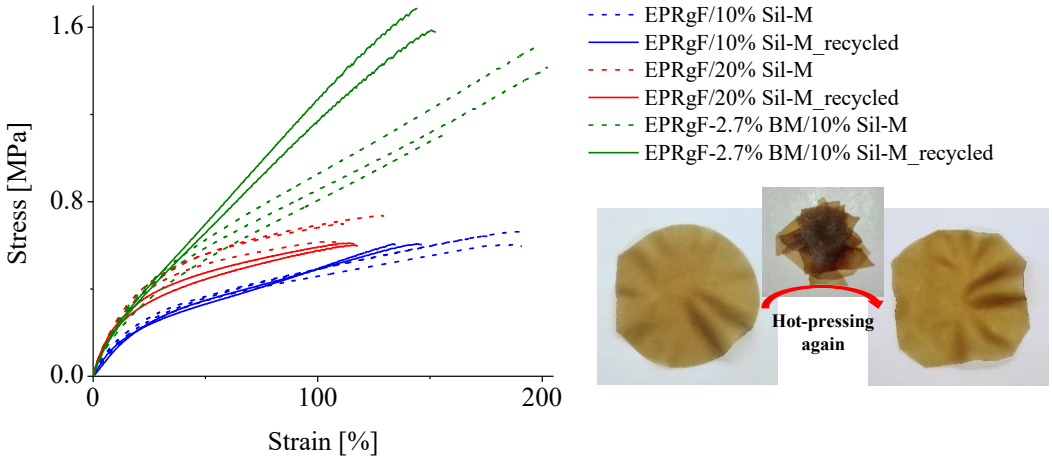


Figure 92. Stress-strain curves from tensile test on the Sil-M reprocessed composites and pictures of a film before/after re-hot pressing.

Results obtained showed a general decrease in elongation at break (from 188% to 148% for EPRgF-2.7%BM/10%Sil-M), which is possibly explained by a small extent of side reactions occurring during thermal reprocessing (as observed in P&F alternative processing) despite no significant changes can be appreciated by FT-IR analysis. However, the performance of the recycled rubbers still appears sufficient for less demanding technological applications (tensile strength is stable for EPRgF/10%Sil-M and EPRgF/20%Sil-M, while it slightly increases from 1.34 MPa to 1.64 MPa for EPRgF-2.7%BM/10%Sil-M), thus representing a significant advantage compared to non-recyclable traditionally crosslinked rubbers.

# Chapter 4

# Conclusions

This doctoral dissertation addressed the preparation of thermoreversibly crosslinked polymers and nanocomposites, exploiting Diels-Alder (DA) reaction with a dissociative covalent adaptable network (CAN) approach, by melt processing and minimizing the use of solvents. Three different polymers were selected and subjected to thermoreversible crosslinking, leading to different results. Regarding the styrene maleic anhydride copolymer (SMA) there were strong evidences of successful diene functionalization with furan as well as its thermoreversible crosslinking after adding a bifunctional dienophile (bismaleimides, BM or BM1), obtained by FT-IR spectroscopy. However, a very brittle material was obtained, likely due to the low molecular weight of pristine SMA and to the limited crosslinking density, which may produce relatively large domains of low molecular weight chains resulting in the mentioned brittleness. Regarding polyethylene grafted with maleic anhydride (PEgMA), furan functionalization was also proved by FT-IR spectroscopy, while limited s evidence of crosslinking with BM1 were found both by FT-IR spectroscopy and tensile testing, likely due to the low content of MA (1 wt%) in PEgMA (and accordingly of furan groups in PEgF) and to the relatively high molecular weight of the crosslinker (3000 g/mol). Regarding the ethylene-propylene rubber grafted with maleic anhydride (EPRgMA), evidences of both furan functionalization and BM crosslinking were observed in FT-IR spectroscopy. This polymer appeared the most promising for the preparation of thermoreversible networks, as tensile tests exhibited higher stiffness and tensile strength with increasing BM content, still yielding soft and highly deformable rubbers, with elastic moduli in the range of 1 MPa and elongation at break typically

higher than 200%. Crosslinking degrees were evaluated by solvent extraction and found directly dependent on the BM concentration, up to ~85% with 8.1 wt% BM, reflecting the mechanical properties. Thanks to the thermally cleavable bonds via the retro-Diels-Alder reaction, crosslinked materials were demonstrated melt-reprocessable into new films. The thermally activated cleavage of the network was first proven by solubilization test at 110°C, whereas reprocessing as a melt required higher temperatures, in the range of 150°C. This is because of both the pristine polymer viscosity and the nature of the dissociative reaction. Indeed, because the retro-DA reaction defines an equilibrium state, the full dissociation of the network is not possible in the molten state, but the equilibrium can be sufficiently shifted toward the dissociated form to allow melt reprocessing. The full recyclability of DA-crosslinked rubbers was demonstrated via multiple reprocessing via compression molding and tensile testing, showing stiffness and strength are slightly increased upon multiple recycling, while elongation at break is maintained.

The reversible crosslinked rubber was also demonstrated for the possible mechanical reinforcement with carbon and silica nanofillers, selected due to their central role in rubber industry. Regarding carbon nanofillers, the reported ability of performing a direct DA reaction on their diene sites was explored with a model reaction of graphite nanoplates (GNP) with a dienophile (MA), both with the already reported method with solvent (GNP-MA_sol) and a new developed vapor process (GNP-MA_vap). The characterization of the products showed strong evidences of the presence of interacting MA on GNP by TGA, especially in the case of GNP-MA_vap, here also with indication of direct covalent DA grafting by Raman spectroscopy and XPS. Relying on this model reaction, implementation of carbon nanoflakes within a DA thermoreversible polymer matrix was aimed. EPR with 5.4 wt% of BM was selected to compromise between processability and crosslinking degree. However, poor GNP dispersion led to the selection of rGO as a more suitable type of carbon nanoflake, added at 5 or 10 wt% loading, aiming at the preparation of reinforced and thermally conductive elastomers. The results indicated homogeneous dispersion of rGO and a remarkable increase in stiffness (up to 8 MPa) and tensile strength (up to 2 MPa) compared to the case of unfilled rubber, along with a thermal conductivity up to 0.47 W/(m·K), while retaining melt reprocessability. Aiming to resolve the high viscosity problems encountered extruding the EP rubber with 10 wt% of rGO, an alternative processing method (Press&Fold, P&F) was targeted, with unsatisfying results due to matrix degradation during the multiple hot-pressing steps. Regarding silica nanocomposites, a maleimide-functionalized silica (Sil-M) was prepared and used

as a reinforcement filler and crosslinking agent for a furan-grafted EP rubber (EPRgF), obtaining a nanostructured thermally reversible network through Diels-Alder reaction between maleimide and furan moieties. When using 20 wt% of Sil-M as the sole crosslinker for the EPRgF rubber, the composite reaches a considerably higher stiffness and tensile strength ($E$=1.85 MPa; $\sigma_{max}$=0.68 MPa) compared to pristine EPRgF ($E$=0.49 MPa; $\sigma_{max}$=0.13 MPa). More importantly, both tensile strength and elongation at break were found significantly higher for Sil-M compared to pristine Sil, at the same concentration of inorganic particles, evidencing the effect of DA crosslinking on mechanical properties at high deformations. As the crosslinking obtained with Sil-M was not quantitative owing to the imperfect dispersion of Sil-M, the combination between Sil-M and bismaleimide (BM) was investigated, to enhance the crosslinking degree and mechanical properties. Indeed, the combination of a moderate content of BM (2.7 wt%) and 10 wt% of Sil-M brought turned out that provide the best performances, with crosslinking degree of 86% yielding a interesting set of mechanical properties ($E$=1.97 MPa; $\sigma_{max}$=1.34 and $\varepsilon_b$=188%). Most importantly, these rubbers were demonstrated for reprocessability through repeated hot pressing, showing high retainment of mechanical properties.

Overall, the results reported in this work demonstrate the possibility to develop a new class of thermoreversibly crosslinked composite rubbers prepared by a sustainable melt-blending process, for the substitution of conventional rubbers, thus contributing to solve the great challenge of recycling, recovery and valorization of used rubbers, within a circular economy approach.

# References


[1] W. Denissen, J.M. Winne, F.E. Du Prez, Vitrimers: permanent organic networks with glass-like fluidity, Chemical Science 7(1) (2016) 30-38.

[2] C.J. Kloxin, C.N. Bowman, Covalent adaptable networks: smart, reconfigurable and responsive network systems, Chemical Society reviews 42(17) (2013) 7161-7173.

[3] D. Montarnal, M. Capelot, F. Tournilhac, L. Leibler, Silica-like malleable materials from permanent organic networks, Science 334(6058) (2011) 965-968.

[4] L. Imbernon, S. Norvez, L. Leibler, Stress relaxation and self-adhesion of rubbers with exchangeable links, Macromolecules 49(6) (2016) 2172-2178.

[5] J. Han, T. Liu, C. Hao, S. Zhang, B. Guo, J. Zhang, A catalyst-free epoxy vitrimer system based on multifunctional hyperbranched polymer, Macromolecules 51(17) (2018) 6789-6799.

[6] S. Kaiser, S. Wurzer, G. Pilz, W. Kern, S. Schlögl, Stress relaxation and thermally adaptable properties in vitrimer-like elastomers from HXNBR rubber with covalent bonds, Soft Matter 15(30) (2019) 6062-6072.

[7] M. Delahaye, J.M. Winne, F.E. Du Prez, Internal catalysis in covalent adaptable networks: phthalate monoester transesterification as a versatile dynamic cross-linking chemistry, Journal of the American Chemical Society 141(38) (2019) 15277-15287.

[8] Y. Li, T. Liu, S. Zhang, L. Shao, M. Fei, H. Yu, J. Zhang, Catalyst-free vitrimer elastomers based on a dimer acid: robust mechanical performance, adaptability and hydrothermal recyclability, Green Chemistry 22(3) (2020) 870-881.

[9] W. Denissen, G. Rivero, R. Nicolaÿ, L. Leibler, J.M. Winne, F.E. Du Prez, Vinylogous Urethane Vitrimers, Adv. Func. Mater. 25(16) (2015) 2451-2457.

[10] M. Guerre, C. Taplan, R. Nicolay, J.M. Winne, F.E. Du Prez, Fluorinated vitrimer elastomers with a dual temperature response, Journal of the American Chemical Society 140(41) (2018) 13272-13284.

[11] P. Wang, L. Yang, B. Dai, Z. Yang, S. Guo, G. Gao, L. Xu, M. Sun, K. Yao, J. Zhu, A self-healing transparent polydimethylsiloxane elastomer based on imine bonds, Europian Polymer Journal 123 (2020) 109382.

[12] A. Rekondo, R. Martin, A. Ruiz de Luzuriaga, G. Cabañero, H.J. Grande, I. Odriozola, Catalyst-free room-temperature self-healing elastomers based on aromatic disulfide metathesis, Materials Horizon 1(2) (2014) 237-240.

[13] M. Rottger, T. Domenech, R. van der Weegen, A. Breuillac, R. Nicolaÿ, L. Leibler, High-performance vitrimers from commodity thermoplastics through dioxaborolane metathesis, Science 356(6333) (2017) 62-65.

[14] S.M. Kim, H. Jeon, S.H. Shin, S.A. Park, J. Jegal, S.Y. Hwang, D.X. Oh, J. Park, Superior toughness and fast self-healing at room temperature engineered by transparent elastomers, Adv. Mater. 30(1) (2018) 1705145.

[15] M. Pepels, I. Filot, B. Klumperman, H. Goossens, Self-healing systems based on disulfide–thiol exchange reactions, Polymer Chemistry 4(18) (2013) 4955-4965.

[16] Y. Zhang, L. Zhang, G. Yang, Y. Yao, X. Wei, T. Pan, J. Wu, M. Tian, P. Yin, Recent advances in recyclable thermosets and thermoset composites based on covalent adaptable networks, Journal of Materials Science & Technology 92 (2021) 75-87.

[17] J. Otera, Transesterification, Chemical reviews 93(4) (1993) 1449-1470.

[18] C.J. Kloxin, T.F. Scott, B.J. Adzima, C.N. Bowman, Covalent adaptable networks (CANs): a unique paradigm in crosslinked polymers, Macromolecules 43(6) (2010) 2643-2653.

[19] O. Diels, K. Alder, Synthesen in der hydroaromatischen Reihe, Justus Liebig's Annalen der Chemie 460(1) (1928) 98-122.

[20] A. Gandini, The furan/maleimide Diels–Alder reaction: a versatile click–unclick tool in macromolecular synthesis, Progress in Polymer Science 38(1) (2013) 1-29.

[21] H. Kwart, K. King, The reverse Diels-Alder or retrodiene reaction, Chemical reviews 68(4) (1968) 415-447.

[22] G. Brieger, J.N. Bennett, The intramolecular Diels-Alder reaction, Chemical reviews 80(1) (1980) 63-97.

[23] D. Craig, Stereochemical aspects of the intramolecular Diels–Alder reaction, Chemical Society reviews 16(0) (1987) 187-238.

[24] K.C. Nicolaou, S.A. Snyder, T. Montagnon, G. Vassilikogiannakis, The Diels-Alder reaction in total synthesis, Angewandte Chemie International Edition 41(10) (2002) 1668-1698.

[25] M.A. Tasdelen, Diels–Alder “click” reactions: recent applications in polymer and material science, Polymer Chemistry 2(10) (2011) 2133.

[26] L.P. Engle, K.B. Wagener, A review of thermally controlled covalent bond formation in polymer chemistry, Journal of Macromolecular Science, Part C: Polymer Reviews 33(3) (1993) 239-257.

[27] S.A. Canary, M.P. Stevens, Thermally reversible crosslinking of polystyrene via the furan–maleimide Diels–Alder reaction, Journal of Polymer Science Part A: Polymer Chemistry 30(8) (1992) 1755-1760.

[28] L.L. Carrette, E. Gyssels, N. De Laet, A. Madder, Furan oxidation based cross-linking: a new approach for the study and targeting of nucleic acid and protein interactions, Chemical communications 52(8) (2016) 1539-1554.

[29] D.S.P. Eftax, A.P. Dunlop, Hydrolysis of simple furans. Products of secondary condensation., The Journal of Organic Chemistry 30(4) (1965) 1317-1319.

[30] X. Chen, M.A. Dam, K. Ono, A. Mal, H. Shen, S.R. Nutt, K. Sheran, F. Wudl, A thermally re-mendable cross-linked polymeric material, Science 295(5560) (2002) 1698-1702.

[31] T. Defize, R. Riva, J.M. Raquez, P. Dubois, C. Jerome, M. Alexandre, Thermoreversibly crosslinked poly(epsilon-caprolactone) as recyclable shape-memory polymer network, Macromolecular rapid communications 32(16) (2011) 1264-1269.

[32] C. Toncelli, D.C. De Reus, F. Picchioni, A.A. Broekhuis, Properties of reversible Diels-Alder furan/maleimide polymer networks as function of crosslink density, Macromolecular Chemistry and Physics 213(2) (2012) 157-165.

[33] S. Billiet, K. De Bruycker, F. Driessen, H. Goossens, V. Van Speybroeck, J.M. Winne, F.E. Du Prez, Triazolinediones enable ultrafast and reversible click chemistry for the design of dynamic polymer systems, Nature chemistry 6(9) (2014) 815-821.

[34] L.M. Polgar, M. van Duin, A.A. Broekhuis, F. Picchioni, Use of Diels–Alder chemistry for thermoreversible cross-linking of rubbers: The next step toward recycling of rubber products?, Macromolecules 48(19) (2015) 7096-7105.

[35] J. Bai, H. Li, Z. Shi, J. Yin, An eco-friendly scheme for the cross-linked polybutadiene elastomer via thiol–ene and Diels–Alder click chemistry, Macromolecules 48(11) (2015) 3539-3546.

[36] B. Willocq, F. Khelifa, J. Brancart, G. Van Assche, P. Dubois, J.M. Raquez, One-component Diels–Alder based polyurethanes: a unique way to self-heal, RSC Advances 7(76) (2017) 48047-48053.

[37] F. Lossada, J. Guo, D. Jiao, S. Groeer, E. Bourgeat-Lami, D. Montarnal, A. Walther, Vitrimer chemistry meets cellulose nanofibrils: bioinspired nanopapers with high water resistance and strong adhesion, Biomacromolecules 20(2) (2019) 1045-1055.

[38] A. Legrand, C. Soulié-Ziakovic, Silica–epoxy vitrimer nanocomposites, Macromolecules 49(16) (2016) 5893-5902.

[39] M. Qiu, S. Wu, Z. Tang, B. Guo, Exchangeable interfacial crosslinks towards mechanically robust elastomer/carbon nanotubes vitrimers, Composites Science and Technology 165 (2018) 24-30.

[40] J. Odent, J.-M. Raquez, C. Samuel, S. Barrau, A. Enotiadis, P. Dubois, E.P. Giannelis, Shape-memory behavior of polylactide/silica ionic hybrids, Macromolecules 50(7) (2017) 2896-2905.

[41] J. Odent, J.M. Raquez, P. Dubois, E.P. Giannelis, Ultra-stretchable ionic nanocomposites: from dynamic bonding to multi-responsive behavior, Journal of Materials Chemistry A 5(26) (2017) 13357-13363.

[42] X. Lu, F. Tian, N. Wang, Q. Zhang, Organic functionalization of the sidewalls of carbon nanotubes by diels-alder reactions: a theoretical prediction, Organic letters 4(24) (2002) 4313-4315.

[43] S. Munirasu, J. Albuerne, A. Boschetti-de-Fierro, V. Abetz, Functionalization of carbon materials using the Diels-Alder reaction, Macromolecular rapid communications 31(6) (2010) 574-579.

[44] B. Willocq, V. Lemaur, M. El Garah, A. Ciesielski, P. Samorì, J.-M. Raquez, P. Dubois, J. Cornil, The role of curvature on Diels-Alder functionalization of carbon-based materials, Chemical communications 52 (2016) 7608-7611.

[45] J.L. Delgado, P. de la Cruz, F. Langa, A. Urbina, J. Casado, J.T. Lopez Navarrete, Microwave-assisted sidewall functionalization of single-wall carbon nanotubes by Diels-Alder cycloaddition, Chemical communications (15) (2004) 1734-1735.

[46] L. Zhang, J. Yang, C.L. Edwards, L.B. Alemany, V.N. Khabashesku, A.R. Barron, Diels-Alder addition to fluorinated single walled carbon nanotubes, Chemical communications (26) (2005) 3265-3267.

[47] C. Menard-Moyon, F. Dumas, E. Doris, C. Mioskowski, Functionalization of single-wall carbon nanotubes by tandem high-pressure/$Cr(CO)_6$ activation of Diels-Alder cycloaddition, Journal of the American Chemical Society 128(46) (2006) 14764-14765.

[48] G. Sakellariou, H. Ji, J.W. Mays, N. Hadjichristidis, D. Baskaran, Controlled covalent functionalization of multiwalled carbon nanotubes using [4+2] cycloaddition of benzocyclobutenes, Chemistry of Materials 19(26) (2007) 6370-6372.

[49] C.-M. Chang, Y.-L. Liu, Functionalization of multi-walled carbon nanotubes with furan and maleimide compounds through Diels–Alder cycloaddition, Carbon 47(13) (2009) 3041-3049.

[50] S. Sarkar, E. Bekyarova, S. Niyogi, R.C. Haddon, Diels-Alder chemistry of graphite and graphene: graphene as diene and dienophile, Journal of the American Chemical Society 133(10) (2011) 3324-3327.

[51] J. Bai, Q. He, Z. Shi, M. Tian, H. Xu, X. Ma, J. Yin, Self-assembled elastomer nanocomposites utilizing $C_{60}$ and poly(styrene-b-butadiene-b-styrene) via

thermally reversible Diels-Alder reaction with self-healing and remolding abilities, Polymer 116 (2017) 268-277.

[52] N.B. Pramanik, N.K. Singha, Direct functionalization of multi-walled carbon nanotubes (MWCNTs) via grafting of poly(furfuryl methacrylate) using Diels–Alder "click chemistry" and its thermoreversibility, RSC Advances 5(114) (2015) 94321-94327.

[53] L.M. Polgar, F. Criscitiello, M. van Essen, R. Araya-Hermosilla, N. Migliore, M. Lenti, P. Raffa, F. Picchioni, A. Pucci, Thermoreversibly cross-linked EPM rubber nanocomposites with carbon nanotubes, Nanomaterials 8(2) (2018) 58.

[54] F. Valorosi, E. De Meo, T. Blanco-Varela, B. Martorana, A. Veca, N. Pugno, I.A. Kinloch, G. Anagnostopoulos, C. Galiotis, F. Bertocchi, J. Gomez, E. Treossi, R.J. Young, V. Palermo, Graphene and related materials in hierarchical fiber composites: production techniques and key industrial benefits, Composites Science and Technology 185 (2020) 107848.

[55] Y. Cao, S. Osuna, Y. Liang, R.C. Haddon, K.N. Houk, Diels-Alder reactions of graphene: computational predictions of products and sites of reaction, Journal of the American Chemical Society 135(46) (2013) 17643-17649.

[56] P.A. Denis, Organic chemistry of graphene: the Diels-Alder reaction, Chemistry 19(46) (2013) 15719-15725.

[57] A.C. Ferrari, Raman spectroscopy of graphene and graphite: disorder, electron–phonon coupling, doping and nonadiabatic effects, Solid State Communications 143(1-2) (2007) 47-57.

[58] W. Chen, K. Wu, Q. Liu, M. Lu, Functionalization of graphite via Diels-Alder reaction to fabricate poly (vinyl alcohol) composite with enhanced thermal conductivity, Polymer 186 (2020) 122075.

[59] J.-M. Seo, I.-Y. Jeona, J.-B. Baek, Mechanochemically driven solid-state Diels–Alder reaction of graphite into graphene nanoplatelets, Chemical Science 4 (2013) 4273-4277.

[60] J.M. Seo, J.B. Baek, A solvent-free Diels-Alder reaction of graphite into functionalized graphene nanosheets, Chemical communications 50(93) (2014) 14651-14653.

[61] O. Zabihi, M. Ahmadi, T. Abdollahi, S. Nikafshar, M. Naebe, Collision-induced activation: towards industrially scalable approach to graphite nanoplatelets functionalization for superior polymer nanocomposites, Scientific reports 7(1) (2017) 3560.

[62] V. Barbera, L. Brambilla, A. Milani, A. Palazzolo, C. Castiglioni, A. Vitale, R. Bongiovanni, M. Galimberti, Domino reaction for the sustainable functionalization of few-layer graphene, Nanomaterials 9(1) (2018) 44.

[63] T. Ramanathan, A.A. Abdala, S. Stankovich, D.A. Dikin, M. Herrera-Alonso, R.D. Piner, D.H. Adamson, H.C. Schniepp, X. Chen, R.S. Ruoff, S.T. Nguyen, I.A. Aksay, R.K. Prud'Homme, L.C. Brinson, Functionalized graphene sheets for polymer nanocomposites, Nature Nanotechnology 3(6) (2008) 327-331.

[64] C.R. Oh, S.H. Lee, J.H. Park, D.S. Lee, Thermally self-healing graphene-nanoplate/polyurethane nanocomposites via Diels-Alder reaction through a one-shot process, Nanomaterials 9(3) (2019) 434.

[65] C.R. Oh, D.I. Lee, J.H. Park, D.S. Lee, Thermally healable and recyclable graphene-nanoplate/epoxy composites via an in-situ Diels-Alder reaction on the graphene-nanoplate surface, Polymers 11(6) (2019) 1057.

[66] K. Ramesh, D.S.B. Anugrah, A.K. Mishra, B.-H. Ahn, Y.-S. Gal, K.T. Lim, Green and sono synthetic approach for direct-functionalization of reduced graphene oxide with poly(styrene-alt-maleic anhydride) by Diels Alder “click” reaction, Applied Surface Science 504 (2020) 144482.

[67] Y. Imai, H. Itoh, K. Naka, Y. Chujo, Thermally reversible IPN organic−inorganic polymer hybrids utilizing the Diels−Alder reaction, Macromolecules 33(12) (2000) 4343-4346.

[68] Z. Jia, S. Zhu, Y. Chen, W. Zhang, B. Zhong, D. Jia, Recyclable and self-healing rubber composites based on thermorevesible dynamic covalent bonding, Composites Part A: Applied Science and Manufacturing 129 (2020) 105709.

[69] S. Schäfer, G. Kickelbick, Self-healing polymer nanocomposites based on Diels-Alder-reactions with silica nanoparticles: the role of the polymer matrix, Polymer 69 (2015) 357-368.

[70] K. Roy, S.C. Debnath, P. Potiyaraj, A critical review on the utilization of various reinforcement modifiers in filled rubber composites, Journal of Elastomers & Plastics 52(2) (2019) 167-193.

[71] S. Colonna, O. Monticelli, J. Gomez, C. Novara, G. Saracco, A. Fina, Effect of morphology and defectiveness of graphene-related materials on the electrical and thermal conductivity of their polymer nanocomposites, Polymer 102 (2016) 292-300.

[72] S. Colonna, D. Battegazzore, M. Eleuteri, R. Arrigo, A. Fina, Properties of graphene-related materials controlling the thermal conductivity of their polymer nanocomposites, Nanomaterials 10(11) (2020) 2167.

[73] L. Maddalena, T. Benselfelt, J. Gomez, M.M. Hamedi, A. Fina, L. Wagberg, F. Carosio, Polyelectrolyte-assisted dispersions of reduced graphite oxide nanoplates in water and their gas-barrier application, ACS Applied Materials and Interfaces 13(36) (2021) 43301-43313.

[74] L.E. Coleman, J.F. Bork, H. Dunn, Reaction of primary aliphatic amines with maleic anhydride, Journal of Organic Chemistry 24 (1959) 135-136.

[75] A.P. Bapat, J.G. Ray, D.A. Savin, E.A. Hoff, D.L. Patton, B.S. Sumerlin, Dynamic-covalent nanostructures prepared by Diels–Alder reactions of styrene-maleic anhydride-derived copolymers obtained by one-step cascade block copolymerization, Polymer Chemistry 3(11) (2012) 3112-3120.

[76] G. Santagiuliana, O.T. Picot, M. Crespo, H. Porwal, H. Zhang, Y. Li, L. Rubini, S. Colonna, A. Fina, E. Barbieri, A.B. Spoelstra, G. Mirabello, J.P. Patterson, L. Botto, N.M. Pugno, T. Peijs, E. Bilotti, Breaking the nanoparticle loading-dispersion dichotomy in polymer nanocomposites with the art of croissant-making, ACS nano 12(9) (2018) 9040-9050.

[77] D.J. Morgan, Comments on the XPS analysis of carbon materials, C - Journal of Carbon Research 7(3) (2021) 51.

[78] G. Socrates, Infrared and Raman characteristic group frequencies: tables and charts, 3rd edition, Wiley2004.

[79] M. Sclavons, P. Franquinet, V. Carlier, G. Verfaillie, I. Fallais, R. Legras, M. Laurent, F.C. Thyrion, Quantification of the maleic anhydride grafted onto polypropylene by chemical and viscosimetric titrations, and FTIR spectroscopy, Polymer 41(6) (2000) 1989-1999.

[80] A. Fina, D. Tabuani, T. Peijs, G. Camino, POSS grafting on PPgMA by one-step reactive blending, Polymer 50(1) (2009) 218-226.

[81] M. Montiel-Herrera, A. Gandini, F.M. Goycoolea, N.E. Jacobsen, J. Lizardi-Mendoza, M.T. Recillas-Mota, W.M. Argüelles-Monal, Furan–chitosan hydrogels based on click chemistry, Iranian Polymer Journal 24(5) (2015) 349-357.

[82] J.M. Rosenfeld, C.B. Murphy, Hydrolysis study of organic acid anhydrides by differential thermal analysis—II: maleic anhydride and trimellitic anhydride, Talanta 14(1) (1967) 91-96.

[83] L.M. Polgar, E. Hagting, P. Raffa, M. Mauri, R. Simonutti, F. Picchioni, M. van Duin, Effect of rubber polarity on cluster formation in rubbers cross-linked with Diels-Alder chemistry, Macromolecules 50(22) (2017) 8955-8964.

[84] K. Sugane, R. Takagi, M. Shibata, Thermally healable/heat-resistant properties of thermosets bearing dynamic and thermally stable bonds formed by the Diels-Alder and thiol-maleimide “click” reactions, Reactive and Functional Polymers 131 (2018) 211-218.

[85] R.W. Nunes, J.R. Martin, J.F. Johnson, Influence of molecular weight and molecular weight distribution on mechanical properties of polymers, Polymer Engineering and Science 22(4) (1982) 205-228.

[86] A. Cuvellier, R. Verhelle, J. Brancart, B. Vanderborght, G. Van Assche, H. Rahier, The Influence of Stereochemistry on the Reactivity of the Diels–Alder Cycloaddition and the Implications for Reversible Network Polymerization, Polym. Chem. 10(4) (2019) 473-485.

[87] B.J. Adzima, H.A. Aguirre, C.J. Kloxin, T.F. Scott, C.N. Bowman, Rheological and chemical analysis of reverse gelation in a covalently crosslinked Diels-Alder polymer network, Macromolecules 41(23) (2008) 9112-9117.

[88] A. Jourdain, R. Asbai, O. Anaya, M.M. Chehimi, E. Drockenmuller, D. Montarnal, Rheological properties of covalent adaptable networks with 1,2,3-triazolium cross-links: the missing link between vitrimers and dissociative networks, Macromolecules 53(6) (2020) 1884-1900.

[89] F. Farivar, P. Lay Yap, R.U. Karunagaran, D. Losic, Thermogravimetric analysis (TGA) of graphene materials: effect of particle size of graphene, graphene oxide and graphite on thermal parameters, C - Journal of Carbon Research 7(2) (2021) 41.

[90] F. Samyn, S. Bourbigot, C. Jama, S. Bellayer, S. Nazare, R. Hull, A. Castrovinci, A. Fina, G. Camino, Crossed characterisation of polymer-layered silicate (PLS) nanocomposite morphology: TEM, X-ray diffraction, rheology and solid-state nuclear magnetic resonance measurements, European Polymer Journal 44(6) (2008) 1642-1653.

[91] J. Gu, X. Meng, Y. Tang, Y. Li, Q. Zhuang, J. Kong, Hexagonal boron nitride/polymethyl-vinyl siloxane rubber dielectric thermally conductive composites with ideal thermal stabilities, Composites, Part A: Applied Science and Manufacturing 92 (2017) 27-32.

[92] Q. Mu, S. Feng, Thermal conductivity of graphite/silicone rubber prepared by solution intercalation, Thermochimica Acta 462(1-2) (2007) 70-75.

[93] A.L. Moore, L. Shi, Emerging challenges and materials for thermal management of electronics, Materials Today 17(4) (2014) 163-174.

[94] Z. Tang, D. Yao, D. Du, J. Ouyang, Highly machine-washable e-textiles with high strain sensitivity and high thermal conduction, Journal of Materials Chemistry C 8(8) (2020) 2741-2748.

[95] R.D.I.G. Dharmasena, K.D.G.I. Jayawardena, Z. Saadi, X. Yao, R.M.I. Bandara, Y. Zhao, S.R.P. Silva, Energy scavenging and powering e-skin functional devices, Proceedings of the IEEE 107(10) (2019) 2118-2136.

[96] F. Orozco, Z. Niyazov, T. Garnier, N. Migliore, A.T. Zdvizhkov, P. Raffa, I. Moreno-Villoslada, F. Picchioni, R.K. Bose, Maleimide self-reaction in furan/maleimide-based reversibly crosslinked polyketones: processing limitation or potential advantage?, Molecules 26(8) (2021).

[97] F. Romani, R. Corrieri, V. Braga, F. Ciardelli, Monitoring the chemical crosslinking of propylene polymers through rheology, Polymer 43(4) (2002) 1115-1131.